TÉCNICO LISBOA

Mountain Waves in Aviation: Prediction and Effects

Jin Maruhashi

Thesis to obtain the Master of Science Degree in

Aerospace Engineering

Supervisors: Prof. Pedro da Graça Tavares Álvares Serrão

Dr. Maria Margarida Sena Belo Santos Pereira

Examination Committee

Chairperson: Prof. Filipe Szolnoky Ramos Pinto Cunha

Supervisor: Dr. Maria Margarida Sena Belo Santos Pereira

Member of the Committee: Prof. Luíz Manuel Braga da Costa Campos

June 2019

Dedicated to…

My Family, who has always motivated me to fly higher.

Acknowledgements

I would like to begin by extending my deepest gratitude to both of my advisors, Dr. Margarida Belo from the Aeronautical Meteorology Division at IPMA (Instituto Português do Mar e da Atmosfera) and Professor Pedro Serrão from Instituto Superior Técnico, who have been ever-present in teaching, guiding and supporting me throughout this thesis.

I would additionally like to thank Dr. Carlos Mateus, Head of the Aeronautical Meteorology Division at IPMA during the time of this thesis, for welcoming me into IPMA's facilities and granting me access to its resources.

I am also grateful to SATA (SATA Internacional – Azores Airlines, S.A.) for their cooperation in providing flight data from some of its aircraft traveling to Pico Island, upon which this work is based.

Last but certainly not least, loving gratitude is extended to my family, who has never ceased to motivate and propel me to greater heights. My mom, with an unmatched passion for aviation, has never gone a day without giving me strength and encouraging me and my studies. My dad, whose request to construct an indestructibly safe aircraft, has likewise always supported and motivated me to study even harder. My sister (currently pursuing her PhD), whose successful career as an accomplished scientific writer, has inspired me to achieve more. I would also like to thank my aunts, uncles and grandmother for their continued support over the years, and my grandfather, who has already flown to Heaven. I am also grateful to my girlfriend, who has always believed in me, for her loving support. And, of course, my dear dog Bilson, whose constant snoring has helped me stay awake at night and be more productive.

Resumo

Investiga-se um incidente de aterragem abrupta que ocorreu no aeródromo do Pico (LPPI) com uma aeronave Airbus A320-200 através de observações aéreas e previsões do modelo AROME. Um segundo voo é analisado. A intensidade do cisalhamento do vento e a influência deste em ambos os voos são calculados através do fator "*I*", recomendado pela ICAO, e pelo F-factor, recomendado pela FAA e NASA. Estes indicadores baseiam-se nas observações registadas pelas aeronaves. Durante o Voo 1, 36% da fase de aterragem (abaixo de 2100 pés) ocorreu sob condições "severas" do cisalhamento do vento e 16% sob condições "fortes". A montante da montanha do Pico, o escoamento era caracterizado por ventos de sudoeste, estratificação estável e um número de Froude perto de 1. De acordo com o modelo AROME, tais condições originaram ondas de montanha que se propagam na vertical, com velocidades verticais máximas acima de 400 pés/min e acima de 200 pés/min ao longo da trajetória da aeronave. As condições severas de cisalhamento do vento e os valores elevados da velocidade vertical, associados às ondas de montanha, poderão ser a causa do referido incidente. Durante o segundo voo, uma esteira com vórtices desenvolveu-se perto da sua trajetória. Sendo este resultado consistente com o número de Froude baixo à montante e com os diagramas do regime de escoamento de estudos passados. Durante a fase de aproximação do Voo 2, não houve condições "severas" do cisalhamento do vento, 4% desta fase foi considerada "forte" e 68% "ligeiro". Após a comparação entre o factor "*I*", o F-factor e os indicadores de turbulência para os dados do AROME, são propostos valores críticos preliminares para estes índices. Por fim, verificou-se que as previsões do vento do AROME apresentam boa concordância com as observações para velocidades acima de 10 nós, revelando, porém, fraca precisão para ventos fracos.

Palavras-chave: ondas de montanha; esteira; modelo AROME; indicadores de turbulência; Açores; número de Froude; verificação objetiva do modelo; observações aéreas; F-factor

Abstract

A hard landing incident in Pico Aerodrome (LPPI) involving an Airbus A320-200 aircraft is investigated using airborne observations and forecasts of the AROME model. A second flight is also analyzed. The severity of the wind shear and wind effects on both flights is quantified using the intensity factor "*I*" that is recommended by ICAO and the F-factor, recommended by the FAA and NASA. Both measures are calculated from aerial data. During Flight 1, 36% of the landing phase (below 2100 ft) occurred under "severe" wind shear conditions and 16% under "strong". Upstream characteristics included southwest winds, stable stratification and a Froude number close to 1. According to the AROME model, these circumstances triggered the development of vertically propagating mountain waves, with maximum vertical velocities above 400 ft/min and exceeding 200 ft/min in the flight path. These conditions, together with the severe wind shear, may have caused the incident. During the second flight, a wake with lee vortices and reversed flow developed in the region of the flight path, which is consistent with a low upstream Froude number and/or with the flow regime diagram of previous studies. During the approach phase of this flight, "severe" wind shear conditions were absent, with "strong" ones occurring 4% of the time. It predominantly displayed "light" wind shear conditions during 68% of this phase. As a result of the comparison between "*I*", the F-factor and the AROME turbulence indicators, preliminary thresholds are proposed for these indexes. Lastly, this study provides an objective verification of AROME wind forecasts, showing a good agreement with airborne observations for wind speeds above 10 kt, but a poor skill for weaker winds.

Keywords: mountain waves; wake; AROME model; turbulence indicators; Azores Island; Froude number; model objective verification; aircraft observations; F-factor

Table of Contents

Acknowledgements ii
Resumo iii
Abstract iv
List of Figures vii
List of Tables ix
List of Symbols x
List of Acronyms xii
1 Introduction 1
1.1 A Background on Mountain Waves 1
1.2 Motivation 3
1.2.1 The Importance of Understanding Mountain Waves 3
1.2.2 The Orography of Pico Island 4
1.3 Thesis Objectives and Contributions 4
1.4 Thesis Structure 5
2 Mountain Wave Fundamentals and Forecasting 6
2.1 Brunt-Väisälä Frequency N 6
2.2 Dimensionless Parameters of Orographic Flow 9
2.2.1 Froude Number 9
2.2.2 Rossby Number 11
2.2.3 Reynolds Number 12
2.3 Governing Equations of Mountain Waves 13
2.3.1 Fundamental Laws 13
2.3.2 Linear Mountain Wave Equation 15
2.3.3 Internal Gravity Wave Structure 17
2.3.4 Flow Behavior over Topography with Constant Wind Speed and Stability 20
2.3.5 Flow Behavior with Vertical Variations in Wind Speed and Stability 23
2.3.6 Flow Behavior over an Isolated, Three-Dimensional Mountain 25
2.4 Forecasting with Regime Flow Diagrams 26
2.5 AROME Model Description 30
3 Measures of Wind Shear and Turbulence Predictors 31
3.1 Definitions of Wind Shear and Wind Components 31
3.1.1 Headwind and Crosswind Definitions 31
3.1.2 Wind Shear Definition 32
3.2 Quantitative Indicators of Wind Shear 33

3.2.1 SATA Airborne Measurements ... 33
3.2.2 Wind Shear Intensity Factor I Definition ... 34
3.2.3 F-factor Definition ... 36
3.3 Turbulence Predictors ... 39
3.3.1 Brown Index Φ ... 40
3.3.2 Ellrod TI Indexes ... 40
3.3.3 CAT1 Indicator ... 41
3.3.4 EDR (Eddy Dissipation Rate) Indicator ... 41
3.4 RMSE and MAE for Wind Speed and Direction ... 41
4 Results and Discussion ... 43
4.1 Synoptic Scale Analysis ... 43
4.2 Mesoscale Analysis ... 44
4.3 Results from Observations ... 46
4.3.1 Aerodrome Wind Data ... 46
4.3.2 Characterization of Wind Profiles ... 46
4.3.3 Wind Shear Intensity Factor I Results ... 47
4.3.4 F-factor Results ... 48
4.4 Results from AROME Forecasts ... 50
4.4.1 Characterization of Orographic Flow during Flight 1 ... 50
4.4.2 Characterization of Orographic Flow during Flight 2 ... 52
4.4.3 Turbulence Indicator Results and Comparison ... 55
4.5 Objective Verification of Wind Forecasts from AROME ... 63
5 Conclusions and Future Research ... 65
References ... 67
Appendix ... I
A.1 Linearization of Navier-Stokes, Continuity and Thermodynamic Equations ... I
A.2 Derivation of the Linear Mountain Wave Equation ... IV
A.3 Vertically Propagating Waves during Flights 1 and 2 ... VII
A.4 Brown and Ellrod TI1 Turbulence Indicators ... VIII
A.5 Aircraft Specifications: A320-200 and B747-200 ... X
A.6 Meteorological Convention ... XI

List of Figures

1.1 Lenticular Cloud....2
1.2 Rotor Cloud....2
1.3 Von Kármán Vortex Street....2
1.4 Distance from Pico Aerodrome to Pico Mountain....4
2.1 Theoretical illustration of the flow splitting phenomenon....11
2.2 Illustration of fundamental wave quantities....17
2.3 Propagation of wave packets....18
2.4 Gravity wave structure, propagation and representation....19
2.5 Evanescent and vertically propagating waves....23
2.6 Trapped lee waves....24
2.7 Flow in the xz plane and in the xy plane both for M=1.5....25
2.8 Flow in the xz plane and in the xy plane both for M=4.5....25
2.9 Regime flow diagrams in the absence of an inversion....27
2.10 Regime flow diagram in the presence of an inversion....28
2.11 Wave breaking with dye streamlines....28
2.12 Laboratory results for the flow splitting phenomenon....29
2.13 Lee vortex formation from numerical simulations....30
3.1 Headwind and crosswind components....31
3.2 Coordinate system relative to Aerodrome runway....32
3.3 Terrestrial coordinate system....33
3.4 Approximate flight path....34
3.5 Calculation of flight path....35
3.6 Boundaries for the classification of wind shear intensity....36
3.7 Aircraft force balance diagram....37
4.1 Mean sea level pressure and 10m wind for Flight 1....43
4.2 Mean sea level pressure and 10m wind for Flight 2....44
4.3 Absolute temperature and buoyancy frequency profiles....45
4.4 Froude number vertical profile for both flights....45
4.5 Wind intensity profiles....47
4.6 Relative frequency per wind shear intensity category for both flights....48

4.7 Instantaneous and 1-km averaged F-factors for both flights. 49
4.8 Absolute vorticity ζ_a and wind vectors for Flight 1. 50
4.9 Horizontal wind at 680 ft and maximum vertical velocity under 6000 ft for Flight 1. 51
4.10 Vertical cross-section of vertical velocity through line A-B and C-D on Figure 3.4, for Flight 1. 52
4.11 Absolute vorticity ζ_a and wind vectors for Flight 2. 53
4.12 Horizontal wind at 135 ft and maximum vertical velocity under 6000 ft for Flight 2. 54
4.13 Vertical cross-section of vertical velocity through line A-B and C-D in Figure 3.4, for Flight 2. 54
4.14 Horizontal and cross-sectional variations of Ellrod TI2 and CAT1 for Flight 1. 56
4.15 AROME turbulence indicators vs. wind shear intensity factor "*I*" along flight path, for Flight 1. 57
4.16 Horizontal and cross-sectional variations of EDR during Flight 1. 57
4.17 Horizontal and cross-sectional variations of Ellrod TI2 and CAT1 for Flight 2. 58
4.18 AROME turbulence indicators vs. wind shear intensity Factor "*I"* along flight path, for Flight 2. 59
4.19 Horizontal and cross-sectional variations of EDR during Flight 2. 59
4.20 Comparison between turbulence indicators, instantaneous and 1-km averaged F-factors, Flight 1. 61
4.21 Comparison between turbulence indicators, instantaneous and 1-km averaged F-factors, Flight 2. 62
4.22 Absolute value differences for wind speed and direction for Flights 1 and 2. 63
4.23 Wind profile along flight path according to aerial observations and AROME for Flights 1 and 2. 64
C Vertically propagating waves during Flights 1 and 2. VII
D1 Horizontal and cross-sectional variations of Brown and Ellrod TI1 during Flight 1. VIII
D2 Horizontal and cross-sectional variations of Brown and Ellrod TI1 during Flight 2. IX
E Specifications of aircraft type used during Flights 1 and 2. X
F1 Meteorological convention for wind direction. XI
F2 Wind barb representation. XI

List of Tables

2.1 Rossby numbers by flight 12

2.2 Reynolds numbers by flight 12

4.1 Froude number and related results by flight 46

4.2 Wind data based on METAR at Pico Aerodrome at the time of both flights. 46

4.3 Classification of wind shear intensity for the three lower altitudes in Flights 1 and 2 48

4.4 Suggested preliminary thresholds for three turbulence indicators 60

4.5 Summary of RMSE and MAE for wind speed and direction for both flights 64

E Aircraft specifications by model X

List of Symbols

Greek Symbols

β	Horizontal aspect ratio
Γ_p^d	Dry Adiabatic lapse rate of parcel
Γ_e	Environmental lapse rate
$\vec{\zeta}$	Vorticity vector
θ	Potential temperature
Φ	Wave phase, Brown Turbulence indicator
ϕ	Latitude
χ	Longitude
$\Omega_\oplus$	Earth's angular velocity of rotation
ν	Kinematic viscosity or wave frequency
γ	Flight path angle
λ	Wavelength

Roman Symbols

a	Mountain width
c	Wave phase speed
$\vec{c}_g$	Group velocity vector
e_T	Specific total aircraft energy
g	Gravitational acceleration
g'	Reduced gravity
H	Fluid mean depth
h	Mountain height
h_c	Critical or streamline-dividing height
I	Wind Shear Intensity Factor
k, m	Horizontal and vertical wavenumbers
$\vec{\kappa}$	Wavenumber vector
L	Horizontal length scale of perturbation
l	Scorer parameter
$M, \hat{h}$	Dimensionless mountain height
N	Dry Brunt-Väisälä or buoyancy frequency
p	Pressure field
$\vec{F}_b$	Buoyant force
$\vec{F}_g$	Gravitational force
Fr	Classical Froude number
Fr_i	Inversion Froude number

Fr_h	Dividing streamline Froude number
F	Instantaneous F-factor
$\bar{F}$	1-km Averaged F-factor
$\dot{q}$	Diabatic heat rate per unit mass
$R_\oplus$	Radius of the Earth
Re	Reynolds number
Ro	Rossby number
$\vec{S}$	Wind shear vector
T_e, T_p	Absolute temperatures of the environment and parcel
t	Time
U	Upstream wind speed
u	Zonal wind speed component
v	Meridional wind speed component
w	Vertical wind speed component
Δz	Displacement of air parcel from its equilibrium position
z_0	Equilibrium position at line of neutral buoyancy

List of Acronyms

1D,2D,3D	One, Two and three-dimensional
AROME	Applications of Research to Operations at Mesoscale
CAT	Clear Air Turbulence
DALR	Dry Adiabatic Lapse Rate
DIA	Denver International Airport
ECMWF	European Center for Medium-Range Weather Forecasts
EDR	Eddy Dissipation Rate
FAA	Federal Aviation Administration
GS	Ground Speed
IAS	Indicated Airspeed
ICAO	International Civil Aviation Organization
IPMA	Instituto Português do Mar e da Atmosfera
LLWS	Low-level wind shear
LPPI	Pico Aerodrome
MAE	Mean Absolute Error
METAR	Meteorological Aerodrome Reports
NASA	National Aeronautics and Space Administration
NTSB	National Transportation Safety Board
NWP	Numerical Weather Prediction
PBL	Planetary Boundary Layer
RMSE	Root Mean Square Error
SATA	SATA Internacional – Azores Airlines, S.A.
TAS	True Airspeed
WRF	Weather Research and Forecasting

Chapter 1

Introduction

The first chapter aims to provide sufficient background information on mountain waves in an attempt to shed light on their ever-present relevance in the realm of aviation, especially within the context of flight safety concerns during takeoff and landing. Given the undeniable role these waves play in aircraft dynamics, the strong need to accurately forecast their impact is discussed. Upon exposing the basics of mountain waves and justifying the motivation for their study via statistical evidence from past aerial accidents, the current section will then delineate the thesis objectives.

1.1 A Background on Mountain Waves

In a stable atmosphere, an air parcel that is displaced vertically will experience a buoyancy force that accelerates the air parcel back toward its original position. This buoyancy force is the restoring force for internal gravity waves. A mountain wave is a particular kind of internal gravity wave that is triggered by a stable flow over an orographic obstacle [1].

The earliest study of gravity waves dates back to the 19th century with Lord Rayleigh in 1883 and shortly thereafter with Lord Kelvin in 1886, who successfully investigated standing waves on water [2]. Although not directly associated with orography, both mountain and surface waves in the ocean are connected as they are both driven by buoyancy forces [3]. Perhaps one of the earliest observations of lee waves was made in 1928 by the German Glider Research Institute near the Rossitten Dunes via balloons subjected to ascending currents in the lee of hills [2]. One of the pioneering studies focusing on mountain waves was first published by G. Lyra in 1943 [4] and by Queney in 1947 [5] who proposed solutions to model stratified uniform airflow. Scorer in 1949 [6] studied the orographic response in a scenario in which both the wind speed $U(z)$ and the atmospheric stability, measured by the Brunt-Väisälä frequency $N(z)$, varied with altitude z. Most advances in mountain wave study prior to 1950 focused on purely theoretical solutions with basic assumptions that led to significantly simplified analytical results. In 1960, Sawyer and Hinds [7] were able to numerically solve the linear lee wave equation. Non-linear theory was furthered by Long in 1953 [8] when he published a model for two-dimensional, inviscid and stably stratified flow.

According to Lin [9], a plethora of atmospheric phenomena are linked to the flow over topography, namely, trapped lee waves, rotors, downslope winds, clear air turbulence (CAT), lee vortices and wave breaking. All of these phenomena occur in the mesoscale, with a horizontal scale varying from 2 to 2000 km.

Visually speaking, certain cloud structures may denounce the presence of orographic phenomena and act as warning signs for strong turbulence. Lenticular and rotor clouds for instance, which could form

from vertically propagating or trapped lee waves, are such cases. The former, as the name suggests, is usually shaped like a lens and tends to rest stagnantly atop mountains. The height at which these clouds exist may vary considerably throughout the troposphere. In Britain for example, these clouds may be found at altitudes fluctuating from 1500 to 7500 m while in the rocky regions of the USA they may be spotted between 7500 to 12000 m. A photograph of a lenticular cloud in the British Isles is shown in Figure 1.1. The latter rotor cloud is more elongated and roll-shaped and normally positions itself in the lee of hills. These clouds are linked to eddies that promote vertical circulations that may in turn bring about severe turbulence for aircraft [2]. In France, close to the Mountain of Lure, these dangerous clouds have been known to exist 1400 m above ground level with vertical accelerations averaging 3G [10]. A rotor cloud in the Northern England region near Cross Fell Mountain is shown in Figure 1.2. A von Kármán vortex street, which is a series of rotating and counter-rotating vortices, is yet another possible occurrence in the lee of mountains and is depicted in Figure 1.3.

Figure 1.1: Lenticular Cloud [11].

Figure 1.2: Rotor Cloud [12].

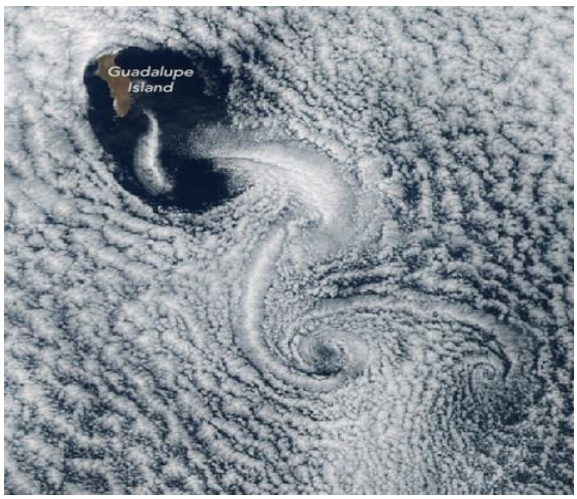

Figure 1.3: Von Kármán Vortex Street [13].

1.2 Motivation

1.2.1 The Importance of Understanding Mountain Waves

In the presence of large amplitude mountain waves, a visually deceptive but potentially damaging form of turbulence known as clear air turbulence (CAT) may develop, which may pose a serious threat to aircraft stability. Their capacity to permeate the troposphere and reach cruise altitudes further consolidates their hazardous nature [14]. Sutherland [3] also notes that internal wave breaking is a common cause for this type of turbulence.

In fact, mountain waves have authored countless aeronautical accidents. Such phenomena may pose serious threats to aircraft not only during their takeoff and landing phases, but also during their flight through the lower troposphere (altitudes of up to 5 km) where atmospheric turbulence and low-level wind shear (LLWS) may reach perilous intensities [15]. According to the National Transportation Safety Board (NTSB), of the 70% of fatal aircraft incidents between 1983 and 1996, close to 25% were shared among low-level turbulence and wind shear events [16]. Further, based on the data collected by the International Civil Aviation Organization (ICAO), a total of 28 aircraft accidents that led to 700 casualties were reportedly caused by LLWS during the period of 1970 to 1985. Heavy investment towards the investigation of low-level wind shear accidents and forms of detection was made by the American government after a Boeing 727 crash-landed at JFK Airport upon encountering severe LLWS in 1975 [17]. Both wind shear and turbulence at lower levels of the atmosphere may be provoked by orography from leeside rotors and hydraulic jumps for instance, which makes the study of mountain wave phenomena an endlessly invaluable pursuit [18]. Therefore, in the 21st century, several studies focus on the validation of numerical model predictions using *in-situ* aerial observations when investigating the potential causes of aviation accidents. The work of Ágústsson and Ólafsson in 2013 [15], for instance, scrutinized the case of a small commercial aircraft that experienced strong turbulence at around 2500 m in the lee of Mt. Öraefajökull in Iceland in 2008. They ultimately concluded that such an event could have been accurately foreseen if pilots at that time were given access to finer-scale simulations. Keller *et al.* [19] investigated a Continental Airlines aircraft that caught fire after veering violently off of the runway in Denver International Airport (DIA) during takeoff. High-resolution numerical simulations enabled them to conclude that lee waves were the probable cause behind the strong crosswinds that caused the accident. Another study published in 2013 by Parker and Lane [20] revealed that turbulence engendered by orographic flow resulted in a fatal lightweight aircraft accident in Australia.

In Portugal, the behavior of Madeira's wake has been the subject of several studies [21-23]. However, mountain waves associated to Pico Mountain (the highest of Portugal), to the authors' best knowledge, have only been addressed previously by Barata *et al.* [24] in terms of a characterization of the surrounding wind regime and validation of the existence of leeside vortices through a scaled physical model of the island placed within a wind tunnel.

Apart from their harmful influence in aeronautics, high-amplitude topographic waves may also engender notable temperature changes resulting from their accelerated downward flow. Such a

phenomenon, usually referred to as foehn warming, can often trigger far-reaching wildfires. Elvidge and Renfrew [25] continue their explanation by alluding to the foehn winds of Santa Ana in California as the culprit behind at least a dozen forest fires that altogether consumed over 1 billion dollars in property.

Therefore, the ability to reliably predict orographic turbulence and understand mountain wave phenomena is of indisputable relevance given its wide-reaching impact not only on flight safety but also on the environment.

1.2.2 The Orography of Pico Island

Pico, one of nine islands that together form the Azorean archipelago (situated in the Atlantic Ocean and located 1500 km from Lisbon), is inherently a geographic focal point of interest because of its unique orography: it comprises Portugal´s tallest mountain with a maximum altitude of 2351 m. Pico Aerodrome (LPPI) lies on the north coast of the island, north of Pico Mountain (Figure 1.4). In the presence of southwesterly winds in the southern region of the Island, which are frequent [24], the likelihood that takeoff and landing phases will be affected by a plethora of orographic phenomena ranging from severe mountain waves, leeside vortices and overall LLWS (low-level wind shear) is increased [24,26].

Figure 1.4: Distance from Pico Aerodrome to Pico Mountain from Google Maps.

1.3 Thesis Objectives and Contributions

The main goal of this thesis is the study of orographic effects that may have led to the hard landing incident involving an Airbus A320-200 aircraft during its approach to Pico Aerodrome (LPPI) in the Azores. Two

flights were considered, where the first one represents the hard landing incident (henceforth referred to as Flight 1) and the second one, labeled Flight 2, will serve as a control parameter that is representative of a flight in which no incidents or significant anomalies were reported. A comparative analysis between airborne results gathered from these flights and predictions of the AROME (Applications of Research to Operations at Mesoscale) model is conducted to not only better understand the incident itself but to also assess the degree of agreement between forecast wind data and observation.

The second goal is to provide an assessment of the agreement between AROME wind forecasts and airborne observations. Five turbulence indicators (Brown, Ellrod TI1, Ellrod TI2, CAT1 and EDR or Eddy Dissipation Rate) are computed from AROME forecasts in order to quantify the turbulence in the surroundings of Pico Aerodrome. The wind shear intensity factor "*I*", as originally suggested by Woodfield and Woods [27], is used to quantify the degree of the wind shear experienced by the aircraft. A preliminary correspondence between these AROME turbulence indicators and the severity of the wind shear registered by the aircraft is presented [28].

Finally, the accuracy of wind forecasts from the AROME model is evaluated. This assessment was performed for both the wind speed and direction, using the root mean square error (RMSE) and the mean absolute error (MAE), as was done in Grubišić *et al.* [21] and Jiménez [29] respectively. This is of great importance because the Portuguese Institute for Sea and Atmosphere (IPMA) routinely provides AROME forecasts of the wind and EDR for Pico and Faial Islands to SATA on an experimental basis. This test phase started in November 2017.

1.4 Thesis Structure

This thesis comprises five chapters. Chapter 2 provides a brief description of the governing mountain wave equations and key dimensionless parameters like the Froude number in order to illustrate the fundamentals behind the characterization of mountain waves. The basic details of the AROME model are then delineated. Other forms of forecasting like the use of flow regime diagrams will also be analyzed. Chapter 3 will mainly focus on mathematically defining the hazard indicators (Wind Shear Intensity Factor *I* and F-factor) that will be computed from airborne data and the turbulence indicators (Brown, Ellrod TI1, Ellrod TI2, CAT1, EDR) that will be quantified from AROME forecasts. Definitions for the RMSE and MAE values are also shown. Chapter 4 presents results from the previously mentioned indicators and provides preliminary threshold suggestions for these turbulence indicators. The accuracy of AROME forecasts against aerial observations will also be quantified via the root mean square error and mean absolute error. Categorization of flow states for each flight via flow regime diagrams is presented. Finally, Chapter 5 will reiterate the main findings of the thesis and suggest paths for future research.

Chapter 2

Mountain Wave Fundamentals and Forecasting

This second chapter begins by inspecting the necessary atmospheric conditions to trigger mountain waves. The origin behind the governing equations of both linear and nonlinear orographic flows is detailed along with a brief exposition of fundamental non-dimensional parameters such as the Froude number. Notable analytic solutions are shown to gain an appreciation of the type of flow regimes foreseen in simple theoretical cases. A description of how to characterize and also predict the occurrence of certain phenomena according to flow regime diagrams then follows. Application of numerical models in research to assist in better understanding aircraft accidents and forecasting orographic phenomena is then discussed. Lastly, the AROME model used in this work is briefly described.

2.1 Brunt-Väisälä Frequency N

Mountain waves, a particular kind of internal gravity wave or buoyancy wave, can only form when the atmosphere is stable, so that a fluid parcel will experience a restoring force (buoyance force) that will push it back to its initial position of equilibrium, sustaining buoyancy oscillations. This could eventually lead to cloud formation depending on the humidity of the air parcel [30], whose change in properties may be found via the ideal gas law (Eq. 2.1):

$$p = \rho R T. \tag{2.1}$$

The pressure of the fluid parcel is p, the density of the air is ρ, R is the universal gas constant and T its absolute temperature [31].

According to Doswell and Markowski [32], the momentum equation based on the z coordinate is expressed as:

$$\rho \frac{dw}{dt} = -\frac{\partial p}{\partial z} - \rho g + 2\rho \Omega_{\oplus} u \cos\phi + \rho F_Z, \tag{2.2a}$$

In Eq. 2.2a, w is the vertical velocity component, g is gravitational acceleration, $\Omega_{\oplus}$ is Earth's angular velocity, ϕ is the latitude, u is the zonal velocity component and F_Z is a net contribution of external forces, like viscous forces. Assuming high Rossby and Reynolds numbers (see Sections 2.2.2 and 2.2.3), it is logical to neglect the Coriolis and external force terms associated to viscous influences. This translates to discarding the last two terms on the right side of Eq. 2.2a. A hydrostatic state is described when, in addition to these considerations, $\frac{dw}{dt}$ is set to zero, yielding:

$$\frac{\partial \bar{p}}{\partial z} = -\bar{\rho} g. \tag{2.2b}$$

The overbar for both pressure and density in Eq. 2.2b represents a basic state variable notation. The prime notation on the other hand denotes a perturbation from this basic state. As such, pressure and density may be quantified as:

$$p = \bar{p} + p' \tag{2.2c}$$

$$\rho = \bar{\rho} + \rho' \tag{2.2d}$$

Substitution of Eq. 2.2b into the simplified form of Eq. 2.2a leads to:

$$\rho \frac{dw}{dt} = -\frac{\partial}{\partial z}(p' + \bar{p}) - (\bar{\rho} + \rho')g = -\frac{\partial p'}{\partial z} - \frac{\partial \bar{p}}{\partial z} - \bar{\rho} g - \rho' g \tag{2.2e}$$

Applying the hydrostatic assumption of Eq. 2.2b to 2.2e produces:

$$\rho \frac{dw}{dt} = -\frac{\partial p'}{\partial z} - \rho' g \Longrightarrow \frac{dw}{dt} = -\frac{1}{\rho}\frac{\partial p'}{\partial z} - \frac{\rho'}{\rho} g \tag{2.2f}$$

Doswell and Markowski [32] then mention the possibility of employing the Boussinesq approximation to Eq. 2.2f, which postulates the existence of a well-defined "reference" vertical density profile $\rho(z)$ so that the buoyancy forces on a fluid particle are determined by the difference between the particle's density and $\rho(z)$ itself rather than on the local difference with the surrounding fluid. In other words, the Boussinesq approximation assumes that density is constant, except in the buoyancy term $\frac{\rho'}{\rho} g$ in Eq. 2.2f. In mathematical terms, $\bar{\rho} = constant$. Once this is taken into account and considering the perturbation term for density small relative to its basic state, it may be stated that $\rho = \bar{\rho}$. If, in Eq. 2.2f, the vertical motion of an air parcel is thought to be affected by only buoyancy and not a pressure gradient as well, then the following simplified form is generated [32]:

$$\frac{dw}{dt} = -\frac{\rho'}{\bar{\rho}} g. \tag{2.2g}$$

The ratio of densities $\frac{\rho'}{\bar{\rho}}$ may be expressed in terms of a ratio of virtual temperatures T_v (See full derivation in Appendix A1) [32]:

$$\frac{\rho'}{\bar{\rho}} \approx -\frac{T_v'}{\bar{T}_v}. \tag{2.2h}$$

Replacing Eq. 2.2h into 2.2g results in:

$$\frac{dw}{dt} = \frac{d^2 \Delta z}{dt^2} = g \frac{T_v'}{\bar{T}_v} = g \frac{T_v - \bar{T}_v}{\bar{T}_v} \equiv \frac{g\left(T_p - T_e\right)}{T_e}, \tag{2.2i}$$

where the virtual temperature T_v represents the air parcel temperature T_p and the environment temperature T_e is considered the base state of the virtual temperature ($\overline{T_v}$).

$$\begin{cases} T_e = T_0 - \Gamma_e \Delta z = T_0 + \dfrac{\partial T_e}{\partial z}\Delta z \\ T_p = T_0 - \Gamma_p^d \Delta z = T_0 + \dfrac{\partial T_p}{\partial z}\Delta z. \end{cases} \tag{2.3}$$

where $\Gamma_e = -\frac{\partial T_e}{\partial z}$ is environmental lapse rate and the parcel lapse rate is represented by $\Gamma_p^d = -\frac{\partial T_p}{\partial z} = 9.8\ ℃/km$, which is the dry adiabatic lapse rate.

Substitution of (2.3) into (2.2i) then leads to:

$$\frac{d^2\Delta z}{dt^2} = \frac{g\left(T_0 - \Gamma_p^d \Delta z - T_0 + \Gamma_e \Delta z\right)}{T_0 - \Gamma_e \Delta z} = -\frac{g\left(\Gamma_p^d - \Gamma_e\right)}{T_0 - \Gamma_e \Delta z}\Delta z.$$

From this point forward, the expression for the dry Brunt-Väisälä frequency N is clear and is shown in (2.4):

$$\begin{cases} \dfrac{d^2\Delta z}{dt^2} + N^2 \Delta z = 0 \\ N^2 = \dfrac{g\left(\Gamma_p^d - \Gamma_e\right)}{T_0 - \Gamma_e \Delta z}. \end{cases} \tag{2.4}$$

If one were to consider that Δz is small[1] so that $T_0 \gg \Gamma_e \Delta z$, then the dry buoyancy frequency may be simplified in the ensuing manner [1]:

$$N^2 = \frac{g\left(\Gamma_p^d - \Gamma_e\right)}{T_0} \tag{2.5}$$

The concept of potential temperature θ is of considerable utility in atmospheric studies given its unvarying nature amidst adiabatic motion for dry air. It may be defined as follows, with p in millibars [1,31]:

$$\theta = T\left(\frac{1000}{p}\right)^{0.288}. \tag{2.6}$$

The dry buoyancy frequency may thus be written according to θ:

$$N^2 = \frac{g}{\theta_0} \cdot \frac{\partial \theta_e}{\partial z}, \tag{2.7}$$

where θ_e is the environmental potential temperature.

By analyzing the differential equation derived in (2.4), it becomes clear that buoyancy waves can only develop when $N^2 > 0$ $(\Gamma_e < \Gamma_p^d)$, in other words, whenever the atmosphere is statically stable. When $N^2 =$

[1] A reasonable assumption since the linearity of the temperature profile is not guaranteed throughout the atmosphere [1].

0, the equilibrium is neutral and the net restoring force is zero. When $N^2 < 0$, the atmosphere is statically unstable and the air parcel will accelerate away from the initial position.

2.2 Dimensionless Parameters of Orographic Flow

The Froude and Rossby numbers, which are both dimensionless, can provide key information about the dynamics of orographic flow. The Froude number is a dimensionless parameter that may be utilized to describe the interaction mechanism between kinetic and potential energies as air flows past orography, according to Sutherland [3]. It is also of value in predicting the type of flow phenomenon that may occur in the lee of a mountain when paired with a flow regime diagram, as was done by Sheridan and Vosper [33]. Three definitions of the Froude number will be considered in this work. The first is the classical Fr form, the second is based on Sheppard's dividing-streamline concept [34] and the third is calculable when a temperature inversion is present in the vicinity of the upstream region of a mountain. The Rossby number is useful in establishing whether or not the Earth's rotation will impact flow dynamics. Lastly, the Reynolds number is also mentioned. These parameters will then help justify and explain the simplifying assumptions employed in the governing equations.

2.2.1 Froude Number

Lynch and Cassano [35] generalize the Froude number as being the ratio of the inertial force to the force of gravity: $Fr \sim \frac{inertia}{gravity}$.

The classical Froude number, Fr, may be defined as:

$$\mathrm{Fr} = \frac{\bar{U}}{N h_m}, \tag{2.8}$$

where $\bar{U}$ is the mean flow speed, N is the Brunt-Väisälä frequency and h_m is the mountain height [36-38]. If $\mathrm{Fr} > 1$ (supercritical flow), then all fluid parcels, even near the ground, can ascend the obstacle [36]. This also means that an air parcel will continually decelerate and see its kinetic energy dwindle as it travels uphill. Once it reaches the top, its speed and ergo kinetic energy will be at a minimum (but maximum potential energy). At the lee of the mountain, the parcel once again is accelerated and its potential energy is converted back to kinetic energy [1]. On the other hand, if $\mathrm{Fr} < 1$ (subcritical flow), then a portion of the fluid below a critical height h_c will be blocked on the upstream side and will not be able to flow over the orographic obstacle (flow splitting phenomenon). It will instead flow around the hill. An illustration of this flow splitting phenomenon is provided in Figure 2.1, in which z_b represents the critical height.

The Froude number is also of use in understanding the linearity of the flow. The smaller this value the greater the nonlinear effects will be. These are usually associated with tall mountains that are then capable of generating high-amplitude waves [3]. A low Fr may indicate the presence of any of the following nonlinear events: lee vortices, strong downslope winds, wave breaking and upstream blocking [9]. Vosper

et al. [39] provide a complementary definition to Eq. 2.8, F_L, that is based instead on a horizontal length scale L, such that $F_L = U/NL$. For this parameter, whenever $F_L \leq 1$ vertically propagating waves are expected, but are evanescent if $F_L > 1$.

Note that some authors [40-42], alternatively, refer to the dimensionless mountain height M:

$$M = \frac{1}{\mathrm{Fr}} = \frac{N h_m}{U_{nm}}, \tag{2.9}$$

where, in the present study, N represents an average value for the Brunt-Väisälä frequency below h_m and U_{nm} a cross-mountain wind speed average also under h_m, as is done similarly by Jiang *et al.* [42].

The computation of the dividing-streamline Froude Number ($\mathrm{Fr_h}$) depends on the determination of the dividing-streamline height h_c, which is possible according to the following formula proposed by Sheppard [34] under stable conditions and with varying wind speed and stratification:

$$\frac{1}{2}\bar{V}_h^2(h_c) = \int_{h_c}^{h_m} N^2(z)\,(h_m - z)dz, \tag{2.10}$$

where Heinze *et al.* [36] define $\bar{V}_h$ as the mean horizontal velocity as a function of the horizontal velocity components u and v: $\bar{V}_h = \sqrt{u^2 + v^2}$. They also note how Eq. 2.10 may be understood as a statement in which the kinetic energy of the flow is entirely converted to gravitational potential energy. As was done in [36], Eq. 2.10 will be solved iteratively for h_c via the trapezoidal rule to numerically compute the integral.

An expression for the Froude number in terms of the dividing-streamline height may then be obtained by assuming constant values for $\bar{V}_h$ and N in Eq. 2.10, as is noted by Trombetti and Tampieri [43]:

$$\mathrm{Fr_h} = 1 - \frac{h_c}{h_m}. \tag{2.11}$$

According to Wooldridge *et al*. [44], Eq. 2.11 may also be used to find the critical height h_c if $\mathrm{Fr_h}$ is replaced by Fr, defined by Eq. 2.8.

The inversion Froude number $\mathrm{Fr_i}$ may be computed in the presence of an inversion by adopting Vosper's [45] definition:

$$\mathrm{Fr_i} = \frac{U_n}{\sqrt{g' z_i}}, \qquad g' = g\frac{\Delta\theta}{\theta_m}. \tag{2.12}$$

The inversion height in Eq. 2.12 is denoted by z_i, $\Delta\theta$ is the magnitude of the potential temperature difference across the inversion, θ_m is the mean potential temperature below the inversion base and U_n is the cross-mountain wind speed (averaged below z_i). Lin [9] notes that Eq. 2.12 may be viewed as a square root ratio of kinetic over potential upstream flow energies. This interpretation better exemplifies the fact that Froude values above 1 represent a situation in which the fluid possesses enough kinetic energy to ascend the

obstacle, as was mentioned earlier. Typically, lower Fr_i values indicate higher disturbance amplitudes [46]. See Figure 2.1 for a visual representation.

In the presence of a temperature inversion, several authors [21,45,47] provide a regime diagram for a two-layer flow over mountains as a function of the inversion Froude number (Eq. 2.12) and of the ratio $\frac{\mathrm{h_m}}{\mathrm{z_i}}$, as is shown in Figure 2.10.

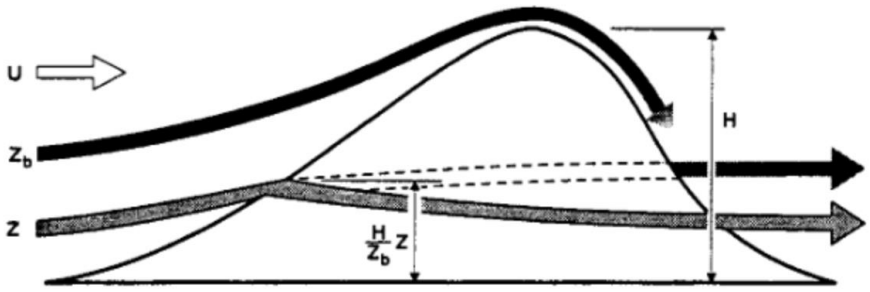

Figure 2.1: Theoretical illustration of the flow splitting phenomenon. Above z_b, the air will flow over the mountain and around it for heights below z_b [48].

In Figure 2.1, Lott and Miller [48] describe the flow splitting phenomenon in terms of z_b, the height at which impinging airflow will be exactly lifted over the peak of the orography. This quantity was previously denoted as h_c, for instance in Eq. 2.10. For an altitude under z_b, like z, the flow will move around the topography and separate near the flanks, rising in height by a factor of $\frac{H}{z_b}$ relative to its initial level z. As before, U is the upstream wind speed and H is the peak elevation of the orographic obstacle.

2.2.2 Rossby Number

The Rossby number Ro bears the name of atmospheric scientist Carl-Gustav Rossby and is a ratio that expresses the influence of the Coriolis effect originating from Earth's rotation relative to the inertia of the wind [35].

It is mathematically defined as follows:

$$Ro = \frac{U}{fL}. \tag{2.13}$$

The horizontal length of the perturbation is L, U is the wind speed and f is the Coriolis parameter which is quantified according to (2.14):

$$f = 2\Omega_{\oplus} \sin \phi\,, \tag{2.14}$$

where $\Omega_{\oplus}$ is Earth's angular velocity of rotation, estimated at $\Omega_{\oplus} = \frac{2\pi}{86400s} = 7.292 \times 10^{-5} s^{-1}$, and ϕ is a latitude. A small Rossby number, say when $Ro < 1$, will indicate a predominant influence of the Coriolis force when compared to the inertial force. Alternatively, $Ro \gg 1$, indicates that Earth's rotation has a low influence on the dynamics of the flow [35].

The Rossby number may be approximated for Flights 1 and 2 and their results are listed below in Table 2.1 using eqns. 2.13 and 2.14.

Table 2.1: Rossby numbers by flight.

	Flight 1	**Flight 2**
$\boldsymbol{\phi}$ [deg]	38.45	38.45
$\boldsymbol{\Omega_{\oplus}}$ [s^{-1}]	7.292×10^{-5}	7.292×10^{-5}
U [ms^{-1}]	17	10
L [km]	21	21
$\boldsymbol{f}$ [s^{-1}]	9.069×10^{-5}	9.069×10^{-5}
$\boldsymbol{Ro}$	8.93	5.25

According to Table 2.1, the Rossby number is considered large for both flights since $Ro > 1$ is fulfilled in either one. This translates to a situation in which Earth's rotation will not have a significant impact on the flow dynamics of orographic phenomena occurring in the vicinity of Pico Mountain.

2.2.3 Reynolds Number

The Reynolds number Re is defined as the ratio between inertial and viscous forces in the following manner:

$$Re = \frac{UL}{\nu}, \tag{2.15}$$

where ν is the kinematic viscosity of the fluid. A large Reynolds number is considered to be above the order of 10^4 and this entails viscous effects being negligible amidst inertial ones, ergo validating the inviscid flow assumption [3]. The Reynolds number of the atmosphere's boundary layer that arises from the Earth's surface is typically close to 10^7, which clearly categorizes the flow as being turbulent. It is therefore typically plausible to apply an inviscid flow approximation [49].

As was done for the Rossby number, the Reynolds number for both flights is summarized in Table 2.2 and is computed using Eq. 2.15 assuming $\nu = 1.5 \times 10^{-5} m^2 s^{-1}$ and the same values for U and L as shown in Table 2.1.

Table 2.2: Reynolds numbers by flight.

	Flight 1	**Flight 2**
$\boldsymbol{Re}$	2.38×10^{10}	1.4×10^{10}

2.3 Governing Equations of Mountain Waves

The 2D orographic flow equations discussed by both Durran and Lin [9,14] for mesoscale dynamics are divided into linear and nonlinear theories. In linear mountain wave theory, it is assumed that the mountain height is small compared to the vertical wavelength of the generated wave. For the latter nonlinear case, the opposite is true: the mountain height is comparable to the vertical wavelength of the orographic disturbance. As will be referred in the next sub-section, this translates to a small value in the classical Froude number Fr. Scorer's equation models linear flow behavior while Long's equation will serve the same purpose for the nonlinear case.

2.3.1 Fundamental Laws

The equations that govern the motion of air derive from three fundamental laws of physics: the second Newtonian law of motion, the conservation of mass or continuity equation and the first law of thermodynamics [9].

Considering the most generic three-dimensional case first, the application of Newton's second law will generate three differential equations called the Navier-Stokes equations Eqs. (2.16) – (2.18) in terms of the zonal u, meridional v and vertical w wind speed components. The frame of reference used in these equations is fixed to the Earth, meaning that a non-inertial frame of reference is being used given the planet's rotation. A moving air parcel will ergo experience an apparent acceleration and consequently force, called the Coriolis force [35]:

$$\frac{Du}{Dt} = -\frac{1}{\rho}\frac{\partial p}{\partial x} + \nu\left(\frac{\partial^2 u}{\partial x^2} + \frac{\partial^2 u}{\partial y^2} + \frac{\partial^2 u}{\partial z^2}\right) + 2\Omega_{\oplus} v \sin\phi - 2\Omega_{\oplus} w \cos\phi \tag{2.16}$$

$$\frac{Dv}{Dt} = -\frac{1}{\rho}\frac{\partial p}{\partial y} + \nu\left(\frac{\partial^2 v}{\partial x^2} + \frac{\partial^2 v}{\partial y^2} + \frac{\partial^2 v}{\partial z^2}\right) - 2\Omega_{\oplus} u \sin\phi \tag{2.17}$$

$$\underbrace{\frac{Dw}{Dt}}_{Acceleration} = -\underbrace{g}_{Gravity} - \underbrace{\frac{1}{\rho}\frac{\partial p}{\partial z}}_{Pressure\ Force} + \underbrace{\nu\left(\frac{\partial^2 v}{\partial x^2} + \frac{\partial^2 v}{\partial y^2} + \frac{\partial^2 v}{\partial z^2}\right)}_{Viscous\ Force} + \underbrace{2\Omega_{\oplus} u \cos\phi}_{Coriolis\ Force}. \tag{2.18}$$

Note that p is the pressure field and t represents time. Additionally, $\frac{D}{Dt}$ is the total derivative[2].

The two remaining fundamental equations are the continuity (2.19) and the first thermodynamic law (2.20) equations [9]:

$$\frac{D\rho}{Dt} + \rho\left(\frac{\partial u}{\partial x} + \frac{\partial v}{\partial y} + \frac{\partial w}{\partial z}\right) = 0 \tag{2.19}$$

[2] $\frac{D}{Dt}X = \frac{\partial X}{\partial t} + u\frac{\partial X}{\partial x} + v\frac{\partial X}{\partial y} + w\frac{\partial X}{\partial z}$

$$\frac{D\theta}{Dt} = \frac{\theta}{c_p T}\dot{q}, \tag{2.20}$$

where c_p is the specific heat capacity at constant pressure and $\dot{q} \equiv \frac{\dot{Q}}{m}$ is the diabatic heat rate per unit mass. Lin [9] then notes that equations (2.16) – (2.20) together form only five independent equations for seven unknowns: $(u, v, w, \rho, p, \theta \; or \; T, \dot{q})$. In order to deal with this under-determined system, two additional equations must be introduced: the ideal gas law, which was presented in Eq. 2.1, and Poisson's relation shown in Eq. 2.6.

The linearization of the system is done by assuming that all relevant variables may be decomposed into two components: a basic state (overbars) and a disturbance (primes). This consideration is called the perturbation method [35] and is generalized for all pertinent variables by equations (2.21):

$$u(x,y,z,t) = \bar{u}(z) + u'(x,y,z,t) \tag{2.21a}$$
$$v(x,y,z,t) = \bar{v}(z) + v'(x,y,z,t) \tag{2.21b}$$
$$w(x,y,z,t) = w'(x,y,z,t) \tag{2.21c}$$
$$\rho(x,y,z,t) = \bar{\rho}(x,y,z) + \rho'(x,y,z,t) \tag{2.21d}$$
$$p(x,y,z,t) = \bar{p}(x,y,z) + p'(x,y,z,t) \tag{2.21e}$$
$$\theta(x,y,z,t) = \bar{\theta}(x,y,z) + \theta'(x,y,z,t) \tag{2.21f}$$
$$T(x,y,z,t) = \bar{T}(x,y,z) + T'(x,y,z,t) \tag{2.21g}$$
$$\dot{q}(x,y,z,t) = \dot{q}'(x,y,z,t). \tag{2.21h}$$

It is important to consider that the multiplication of two smaller terms called perturbations will lead to even smaller quantities. Therefore, perturbation products are considered negligible. Terms like $u'\frac{\partial w'}{\partial x}$ or $w'\frac{\partial w'}{\partial z}$, for instance, are excluded from calculations [35].

It is assumed that any derivative of a state variable will be set to zero except for the pressure and potential temperature: $\frac{\partial \bar{p}}{\partial z} \neq 0$ and $\frac{\partial \bar{\theta}}{\partial z} \neq 0$ [35]. All other basic state variables are therefore constant in both x and z. The exception, which will also be studied, occurs when the zonal wind is considered variable and will therefore have a nonzero derivative with respect to the vertical coordinate z.

2.3.2 Linear Mountain Wave Equation

The Navier-Stokes equations may be simplified when certain assumptions can be made, namely:

- Large Rossby number (Coriolis terms in the Navier-Stokes equations may be disregarded [35]. This was confirmed by the estimations provided in Table 2.1 for both flights).
- Inviscid flow (high Reynolds number translates to inviscid flow or a flow without frictional considerations [35]. In practice, this means inertial forces will dominate to produce a more turbulent flow pattern. The kinematic viscosity ν terms therefore assume a null value).
- 2D flow in the xz plane ($\frac{\partial}{\partial y} = 0, v = 0$).
- Adiabatic flow (assuming a process without heat exchange with the surroundings, it is possible to simplify (2.20) to: $\frac{D\theta}{Dt} = 0$).
- Basic state variable of vertical wind component is zero: $\bar{w} = 0$ (This simplification was incorporated in (2.21c) [35].
- Boussinesq Approximation: This approximation permits density variations that originate buoyancy forces but that do not affect the horizontal force balance. As a consequence, the following two relations are assumed for ρ during the linearization process [35]:
  - $\left|\frac{\rho'}{\bar{\rho}}\right| \ll 1 \Longrightarrow \frac{1}{\rho' + \bar{\rho}} = \frac{1}{\bar{\rho}\left(1 + \frac{\rho'}{\bar{\rho}}\right)} \approx \frac{1}{\bar{\rho}}$
  - $-\frac{\rho'}{\bar{\rho}} \approx \frac{\theta'}{\bar{\theta}}$.
- Hydrostatic approximation for the basic pressure state $\bar{p}$ is assumed:

$$\frac{\partial \bar{p}}{\partial z} = -\bar{\rho} g \tag{2.22}$$

These assumptions then lead to the following condensed Navier-Stokes equations:

$$\frac{\partial u}{\partial t} + u\frac{\partial u}{\partial x} + w\frac{\partial u}{\partial z} + \frac{1}{\rho}\frac{\partial p}{\partial x} = 0 \tag{2.23}$$

$$\frac{\partial w}{\partial t} + u\frac{\partial w}{\partial x} + w\frac{\partial w}{\partial z} + \frac{1}{\rho}\frac{\partial p}{\partial z} + g = 0. \tag{2.24}$$

The continuity equations from (2.19) becomes:

$$\frac{\partial u}{\partial x} + \frac{\partial w}{\partial z} = 0. \tag{2.25}$$

The thermodynamic equation in (2.20) leads to:

$$\frac{D\theta}{Dt} = 0 \Longrightarrow \frac{\partial \theta}{\partial t} + u\frac{\partial \theta}{\partial x} + w\frac{\partial \theta}{\partial z} = 0. \tag{2.26}$$

In a 2D flow, the variables of interest to be decomposed via the perturbation method may be reduced to five:

$$u = \bar{u} + u' \tag{2.27a}$$

$$w = w' \tag{2.27b}$$

$$p = \bar{p}(z) + p' \tag{2.27c}$$

$$\theta = \bar{\theta}(z) + \theta' \tag{2.27d}$$

$$\rho = \bar{\rho} + \rho'. \tag{2.27e}$$

It is assumed that only the basic states of p and θ are variable with altitude z. The process of linearization is conducted by replacing equations (2.27) into equations (2.23 – 2.26) and simplifying, the computations are included in Appendix A.1 The resulting equations are shown below in terms of the perturbation terms (primes) [9,35]:

$$\frac{\partial u'}{\partial t} + \bar{u}\frac{\partial u'}{\partial x} + w'\frac{\partial \bar{u}}{\partial z} + \frac{1}{\bar{\rho}}\frac{\partial p'}{\partial x} = 0 \tag{2.28}$$

$$\frac{\partial w'}{\partial t} + \bar{u}\frac{\partial w'}{\partial x} - g\frac{\theta'}{\bar{\theta}} + \frac{1}{\bar{\rho}}\frac{\partial p'}{\partial z} = 0 \tag{2.29}$$

$$\frac{\partial u'}{\partial x} + \frac{\partial w'}{\partial z} = 0 \tag{2.30}$$

The thermodynamic equation may also be written in terms of the Brunt-Väisälä frequency since $N^2 = \frac{g}{\bar{\theta}}\frac{\partial \bar{\theta}}{\partial z}$ [9]:

$$\frac{\partial \theta'}{\partial t} + \bar{u}\frac{\partial \theta'}{\partial x} + w'\frac{\partial \bar{\theta}}{\partial z} = \frac{\partial \theta'}{\partial t} + \bar{u}\frac{\partial \theta'}{\partial x} + \frac{N^2\bar{\theta}}{g}w' = 0. \tag{2.31}$$

The combination of (2.28 – 2.31) (a complete mathematical derivation is shown in Appendix A.2) into one to obtain a partial differential equation that showcases the disturbance of the vertical wind component w' yields the following linear mountain wave equation:

$$\left(\frac{\partial}{\partial t} + \bar{u}\frac{\partial}{\partial x}\right)^2\left(\frac{\partial^2 w'}{\partial x^2} + \frac{\partial^2 w'}{\partial z^2}\right) + N^2\frac{\partial^2 w'}{\partial x^2} = 0 \tag{2.32}$$

As is noted by Lynch and Cassano [35], the set of linearized equations represented by Eqs. 2.28 – 2.31 involving the unknowns u', w', p' and θ' have been condensed into a single equation (Eq. 2.32) with only one unknown: w'.

2.3.3 Internal Gravity Wave Structure

In order to visualize the structure of an internal gravity wave, a solution to Eq. 2.32 must first be assumed. Based on the notions of Fourier analysis, it is possible to describe any continuous function as a sum of individual wave functions. As such, it is often practical, in the study of atmospheric phenomena, to quantify variables in terms of waveforms. Given also that Eq. 2.32 is a linear differential equation, since products of perturbations have been excluded, it is most logical to consider wave solutions (sines and cosines). Eq. 2.33, a wave defined in the x and z directions, is ergo considered as a solution to Eq. 2.32 [1,35]:

$$w' = w_0 \cos(kx + mz - \nu t). \tag{2.33}$$

In Eq. 2.33, w_0 symbolizes the amplitude, k is the horizontal wavenumber since it concerns the x coordinate, m is the vertical wavenumber given that it pertains to the z coordinate and ν is the frequency of the wave. It is worth noting that $k = \frac{2\pi}{\lambda_x}$ and $m = \frac{2\pi}{\lambda_z}$, where λ_x and λ_z are the horizontal and vertical wavelengths respectively. The argument of Eq. 2.33, $\Phi = kx + mz - \nu t$, is the wave phase. Lines for which this quantity is unvarying are referred to as wavefronts. Wavefronts in turn are perpendicular to the wavenumber vector $\vec{\kappa}$, whose components are both k and m: $\vec{\kappa} = k\vec{e}_x + m\vec{e}_z$. This vector is important since it dictates the direction of wave propagation at a phase speed denoted by c. Markowski [1] provides a simple illustration of these concepts in Figure 2.2.

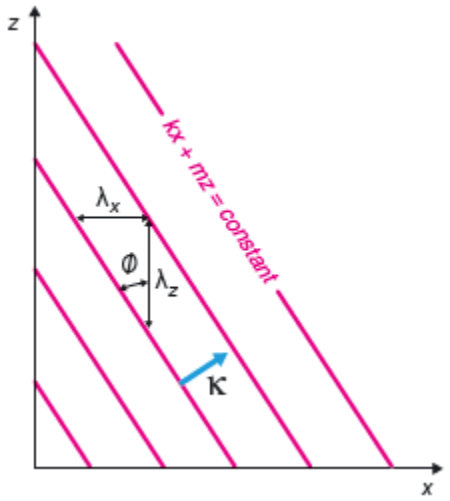

Figure 2.2: Illustration of fundamental wave quantities [1].

Contrary to what is idealized in Eq. 2.33, however, atmospheric waves cannot exist limitlessly in space so will instead occur in packets of wave. These describe regions with visible amplitudes that resulted from the superposition of a multitude of waves of the form implied by Eq. 2.33 [1]. Such is detailed in Figure 2.3.

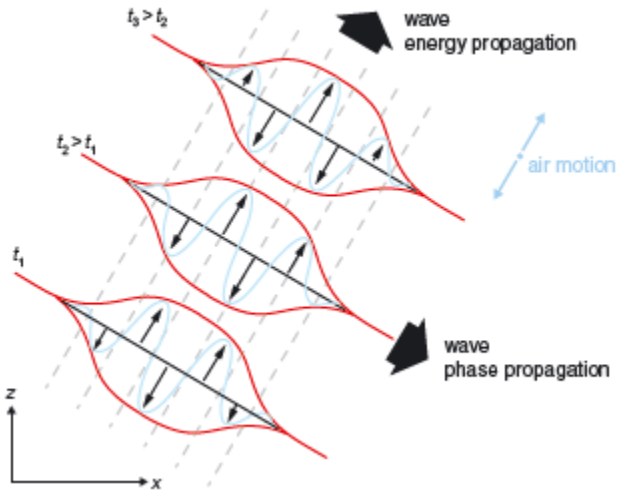

Figure 2.3: Propagation of Wave Packets [1].

The dispersion relation of a gravity wave is an essential statement that connects its frequency ν with wavenumbers m and k. Such an expression may be procured from the characteristic equation resulting from the substitution of Eq. 2.33 into Eq. 2.32:

$$(\nu - \bar{u}k)^2(m^2 + k^2) - N^2k^2 = 0. \tag{2.34}$$

When the basic state horizontal wind speed is set to zero ($\bar{u} = 0$), Eq. 2.34 will yield two distinct roots:

$$\nu = \pm\frac{Nk}{\sqrt{m^2 + k^2}} \tag{2.35}$$

The appropriate root from Eq. 2.35 is chosen so as to guarantee that the frequency ν is a positive value: $\nu = \frac{Nk}{\sqrt{m^2+k^2}}$ when $k > 0$ and $\nu = -\frac{Nk}{\sqrt{m^2+k^2}}$ when $k < 0$ [35].

Once Eq. 2.33 is replaced into the set of linearized equations (Eqs. 2.28 – 2.31), expressions illustrating the development of the horizontal wind component disturbance (u'), the pressure disturbance (p') and the potential temperature disturbance (θ') may be obtained [35]:

$$u' = -\frac{w_0 m}{k}\cos\phi \tag{2.36a}$$

$$p' = -\frac{\rho w_0 \nu m}{k^2}\cos\phi \tag{2.36b}$$

$$\theta' = \frac{w_0}{\nu}\frac{d\bar{\theta}}{dz}\sin\phi\,. \tag{2.36c}$$

For the case of a downward propagating wave to the west ($k, m < 0$), the wavefronts at an initial instant $t = 0$, are computed from the definition of a constant wave phase Φ:

$$\Phi = kx + mz = const. \tag{2.37a}$$

Solving for z leads to:

$$z = -\frac{k}{m}x + const. \tag{2.37b}$$

Wavefronts defined by Eq. 2.37b are shown in Figure 2.4 as lines with a slope of $-\frac{k}{m}$ [35].

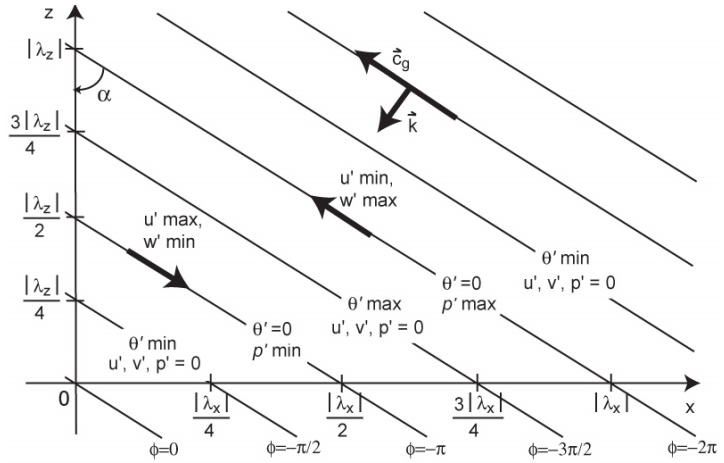

Figure 2.4: Gravity wave structure, propagation and representation of u', w', p', θ' variation [35].

In Figure 2.4, $\vec{c}_g$ denotes the group velocity vector, which can describe the magnitude and direction of a collective or group of waves that is composed of varying amplitudes and phases. The horizontal and vertical components of this velocity are c_{gx} and c_{gz}:

$$\begin{cases} c_{gx} = \dfrac{\partial \nu}{\partial k} \\ c_{gz} = \dfrac{\partial \nu}{\partial m}. \end{cases} \tag{2.38}$$

Another variable of interest illustrated in Figure 2.4 is α, which refers to the angle between air parcel vibrations and the vertical. An expression for this angle may be found by focusing on the right triangle that is formed by legs of length λ_x and λ_z with a hypotenuse of $\sqrt{\lambda_x^2 + \lambda_z^2}$. The cosine of α is therefore:

$$\cos\alpha = \frac{\lambda_z}{\sqrt{\lambda_x^2 + \lambda_z^2}}. \tag{2.39}$$

Replacing wavelengths with wavenumbers into Eq. 2.39 yields:

$$\cos\alpha = \frac{\frac{2\pi}{m}}{\sqrt{\left(\frac{2\pi}{k}\right)^2 + \left(\frac{2\pi}{m}\right)^2}} = \frac{\frac{2\pi}{m}}{\sqrt{\left(\frac{2\pi}{km}\right)^2 (m^2 + k^2)}} = \frac{k}{\sqrt{m^2 + k^2}}. \tag{2.40}$$

Next, applying the dispersion relation of Eq. 2.35 to Eq. 2.40:

$$\nu = \frac{Nk}{\sqrt{m^2 + k^2}} = N\cos\alpha \tag{2.41}$$

According to Eq. 2.41, the wave frequency is a function of the angle α shown in Figure 2.4 and on the buoyancy frequency N. For air parcel oscillations that are totally vertical ($\alpha = 0$), the wave propagates in the horizontal direction and the wave frequency is equal to the Brunt–Väisälä frequency ($\nu = N$). As the angle α increases, air parcel oscillation becomes increasingly horizontal and the frequency of the wave decreases. Also, from Eq. 2.41, it is possible to state that the maximum frequency of vibration for internal gravity waves is N itself [35].

2.3.4 Flow Behavior over Topography with Constant Wind Speed and Stability

Wave phenomena arising from the interaction with Pico Mountain are best understood in theory by considering the case of a flow response over a single hill. Both scenarios in which air flows over an infinite set of hills or across a single orography are, however, closely linked. The solutions in the former situation for an infinite series of ridges are also applicable to the latter since, according to Fourier analysis, a single hill can be modeled by an infinite sum of sines and cosines. The same thinking applies to the atmospheric responses themselves, where individual responses across each hill are superimposed to arrive at the resultant behavior [35]. As such, the solution to the infinite series case is provided first and the transposition to the study of an isolated mountain is then made via Fourier transforms.

Consider a stationary wave ($\frac{\partial}{\partial t} = 0$ and $\nu = 0$) and apply this to Eq. 2.32, which after being integrated twice with respect to x given the second order nature of this differential equation, yields the following [35]:

$$\frac{\partial^2 w'}{\partial x^2} + \frac{\partial^2 w'}{\partial z^2} + \frac{N}{\bar{u}^2} w' = 0 \tag{2.42}$$

Note that in the formulation of Eq. 2.42 it has been assumed that wind speed ($\bar{u}$) and buoyancy frequency (N) are constant. It is common practice to define a ridge of infinite hills in terms of the cosine function [18,35]:

$$h(x) = h_{max}\cos(kx), \tag{2.43}$$

where h_{max} is the peak height and as before, k is the horizontal wavenumber.

As is referred by Durran [18], the generic solution to (2.42) may be expressed as:

$$w' = \mathrm{Re}\left[C_1 e^{i(kx+mz)} + C_2 e^{i(kx-mz)}\right], \tag{2.44}$$

where C_1 and C_2 are complex coefficients and m is now described in the following manner, upon substitution of Eq. 2.44 into Eq. 2.42:

$$m = \sqrt{\frac{N^2}{\bar{u}^2} - k^2}. \tag{2.45}$$

Durran [18] further notes that in Eq. 2.45, the positive root for m was selected in order to remove redundant solutions from Eq. 2.44.

Pertinent lower boundary conditions consist in assuming that wind cannot flow into or out of the surface, which equates to stating that the normal velocity component is zero [35]:

$$w'(x,0) = \bar{u}\frac{\partial h}{\partial x} = -\bar{u}kh_{max}\sin(kx). \tag{2.46}$$

The other required boundary condition relates to the altitude z as it approaches infinity. For the case when the value of m has a nonzero imaginary part ($\bar{u}k > N$), the general solution in (2.44) becomes [18]:

$$w' = \mathrm{Re}\left[C_1 e^{i\left(kx+iz\sqrt{k^2-\frac{N^2}{\bar{u}^2}}\right)} + C_2 e^{i\left(kx-iz\sqrt{k^2-\frac{N^2}{\bar{u}^2}}\right)}\right] = \mathrm{Re}[C_1 e^{-\mu z}e^{ikx} + C_2 e^{\mu z}e^{ikx}]. \tag{2.47}$$

In (2.47), μ is a real number defined as $\sqrt{k^2 - \frac{N^2}{\bar{u}^2}}$. From this expression, it is clear that $C_2 = 0$ must be true since the oscillations cannot boundlessly propagate upwards. On the other hand, when m is real ($\bar{u}k < N$), the radiation condition is used. According to this idea, waves at elevated heights are obliged to be transporting energy away from the hill. In other words, the coefficient associated with the upward energy flux is nonzero and the one linked to the downward energy flux is null. This idea, proposed by Eliassen and Palm [50], was explained in terms of the vertical energy flux $\overline{p'w'}$ that is the product of the perturbation pressure and vertical component averaged across a wavelength. Durran [18] defines the perturbation pressures for waves with constants C_1 and C_2 as p'_{C_1} and p'_{C_2} respectively as:

$$p'_{C_1} = \frac{\bar{u}m}{k}\mathrm{Re}\left[C_1 e^{i(kx+mz)}\right] \tag{2.48}$$

$$p'_{C_2} = -\frac{\bar{u}m}{k}\mathrm{Re}\left[C_2 e^{i(kx-mz)}\right]. \tag{2.49}$$

Since $\overline{p'_{C_1} w'_{C_1}}$ is positive and $\overline{p'_{C_2} w'_{C_2}}$ is negative, it is evident that the former represents the upward flux (upstream tilting wave) and the latter the downward flux (downstream wilting wave). From these results, it is possible to conclude that again $C_2 = 0$ must be abided.

Upon application of these boundary conditions, the following solution to (2.42) is obtained for the perturbation of the vertical velocity component w' [18]:

$$w' = \begin{cases} -\bar{u}h_{max}ke^{-\mu z}\sin(kx); & \bar{u}k > N \\ -\bar{u}h_{max}k\sin(kx+mz); & \bar{u}k < N. \end{cases} \tag{2.50}$$

Results obtained in Eq. 2.50 are consistent with those of Lynch and Cassano [35]. Durran [18] refers that when $\bar{u}k > N$, evanescent or exponentially decaying waves with height are expected. Such a decay is owed to the fact that buoyant restoring forces are not able to sustain the perturbations. On the other hand, when $\bar{u}k < N$, vertically propagating waves that do not suffer losses of amplitude with height are foreseen. In this latter case, oscillations are maintained by these buoyancy forces (see Durran [18], their Figure 4.2).

The solution obtained for the infinite hill scenario (Eq. 2.50) may be transposed to the more realistic situation in which only one hill exists through the use of the Fourier transform $\mathcal{F}$ since an infinite series of sinusoidal functions should be superimposed for this purpose. The Fourier transform $\tilde{f}(k)$ of a generic real function $f(x)$ is [18]:

$$\tilde{f}(k) = \frac{1}{\pi}\int_{-\infty}^{\infty} f(x)\, e^{-ikx}dx. \tag{2.51}$$

It is worth noting that the assumptions of constant $\bar{u}$ and N still hold. Applying the Fourier transform to the governing differential equation in (2.42) will lead to the following [14,18]:

$$\frac{\partial^2\widetilde{w'}}{\partial z^2} + \left(\frac{N^2}{\bar{u}^2} - k^2\right)\widetilde{w'} = 0. \tag{2.52}$$

Defining l in Eq. 2.52 as:

$$l^2 = \frac{N^2}{\bar{u}^2}. \tag{2.53}$$

Using the same boundary conditions as before, the complex analog of (2.50) is found according to Lin [9]:

$$\widetilde{w'}(k,z) = \begin{cases} ik\bar{u}\tilde{h}(k)e^{iz\sqrt{l^2-k^2}}, & N > \bar{u}k \\ ik\bar{u}\tilde{h}(k)e^{-z\sqrt{k^2-l^2}}, & N < \bar{u}k \end{cases}. \tag{2.54}$$

The main difference now between the initial consideration of infinite hills is that Eq. 2.54 must be converted back into the x, z domain by taking the inverse Fourier transform of $\widetilde{w'}(k,z)$ to arrive at $w'(x,z)$ [18].

In order to visualize the expected behavior of mountain waves across isolated orography, the solutions applied to a mountain profile modeled by the "Witch of Agnesi" ($h_W(x)$) are contemplated in Figure 2.5, as was done by Queney [51]:

$$h_W(x) = \frac{h_{max} a}{x^2 + a^2}, \tag{2.55}$$

where a is the mountain width.

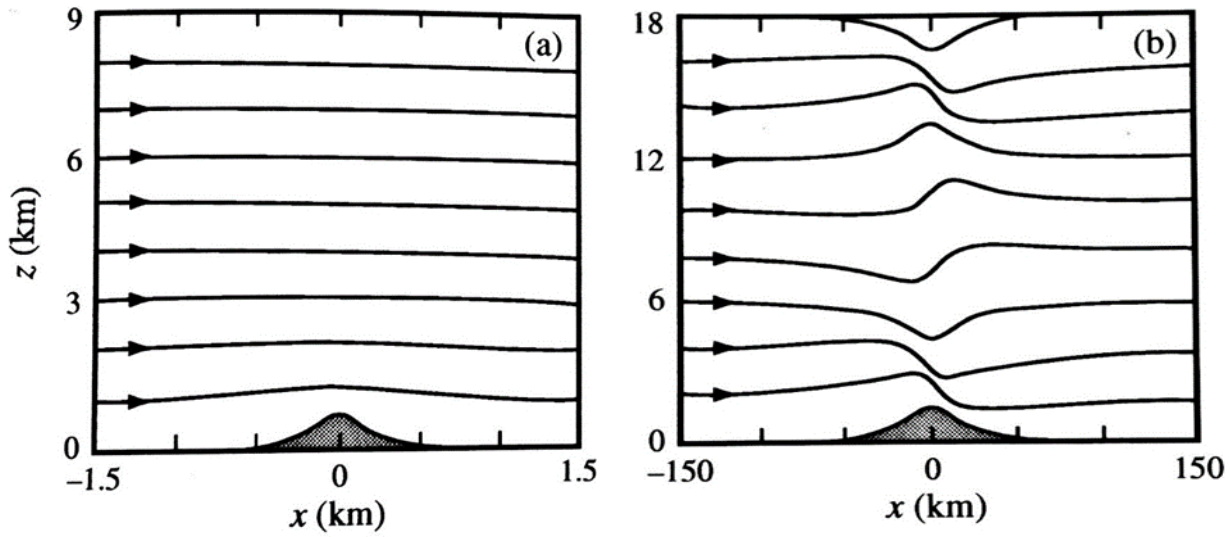

Figure 2.5: (a) Evanescent waves ($N < \bar{u}k$) for flow over an isolated mountain; (b) Vertically propagating waves ($N > \bar{u}k$), from Lin [9].

As was aforementioned, when $N < \bar{u}k$ (Figure 2.5 (a)): $\frac{\bar{u}}{a} \gg N$, where a is the mountain width, dominant wavenumbers force the transition into evanescent waves (which corresponds to a narrow mountain). When $N > \bar{u}k$, vertically propagating waves with constant phase shift are formed. This situation corresponds to a wider mountain: $\frac{\bar{u}}{a} \ll N$ [18].

2.3.5 Flow Behavior with Vertical Variations in Wind Speed and Stability

The scenario is quite idealized, since the wind speed $\bar{u}$ and buoyancy frequency N generally fluctuate in reality. When these parameters are allowed to vary, the governing equation (Eq. 2.56) to consider is obtained by still applying a steady state assumption to Eq. 2.32 but noting now that $\frac{\partial^2 \bar{u}}{\partial z^2} \neq 0$ [18,35].

$$\frac{\partial^2 w'}{\partial x^2} + \frac{\partial^2 w'}{\partial z^2} + \left(\frac{N^2}{\bar{u}^2} - \frac{1}{\bar{u}} \frac{\partial^2 \bar{u}}{\partial z^2} \right) w' = 0. \tag{2.56}$$

Where l is the Scorer parameter, defined as: $l^2 = \frac{N^2}{\bar{u}^2} - \frac{1}{\bar{u}} \frac{\partial^2 \bar{u}}{\partial z^2}$. Under such conditions, trapped lee waves may develop. These waves are another noteworthy orographic phenomenon that occur in the lower atmosphere and may be thought of as a trail of resonant waves that do not exhibit a phase shift [9]. Durran [14,18] posits that these waves form as a result of a pronounced decrease in the Scorer parameter l with altitude by

variation of N and $\bar{u}$. To account for these changes, a two-layer atmospheric model is contemplated in which the Scorer parameters for the upper and lower boundaries are l_U and l_L respectively. A condition that must be met for the existence of at least one trapped lee wave in terms of the lower layer depth H is given by (2.57):

$$l_L^2 - l_U^2 \geq \frac{\pi^2}{4H^2}. \tag{2.57}$$

In other words, (2.57) states that waves will only be trapped when the lower layer is considerably more stable than the one above it, meaning a higher Brunt-Väisälä frequency, or when the basic state wind speed $\bar{u}$ is much smaller. The wave is therefore capable of vertically propagating in the lower layer but is evanescent in the upper layer [18]. An illustration of such waves, that lack tilt, is found in Figure 2.6.

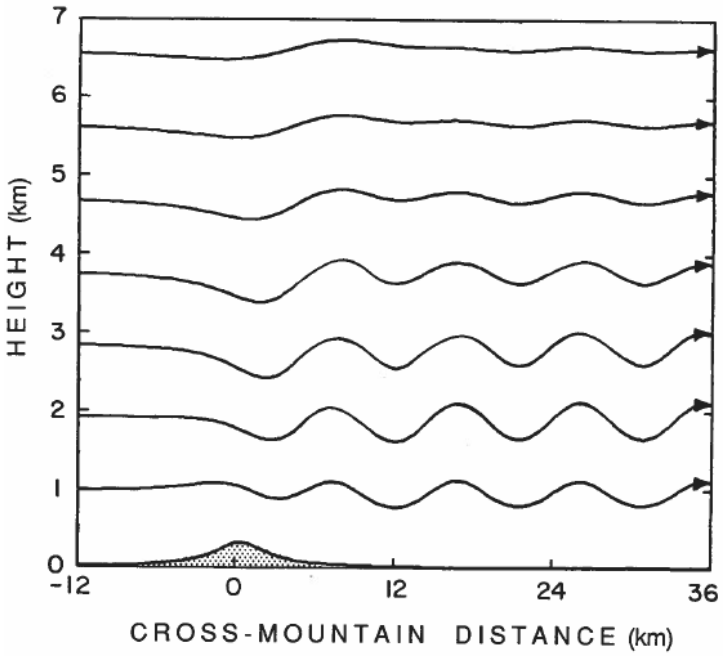

Figure 2.6: Trapped lee waves, from Durran [18].

Linear theory on its own is capable of accurately predicting the amplitude of these resonant lee waves based on numerical studies [14]. In general, analytic solutions in linear mountain wave theory are useful for predicting the behavior of small-amplitude waves and other linear phenomenon. However, linear theory provides a less accurate forecast of nonlinear flow types that include hydraulic jumps and rotors, which actually tend to pose more threats to aviation. This means that other experimental and numerical methods must also be incorporated into the analysis to ameliorate orographic flow forecasting [46].

2.3.6 Flow Behavior over an Isolated, Three-Dimensional Mountain

Flow behavior so far has been modeled only in terms of a two-dimensional hill, for instance via Eq. 2.55. The most complex and realistic approach is therefore to consider a three-dimensional orography. Smolarkiewicz and Rotunno [38] have studied the flow over such an obstacle ($h_{3D}(x,y)$) that is defined was follows:

$$h_{3D}(x,y) = \frac{h_m}{\left[1 + \frac{x^2 + y^2}{a^2}\right]^{\frac{3}{2}}}. \tag{2.58}$$

They generated a series of numerical solutions as a function of the dimensionless mountain height M (Eq. 2.9). Their results for $M = 1.5$ and $M = 4.5$ are presented in Figures 2.7 and 2.8 respectively.

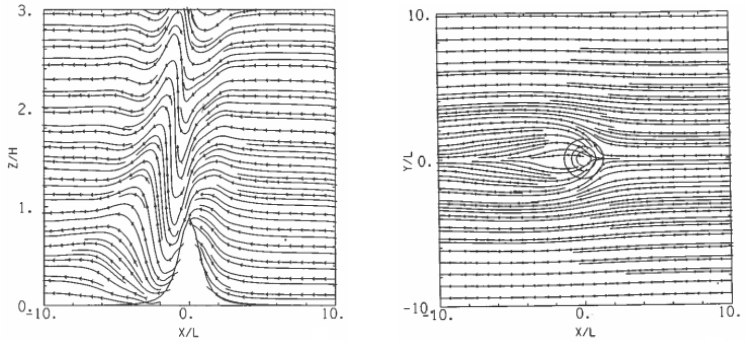

(a) (b)

Figure 2.7: (a) Flow in the *x-z* plane, (b) and in the *x-y* plane both for $M = 1.5$ [38].

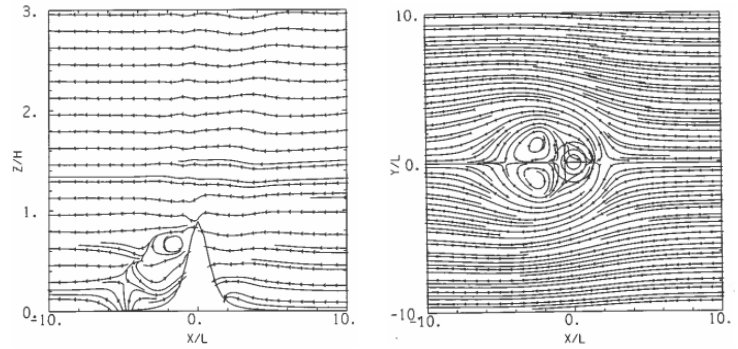

(a) (b)

Figure 2.8: (a) Flow in the *x-z* plane, (b) and in the *x-y* plane both for $M = 4.5$ [38].

It is relevant to note that airflow occurs from the right to the left of Figures 2.7 and 2.8. Vertically propagating waves are witnessed for $M = 1.5$ along with an absence of vorticity in the lee (Figure 2.7). In

Figure 2.8 (a), with an increase in the non-dimensional mountain height, vertically propagating waves are barely present, with reversed flow existing downstream. In Figure 2.8 (b), a pair of vortices is seen. Other 3D studies are referred to in terms of flow regime diagrams in Section 2.4.

2.4 Forecasting with Regime Flow Diagrams

Section 2.3 focused primarily on how mountain waves are predicted mostly according to analytical solutions for the governing flow equations. The present section aims to describe pertinent research that has been done regarding regime flow diagrams, which use not only theory but also amalgamate numerical and laboratorial studies to explain the orographic flow dynamics based on two dimensionless parameters. The most widely used are the Froude number Fr (or its reciprocal M) and the ratio of the mountain height to the inversion height, h_{max}/z_i.

Three regime flow diagrams will be discussed depending on whether a temperature inversion exists. The first two, which will be applied in the absence of an inversion (as is the case for Flight 1) are extracted from Smith [52] who deals with a linear regime and Bauer [41] for nonlinear ones. They map several phenomena, such as lee vortices, flow splitting and wave breaking in terms of two parameters: the dimensionless mountain height M (see Eq. 2.9) and the horizontal aspect ratio β, which is defined as the ratio between spanwise and streamwise lengths. The third flow diagram is applicable whenever an inversion exists, as proposed by Schär and Smith [47] and adapted by Grubišić *et al.* [21] to study the flow dynamics near Madeira's wake. Events like wake formation with vortices, wake formation with and without reversed flow as well as subcritical flow are possible categories within this diagram that operates in terms of the ratio h_{max}/z_i along with the inversion Froude number Fr_i (see Eq. 2.12).

Smith [52] and Bauer [41] contemplate hills of varying geometries via the β parameter, which is defined as follows:

$$\beta = \frac{L_y}{L_x}, \tag{2.59}$$

where L_x is the streamwise length and L_y the spanwise equivalent. For Pico Mountain, this ratio is approximately 1 given its nearly circular geometry. This first two flow diagrams are represented in Figure 2.9 (a) and (b).

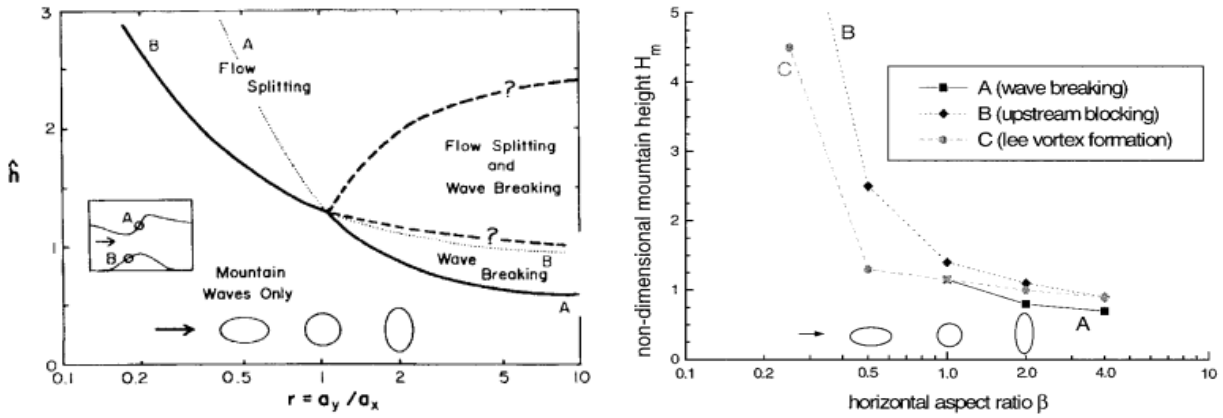

(a) **(b)**

Figure 2.9: Flow regime diagrams in the absence of an inversion for (a) linear regime from Smith [52] and (b) nonlinear diagram based on three-dimensional numerical simulations from Bauer [41].

Figure 2.9 (a) establishes the type of expected phenomena, depending on the ratio $\beta = \frac{L_y}{L_x} = r$ defined in Eq. (2.55) and $\hat{h} = M = \frac{1}{Fr}$, based on Smith's [52] linear theory. Figure 2.9 (b) similarly depicts the same phenomena (including lee vortex formation) using 3D numerical simulations. In both diagrams, it is clear that for any hill geometry, more complex and nonlinear flow behavior transpires as M ($\hat{h}$ or H_m) increases. As is noted in Bauer's [41] analysis of Smith's [52] linear results for a circular obstacle, turbulent flow in the form of wave breaking is initiated approximately at $M = \hat{h} = 1.34$. Flow stagnation for a hill with $\beta < 1$ occurs before wave breaking in the lee. When $\beta > 1$, wave breaking will transpire prior to flow stagnation inherent in the flow splitting phenomenon. In the nonlinear regime (Figure 2.9 (b)), the cutoff value for the occurrence of wave breaking is lowered to $\hat{h} = 1.15$. Bauer [41] further notes that wave breaking is not foreseen for any Froude number whenever the horizontal aspect ratio $\beta \leq 0.5$. This turbulent phenomenon is more common for wider obstacles (for higher β).

Grubišić *et al.* [21] make use of the regime flow diagram shown in Figure 2.10 in order to characterize the orographic flow in the vicinity of Madeira Island. According to this diagram, when the ratio between the mountain height and the inversion height is higher than 1.5, a *Von Kármán vortex* street is expected for any inverse Froude number below 1. According to their WRF (Weather Research and Forecasting) simulations, an eddy shedding period (time taken for a pair of positive and negative vortices to be shed) of about 7 to 8 hours was found. For Pico Island, it is difficult to determine in reality if vortex shedding occurs given the island's wake immediately interfering with São Jorge Island.

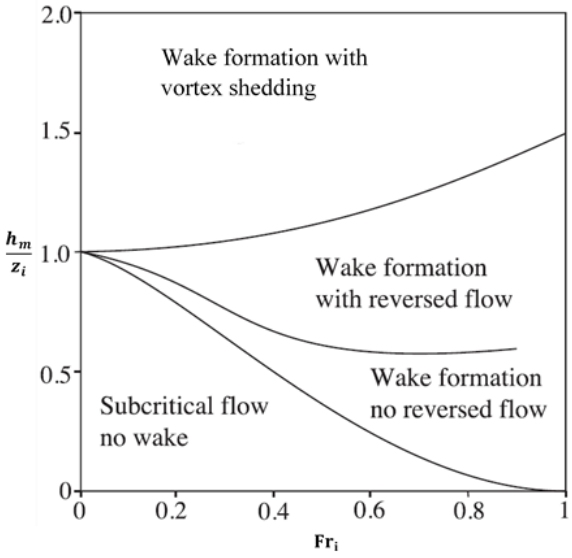

Figure 2.10: Regime flow diagram in the presence of an inversion, adapted from Grubišić *et al.* [21].

Epifanio [40] alludes to small mountain waves, wave-breaking, flow-splitting and lee vortex formation as the most important types of flow phenomena in a scenario in which both wind speed and stability are assumed to be constant, all of which are possible flow states covered by regime flow diagrams of Figures 2.9 and 2.10. Epifanio [40] then provides laboratorial evidence, shown in Figure 2.11, that demonstrates the occurrence of wave breaking with dye streams over an elevation.

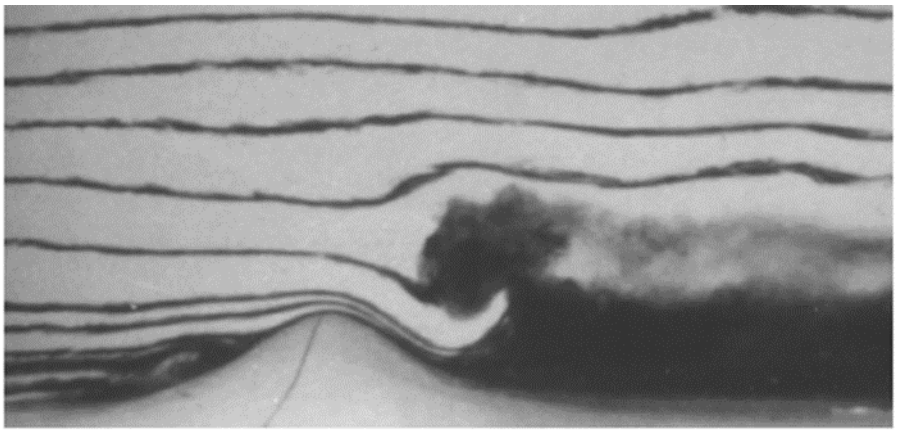

Figure 2.11: Wave breaking with dye streamlines, from Epifanio [40].

Figure 2.11 shows how, at a critical height, certain streamlines will overturn. Such a motion will create a temporary structure in which denser fluid from lower levels is displaced upward and places itself atop lighter fluid parcels. This unstable configuration cannot be sustained for long and the wave will break, thereby generating turbulent flow. Epifanio [40] further observes how a region that is thoroughly mixed is created in the leeside of the obstacle where winds with elevate acceleration are present.

Flow stagnation describes the situation in which the local velocity of the fluid is zero and may orographically transpire at a critical height h_c, which may be calculated via Sheppard's dividing streamline formula in Eq. (2.10). It is caused by the cancellation of movement between the incoming and reversed flows, the latter of which is brought forth as a consequence of an opposing pressure gradient. In a 3D model, flow stagnation is responsible for causing flow splitting [9], which has already been briefly described via a theoretical illustration (Figure 2.1). Figure 2.12 shows laboratorial results depicting the flow splitting phenomenon.

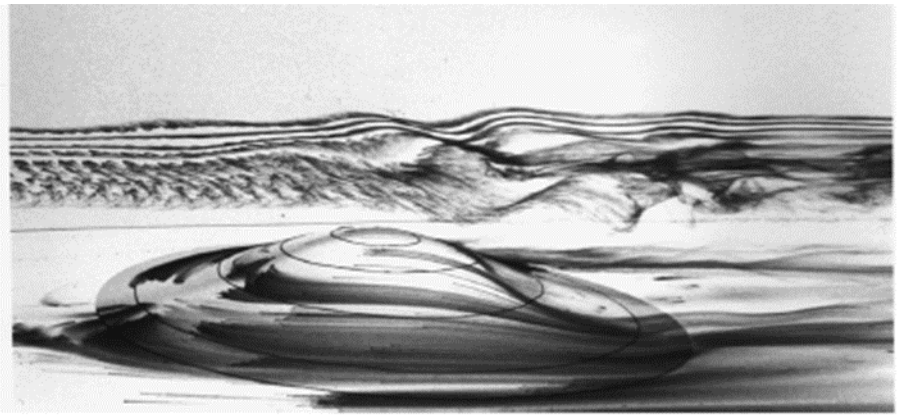

Figure 2.12: Laboratory results for the flow splitting phenomenon, from Epifanio [40].

Epifanio [40] also refers to lee vortices. These may be defined as an alternating pair of eddies whose presence is often associated with flow splitting. Laboratorial research has pointed to the close dependence between lee vortex formation with upstream stagnation while numerical results have hinted at the possibility that flow splitting might not necessarily lead to vorticity. Lin [9] provides a complete overview of several theories that aim to explain the genesis of such eddies. Under the consideration of viscous flow, he shares the ideas of Batchelor [53] and Hunt and Snyder [54] who cite the separation of the boundary layer as the mechanism responsible for lee vortices. In short, this theory describes how in the presence of an elevated Reynolds number flow reversal will arise from an adverse pressure gradient. The clashing of both reversed and incoming flows will create stagnation points on which the streamlines will break away from the surface and move into turbulent regime. Lin [9], however, also notes the contribution of Smolarkiewicz and Rotunno [38] who noted that lee vortices were still being generated past an isolated hill for small Froude numbers, for $Fr \approx 0.6$. These results were obtained from a nonlinear numerical simulation with a free-slip boundary condition, which translates to assuming a frictionless surface and equivalently to neglecting its boundary layer. Lab tank testing showed coherent conclusions. Such a discovery clearly meant that although boundary layer separation could possibly explain vortex generation in viscous flow, it could not do the same for inviscid flow and so evidently other kinds of mechanisms are at work. One possible explanation that is scrutinized by Lin [9] is baroclinicity. This concept may be understood in terms of the

inviscid vorticity equation (2.60), which derives directly from the Navier-Stokes relations (Eqs. 2.16-2.18) via the curl operator [9]:

$$\frac{D\vec{\zeta}}{Dt} = -\vec{V} \cdot \nabla\vec{\zeta} + (\vec{\zeta} \cdot \nabla)\vec{V} + \frac{\nabla\rho \times \nabla p}{\rho^2}. \tag{2.60}$$

The vorticity vector is represented by $\vec{\zeta} = (\zeta_x, \zeta_y, \zeta_z)$. The term in Eq. 2.60 with the vector cross product symbolizes the baroclinic contribution to vorticity. As is known from vector mathematics, $\frac{\nabla\rho \times \nabla p}{\rho^2} \neq 0$ only when the gradient vectors of pressure and density are both misaligned and maximized when they are at right angles of each other. In practical terms, the misalignment of these vector quantities reflects a situation in which density variations impart motion by having heavy fluid sink and lighter fluid rise [3]. Epifanio [40] includes an illustration of lee vortices that were numerically simulated, these results are seen in Figure 2.13.

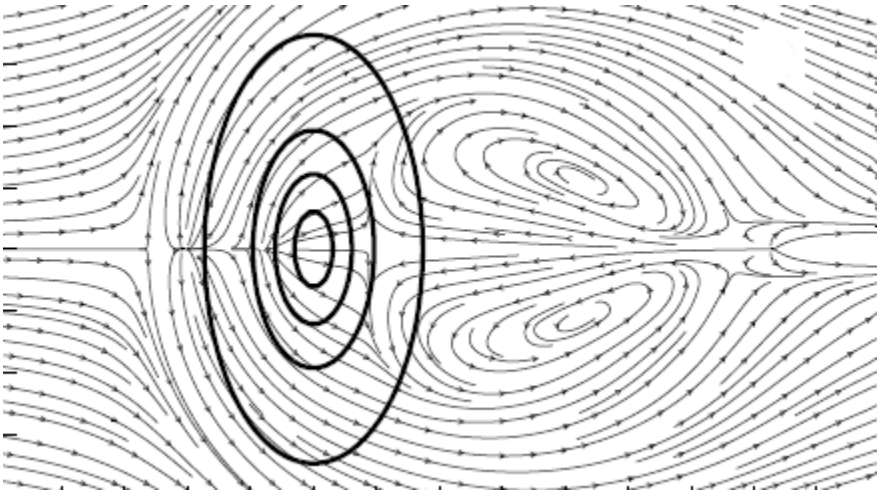

Figure 2.13: Lee vortex formation from numerical simulations, from Epifanio [40].

2.5 AROME Model Description

The AROME model that runs operationally at the Portuguese Institute for Sea and Atmosphere (IPMA) uses a horizontal grid spacing of 2.5 km. It employs a three-class ice scheme with ECMWF (European Center for Medium-Range Weather Forecasts) radiation parameterizations, as is described by Seity *et al.* [55]. Turbulence in the planetary boundary layer is modeled after a prognostic TKE (Turbulent Kinetic Energy) equation from Cuxart *et al.* [56] that uses a diagnostic mixing length. AROME initial and boundary conditions emanate from the ARPEGE (Action de Recherche Petite Échelle Grande Échelle) model. At the time of Flight 1, AROME was integrated with 46 model levels, while at the time of Flight 2 it used 60 vertical levels. For both models, however, the maximum altitude at which forecasts were available is about 45000 ft or 13716 m. This model will mainly provide wind data to compute Froude numbers and turbulence indicators.

Chapter 3

Measures of Wind Shear and Turbulence Predictors

This chapter is mainly devoted to defining the main indicators of wind shear and turbulence that will be used in the current work to analyze Flights 1 and 2. Wind shear (normally referring to vertical wind shear) is simply the change in the wind speed and/or direction with altitude and its effects on aircraft will be measured in terms of the wind shear intensity factor I and the F-factor. Both of these quantities are based on airborne data and aim to portray effects directly experienced by an aircraft. SATA aerial observations are detailed in Section 3.2.1. Next, five turbulence predictors (Brown, Ellrod TI1, Ellrod TI2, CAT1 and EDR) calculated from AROME wind data, are explained. Finally, methods of calculation for the RMSE and MAE values are listed.

3.1 Definitions of Wind Shear and Wind Components

The meteorological convention used in characterizing the wind vector is detailed in Appendix A.6 in Figures F.1 and F.2. Definitions of the cross and headwind components in the perspective of the aircraft are included below. The definition of wind shear, according to ICAO, then follows.

3.1.1 Headwind and Crosswind Definitions

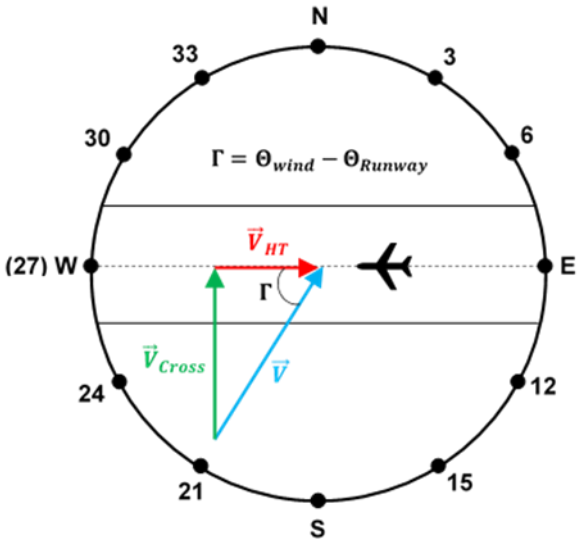

Figure 3.1 Headwind and crosswind components.

The calculation of the head or tailwind component V_{HT} is done by resolving the wind vector $\vec{V}$ according to the angle Γ (see Figure 3.1), which depends on the runway bearing Θ_{runway} and wind direction Θ_{wind} both in degrees. Expressions for V_{HT} and V_{Cross} (the crosswind component) are provided respectively by:

$$V_{HT} = -|\vec{V}| \cos\left[\left(\Theta_{wind} - \Theta_{Runway}\right) \cdot \frac{\pi}{180}\right], \tag{3.1}$$

$$V_{Cross} = |\vec{V}| \sin\left[\left(\Theta_{wind} - \Theta_{Runway}\right) \cdot \frac{\pi}{180}\right]. \tag{3.2}$$

The runway bearing in degrees is determined in relation to the runway code according to Eq 3.3. For Pico Aerodrome, this can be either 27 or 09.

$$\Theta_{Runway} = Runway\ Code \times 10 \tag{3.3}$$

It should be noted that the crosswind is from the left when negative and the headwinds are also represented by positive values.

Note that the reference frame used to express these components is in relation to the airport runway, as is shown in Figure 3.2 according to ICAO [57].

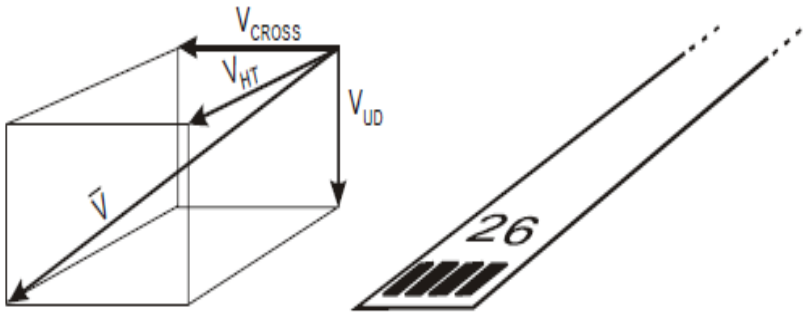

Figure 3.2: Coordinate system relative to Aerodrome runway, from ICAO Manual on LLWS [57].

3.1.2 Wind Shear Definition

Mathematically speaking, wind shear is the difference vector between wind vectors at two distinct points in space. Low-level wind shear (LLWS) is normally the most relevant kind as it occurs in the lower atmosphere at heights below 2000 ft [16], when aircraft are climbing to cruise or approaching to prepare for landing. During these flight phases, aircraft are particularly vulnerable to wind shear destabilization since their airspeed is already at a critical level [57].

The meteorological definition of vertical wind shear uses a reference length that is simply equal to the altitude change between two distinct points in space at which the wind vector was measured. Typically, these vector quantities are measured in the terrestrial coordinate system described in Figure 3.3 by the ICAO LLWS Manual [57].

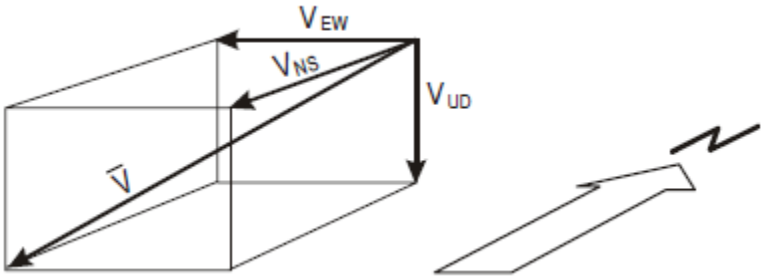

Figure 3.3: Terrestrial coordinate system, from ICAO Manual on LLWS [57].

In Figure 3.3, V_{EW} and V_{NS} are the east-west (or zonal) and north-south (or meridional) components of the wind respectively. The updraft or downdraft term V_{UD} will not be factored into any observationally based indicator of wind shear as only the angle between V_{EW} and V_{NS} is available from SATA aircraft observations. It is worth noting that true wind directions were measured.

The wind shear intensity $|\vec{S}|$, with SI units of s^{-1}, itself is mathematically given by the magnitude of the difference vector between wind vectors at altitudes z_1 and z_2 such that $z_2 < z_1$, divided by $z_1 - z_2$. This is shown in Eq. (3.4) [57]:

$$|\vec{S}| = \frac{\sqrt{\left(V_{EW,1} - V_{EW,2}\right)^2 + \left(V_{NS,1} - V_{NS,2}\right)^2}}{z_1 - z_2}. \tag{3.4}$$

The wind shear definition of Eq. (3.4) will not be used to assess the impact on aircraft since it does not consider their flight trajectory. Instead, the wind shear intensity factor "I" and the F-factor will be used. The first of which is recommended by ICAO and the second was tested as part of NASA and FAA's wind shear program and has become a requirement for FAA certification of onboard detection systems for wind shear hazards [58].

3.2 Quantitative Indicators of Wind Shear

Two wind shear indicators will be defined in this first sub-section: the F-factor and the wind shear intensity factor "I". Both are based on in-flight measurements collected by Airbus A320-200 aircraft.

3.2.1 SATA Airborne Measurements

For each flight, wind intensity and direction (true direction) are provided every 4 seconds along with the corresponding altitude and geographical coordinates (latitude and longitude). Only the approach and landing phases (approximately final 10 minutes of flight or altitudes below 5000 ft) are perused since these are the most pertinent to understanding the incident. The average trajectory for both flights along with Pico's orography according to the AROME model are mapped in Figure 3.4.

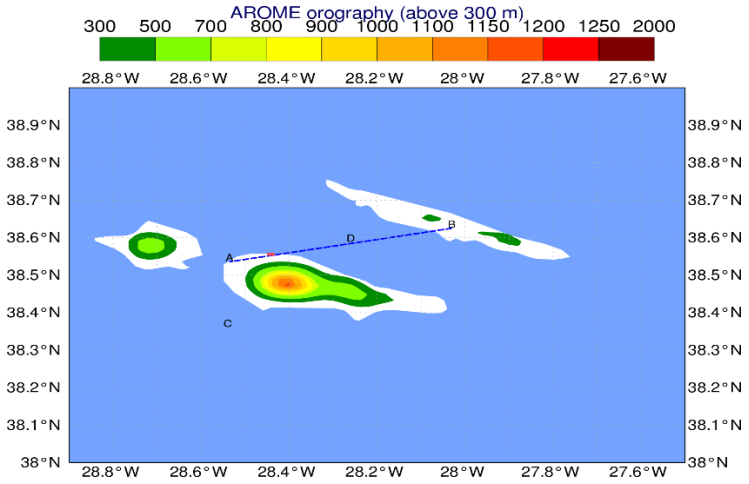

Figure 3.4: Approximate flight path (blue dotted line) and AROME orography. Shading shows elevation in meters. Pink marker shows aerodrome location.

It is important to note that given the limitations of the AROME model, Pico Mountain is depicted with an elevation of only about 1200 m instead of the real 2351 m.

3.2.2 Wind Shear Intensity Factor I Definition

The severity of wind shear intensity, as perceived by the aircraft, can be quantified according to the wind shear intensity factor "I", detailed in ICAO's (International Civil Aviation Organization) Manual on Low-level Wind Shear [57]. Following [57] and Guan and Yong [17], wind shear is classified as "light", "moderate", "strong" or "severe" based on the variation of the airspeed with time $\frac{dV_{TAS}}{dt}$ and on the airspeed proportion $\frac{\Delta V_{TAS}}{V_{TAS}}$. The intensity factor I itself may be expressed as follows:

$$I = \frac{dV_{TAS}}{dt} \cdot \left(\frac{\Delta V_{TAS}}{V_{TAS}}\right)^2 . \tag{3.5}$$

The computation of the true airspeed, V_{TAS}, is based on the following relation:

$$GS = V_{TAS} + V_{HT}, \tag{3.6}$$

where GS represents the ground speed of the aircraft and was computed by employing the three-dimensional distance formula between any two points described by their altitude and geographic coordinates (latitude and longitude), see Eq. (3.7). The head or tailwind component (see Eq. 3.1 and 3.2 and Figure 3.1) is then subtracted from the ground speed to obtain the true airspeed.

More specifically, the ground speed was estimated according to the following relation for a time interval Δt:

$$GS = \frac{d_{path}}{\Delta t}. \tag{3.7}$$

The length described by d_{path} is the straight-line distance an aircraft travels between two points in space each defined by an altitude h, a longitude χ and a latitude ϕ in a spherical coordinate system on the Earth with a radius $R_{\oplus}$. An illustration of this variable is provided in Figure 3.5.

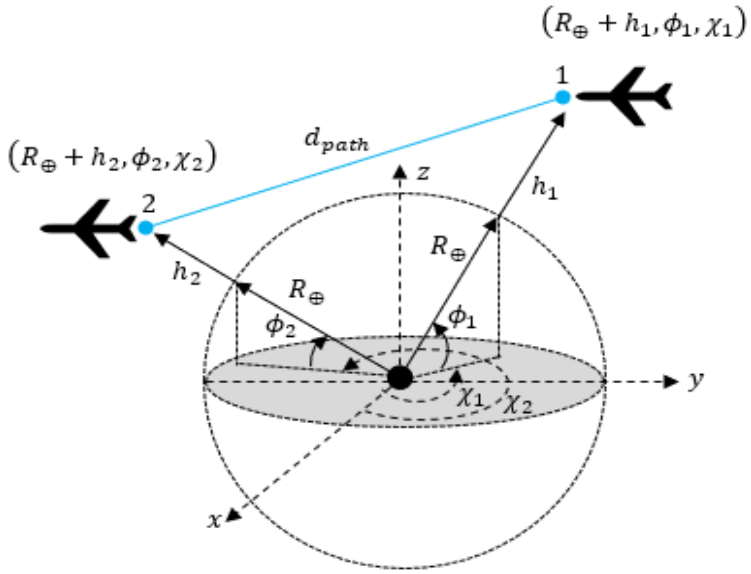

Figure 3.5: Calculation of flight path.

Figure 3.5 illustrates the position of an aircraft at a point 1 and then later at a point 2 in terms of spherical coordinates. In order to compute d_{path}, it is first necessary to convert this information to a point (x_i, y_i, z_i) in a rectangular reference frame xyz as is shown by Eqs. (3.8).

$$x_i = \left(R_{\oplus} + h_i\right)\cos(\phi_i)\cos(\chi_i) \tag{3.8a}$$

$$y_i = \left(R_{\oplus} + h_i\right)\cos(\phi_i)\sin(\chi_i) \tag{3.8b}$$

$$z_i = \left(R_{\oplus} + h_i\right)\sin(\phi_i) \tag{3.8c}$$

Once two coordinates at positions 1 and 2 are expressed in this form, the distance d_{path} is found by simply making use of the distance formula in 3D space:

$$d_{path} = \sqrt{(x_1 - x_2)^2 + (y_1 - y_2)^2 + (z_1 - z_2)^2}. \tag{3.9}$$

Once $\frac{dV_{TAS}}{dt}$ and $\frac{\Delta V_{TAS}}{V_{TAS}}$ are known, the wind shear intensity may be classified by consulting the proper boundaries specified in Figure 3.6. In both flights, this was performed for altitudes approximately below 2000

ft (610 m), which according to Guan and Yong [17], represent the appropriate range for low-level wind shear considerations.

Woodfield and Woods [27] first suggested the wind shear intensity factor "I", which was based upon the scrutiny of more than 9000 British Airways flights with a Boeing 747 (aircraft details in Appendix A5). Their findings are mapped in Figure 3.6. Their research showed that the classification of wind shear intensity via the "I" factor was more coherent with pilot reports than the method suggested by Eq. (3.4).

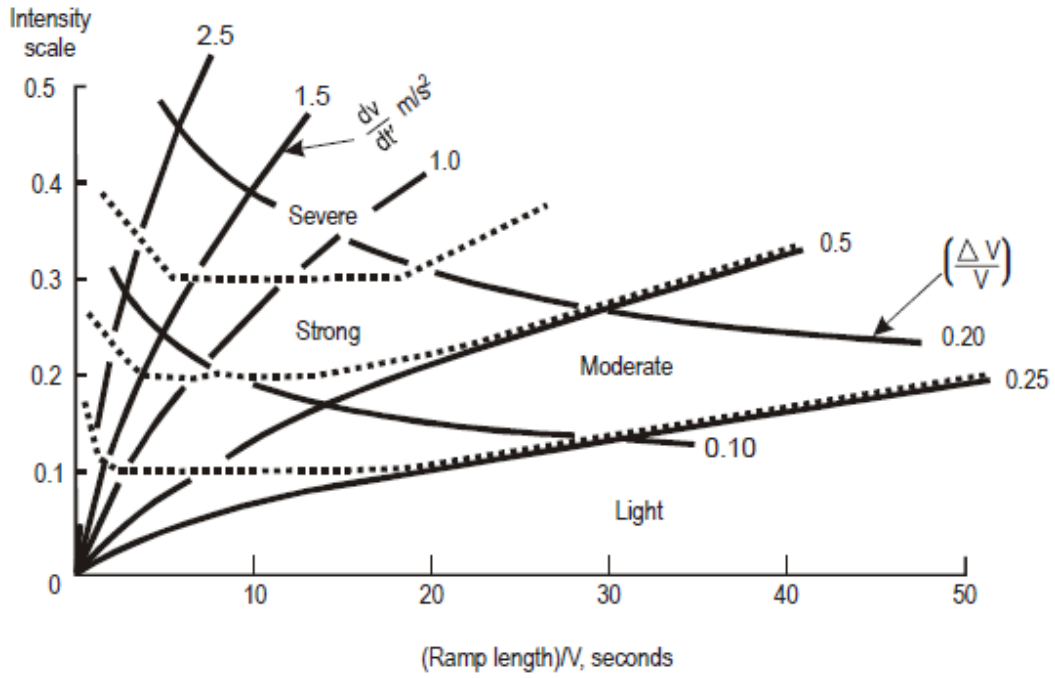

Figure 3.6: Boundaries for the classification of wind shear intensity as recommended by the ICAO Manual on Low-Level Wind Shear [57] and originally proposed by Woodfield and Woods [27].

3.2.3 F-factor Definition

Like the wind shear intensity "I", the F-factor or wind shear hazard factor is an alternative indicator that quantifies the danger level associated with wind shear, as perceived by an aircraft [58]. The index itself was proposed by Bowles and Hinton [59] and implemented by both the National Aeronautics and Space Administration (NASA) and the Federal Aviation Administration (FAA) in onboard wind shear alert systems [57]. It represents the rate at which an aircraft's energy varies in the presence of wind shear [60].

The F-factor is derived according to the total energy of an aircraft assuming contributions in terms of gravitational potential and kinetic energies. The specific total aircraft energy e_T is thus given as:

$$e_T \equiv \frac{E_T}{W} = z + \frac{V_a^2}{2g}, \tag{3.10}$$

with V_a equaling the aircraft airspeed and W its weight.

Taking the derivative of (3.10) with respect to time t leads to (3.11) as shown:

$$\frac{de_T}{dt} \equiv \dot{e}_T = \dot{z} + \frac{V_a}{g}\dot{V}_a. \tag{3.11}$$

The equations of motion must now be obtained and replaced into (3.11). Mulgund and Stengel [61] provide a useful drawing of forces acting on an aircraft in flight, which is shown in Figure 3.7.

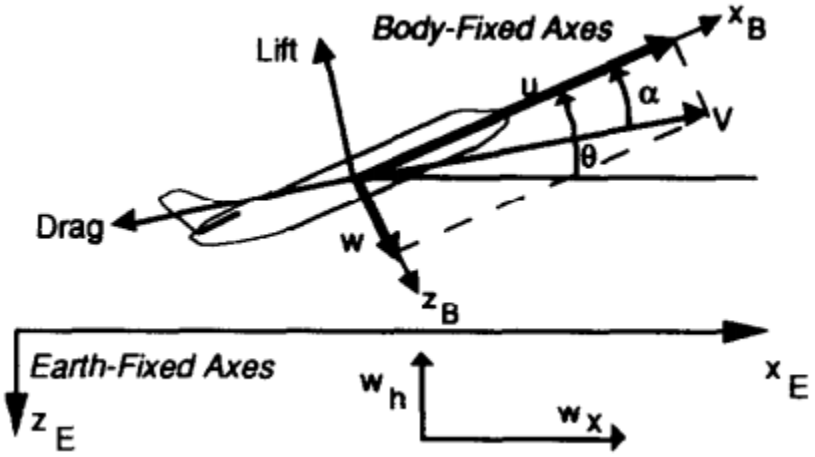

Figure 3.7: Aircraft force balance diagram, from Mulgund and Stengel [61].

This figure shows a generic aircraft with an angle of attack α, pitch angle θ, and weight W. In this particular case, the headwind component is labeled w_x and the up or downdraft component is w_h. The thrust T is directed along the axis x_B. The flight path angle γ (not shown in Figure 3.7) is the difference between θ and α.

A relevant kinematic relation to obtain an expression for the F-factor is that of the climb rate $\dot{z}$ from equation (3.11) [61]:

$$\dot{z} = V_a \sin\gamma + w_h. \tag{3.12}$$

According to [61], the application of Newton's second law to the forces involved in Figure 3.7 will then lead to:

$$\dot{V}_a = \frac{T\cos\alpha - D}{m} - g\sin\gamma - \dot{w}_x\cos\gamma - \dot{w}_h\sin\gamma\,. \tag{3.13}$$

Note that the second and third terms in (3.13) are negative since the inertial reference frame fixed to the Earth has a positive direction downwards. By substituting (3.12) and (3.13) into (3.11), one obtains the following results:

$$\dot{e}_T = V_a\sin\gamma + w_h + \frac{V_a}{g}\left[\frac{T\cos\alpha - D}{m} - g\sin\gamma - \dot{w}_x\cos\gamma - \dot{w}_h\sin\gamma\right]$$

$$\dot{e}_T = V_a\left(\sin\gamma + \frac{w_h}{V_a}\right) + V_a\left[\frac{T\cos\alpha - D}{mg} - \sin\gamma - \frac{\dot{w}_x}{g}\cos\gamma - \frac{\dot{w}_h}{g}\sin\gamma\right]$$

$$\dot{e}_T = V_a\left[\frac{T\cos\alpha - D}{mg} - \frac{\dot{w}_x}{g}\cos\gamma - \frac{\dot{w}_h}{g}\sin\gamma + \frac{w_h}{V_a}\right]. \tag{3.14a}$$

By factoring out a negative sign from equation (3.14a), the previous expression becomes:

$$\dot{e}_T = V_a\left[\frac{T\cos\alpha - D}{mg} - \underbrace{\left(\frac{\dot{w}_x}{g}\cos\gamma + \frac{\dot{w}_h}{g}\sin\gamma - \frac{w_h}{V_a}\right)}_{F-factor}\right], \tag{3.14b}$$

where the instantaneous F-factor was defined by Mulgund and Stengel [61] as follows:

$$F = \frac{\dot{w}_x}{g}\cos\gamma + \frac{\dot{w}_h}{g}\sin\gamma - \frac{w_h}{V_a}. \tag{3.15a}$$

The sign convention used to obtain Eq. 3.15a assumed that a headwind would be a positive quantity. However, in the current study and in other known works, the opposite is many times considered so that Eq. 3.15a should take the following form:

$$F = \frac{\dot{w}_x}{g}\cos\gamma - \frac{\dot{w}_h}{g}\sin\gamma + \frac{w_h}{V_a}. \tag{3.15b}$$

Guan and Yong [17] note that according to Eq. 3.14b, it is evident that when $F > 0$ the total energy of the aircraft is reduced and in such situations the wind shear is said to have a detrimental influence on its performance. This obviously implies that a negative F-factor is considered to be “performance-increasing” in the words of Mulgund and Stengel [61] as there is more climb energy available. An F-factor of 0.1, for instance, implies that an aircraft must generate an excess specific thrust ratio with this same value in order to preserve, at a constant speed, a level flight [60].

In order to apply equation (3.15b) to real data it is of utmost practicality to employ simplifying approximations first. Typically, the flight path angle γ is taken to be small so that Eq. 3.15b further simplifies to the following expression [59]:

$$F \approx \frac{\dot{w}_x}{g} + \frac{w_h}{V_a}. \tag{3.16}$$

From Eq. 3.16 it is possible to use yet another approximate form, which was once adopted by Proctor *et al.* [58] and is also used in wind shear alert systems in aircraft [17].

$$F \approx F_H\left(1 + \frac{g\beta H}{V_a^2}\right) \tag{3.17a}$$

$$F_H = \frac{\dot{w}_x}{g} \approx \frac{V_a}{g}\frac{\partial w_x}{\partial x} \tag{3.17b}$$

The approximation to parameter F_H that is written in terms of the rate of change of the headwind component with horizontal distance, as is shown in (3.17b), will be used to estimate the instantaneous F-factor from airborne data. H refers to a reference altitude. The β parameter is a function of F_H and is defined as:

$$\beta = \begin{cases} 1, F_H < 0 \\ 2, F_H > 0 \end{cases}. \tag{3.18}$$

Proctor *et al.* [58] note that oscillations of the instantaneous F-factor to large positive and negative values, in association with turbulence in the PBL (Planetary Boundary Layer), do not necessarily cause a significant deterioration in flight path since they are not sustained throughout long enough distances or time period. For this reason, instantaneous F-factor presented by Eqns. 3.17 should be averaged over a certain length L to properly categorize the hazard level of a shear event, as follows, to obtain the averaged F-factor $\bar{F}$:

$$\bar{F}(L) = \frac{1}{L}\int_{x}^{x+L} F ds\,. \tag{3.19}$$

The discretized form of Eq. (3.19) for a finite set of in-flight observations is expressed as a moving average in which the horizontal distance covered by the aircraft in each averaging window is approximately 1 km [60]:

$$\bar{F} = \frac{1}{N_w}\sum_{i=m}^{n} F_i\,, \tag{3.20}$$

where N_w is the number data points in a window w (beginning with the m-th observation and ending with the n-th point) such that a length of about 1 km is covered.

Several different aircraft types were analyzed (most were conventional jet transports) in order to arrive at the conclusion that $\bar{F} \geq 0.12$ [60] should be used as a wind shear alert. The FAA, however, considers that 0.13 should be the critical alert threshold for the 1-km averaged F-factor. Onboard wind shear alert systems emit a warning whenever this value is surpassed [58]. A value of 0.1, however, is already typically considered hazardous [60] and in Chapter 4, a situation in which $\bar{F} \geq 0.1$ will be deemed perilous.

3.3 Turbulence Predictors

The five turbulence indicators (Brown, Ellrod TI1, Ellrod TI2, CAT1 and EDR) as well as the three Froude numbers introduced in Section 2.2.1 were computed using forecast data from the AROME model. Relevant input parameters were procured from AROME via a two-step approach to find the most adequate corresponding value for a given airborne observation:

1. The absolute difference between all AROME levels for each recorded flight altitude, expressed as $\left|\mathrm{Altitude}_{\mathrm{Flight}} - \mathrm{Altitude}_{\mathrm{AROME}}\right|$, is computed and the level with the minimum difference is selected as the best match. This process is repeated for each available flight altitude.

2. Once every flight altitude is paired with an AROME level, a latitude and longitude pair must be chosen at each one of these correspondences. Following a similar logic, the best coordinate pair from the model is deemed to minimize the distance relative to the flight coordinates at each altitude.

Wind data and other parameters may be obtained once search parameters in the form $(Altitude, Latitude, Longitude)_{AROME}$ are available for every observed flight altitude.

3.3.1 Brown Index Φ

According to Gill and Buchanan [62] and Sharman *et al*. [63], the first version of the Brown Index, Φ, is defined as:

$$\Phi = \sqrt{0.3\zeta_a^2 + \left(\frac{\partial v}{\partial x} + \frac{\partial u}{\partial y}\right)^2 + \left(\frac{\partial u}{\partial x} - \frac{\partial v}{\partial y}\right)^2}, \qquad \zeta_a = \left(\frac{\partial v}{\partial x} - \frac{\partial u}{\partial y}\right) + f \tag{3.21a}$$

with u and v denoting the zonal and meridional components of the wind respectively. The vertical component of absolute vorticity, represented by ζ_a, is the sum of the vertical component of the relative vorticity, $\left(\frac{\partial v}{\partial x} - \frac{\partial u}{\partial y}\right)$, and of the Coriolis frequency, represented by f. The form used in the present work, Φ_ε, is expressed as energy dissipation in the following manner:

$$\Phi_\varepsilon = \frac{1}{24}\Phi S_V^2, \qquad S_V = \sqrt{\left(\frac{\partial u}{\partial z}\right)^2 + \left(\frac{\partial v}{\partial z}\right)^2} \tag{3.21b}$$

where S_V is the vertical wind shear.

3.3.2 Ellrod TI Indexes

As is mentioned in [62], the Ellrod indicators can be used to quantify turbulence. The first version, Ellrod TI1, is defined as:

$$\text{Ellrod TI1} = \mathrm{S_v}\sqrt{\left(\frac{\partial u}{\partial x} - \frac{\partial v}{\partial y}\right)^2 + \left(\frac{\partial v}{\partial x} + \frac{\partial u}{\partial y}\right)^2}. \tag{3.22}$$

The Ellrod TI2 index is similar to the Ellrod TI1, except that it incorporates a convergence term in the form of $-\left(\frac{\partial u}{\partial x} + \frac{\partial v}{\partial y}\right)$, as is shown in Eq. 3.23:

$$\text{Ellrod TI2} = \text{S}_\text{v}\left[\sqrt{\left(\frac{\partial u}{\partial x}-\frac{\partial v}{\partial y}\right)^2+\left(\frac{\partial v}{\partial x}+\frac{\partial u}{\partial y}\right)^2}-\left(\frac{\partial u}{\partial x}+\frac{\partial v}{\partial y}\right)\right]. \tag{3.23}$$

3.3.3 CAT1 Indicator

The CAT1 turbulence indicator, as is denoted in this study, is referred to as "MOS (Model Output Statistics) probability forecast" by Sharman *et al.* [63] and is defined as:

$$\text{CAT1} = \left|\vec{V}_h\right|\sqrt{\left(\frac{\partial u}{\partial x}-\frac{\partial v}{\partial y}\right)^2+\left(\frac{\partial v}{\partial x}+\frac{\partial u}{\partial y}\right)^2}, \tag{3.24}$$

where $\vec{V}_h$ is the horizontal wind vector.

3.3.4 EDR (Eddy Dissipation Rate) Indicator

The Eddy Dissipation Rate, ε, may also be used as a quantifier for turbulence. The method of calculation for this parameter in the current study follows the empirical formula delineated in Frech *et al.* [64]:

$$\varepsilon = \frac{\text{TKE}^{1.5}}{L_e}, \tag{3.25}$$

where $L_e = 311m$, which is the chosen length scale [64]. TKE represents the turbulent kinetic energy, which is a prognostic variable from the AROME model. The EDR indicator itself, however, is defined as the cube root of ε according to ICAO [65]:

$$\text{EDR} = \varepsilon^{\frac{1}{3}}. \tag{3.26}$$

3.4 RMSE and MAE for Wind Speed and Direction

The quantitative comparison between observed (from aircraft) and forecast (from AROME) wind data is established using to the root mean square error (RMSE) and the mean absolute error (MAE). The calculation of the wind speed error, RMSE_WSPD, is performed following the method employed by Grubišić *et al.* [21] for a dataset with n points, as follows:

$$\text{RMSE}_\text{WSPD} = \sqrt{\frac{1}{n}\sum_{i=1}^{n}\left[\left|\vec{V}_h(i)\right|_{obs}-\left|\vec{V}_h(i)\right|_{sim}\right]^2}. \tag{3.27}$$

$\mathrm{MAE}_{\mathrm{WSPD}}$ is similarly defined as follows:

$$\mathrm{MAE}_{\mathrm{WSPD}} = \frac{1}{n}\sum_{i=1}^{n}\left|\left|\vec{V}_h(i)\right|_{obs} - \left|\vec{V}_h(i)\right|_{sim}\right|. \tag{3.28}$$

The root mean square error and the mean absolute error for the wind direction, $\mathrm{RMSE}_{\mathrm{WDIR}}$ and $\mathrm{MAE}_{\mathrm{WDIR}}$ respectively, are determined using the method described in Jiménez *et al.* [29]:

$$\mathrm{RMSE}_{\mathrm{WDIR}} = \sqrt{\frac{1}{n}\sum_{i=1}^{n}[\Delta_{\mathrm{WDIR}}(i)]^2}\,, \tag{3.29}$$

$$\mathrm{MAE}_{\mathrm{WDIR}} = \frac{1}{n}\sum_{i=1}^{n}|\Delta_{\mathrm{WDIR}}(i)|\,, \tag{3.30}$$

where $\Delta_{\mathrm{WDIR}}(i)$ in degrees is given by:

$$\Delta_{\mathrm{WDIR}}(i) = \begin{cases} \mathrm{WDIR}_{sim}(i) - \mathrm{WDIR}_{obs}(i); & |\mathrm{WDIR}_{sim}(i) - \mathrm{WDIR}_{obs}(i)| \leq 180 \\ \mathrm{WDIR}_{sim}(i) - \mathrm{WDIR}_{obs}(i) - 360; & \mathrm{WDIR}_{sim}(i) - \mathrm{WDIR}_{obs}(i) > 180 \\ \mathrm{WDIR}_{sim}(i) - \mathrm{WDIR}_{obs}(i) + 360; & \mathrm{WDIR}_{sim}(i) - \mathrm{WDIR}_{obs}(i) < -180 \end{cases}. \tag{3.31}$$

Chapter 4

Results and Discussion

This chapter begins by characterizing the synoptic background in which both Flights 1 and 2 were involved. Results based on aerial observations follow. Wind intensities registered by Pico Aerodrome are also included for verification of consistency with aircraft observations and AROME model predictions. Based on airborne data collected from both flights, a classification of wind shear intensity experienced by the aircraft is derived via the wind shear intensity factor I and F-factor. Outcomes from the five turbulence indicators mentioned earlier, computed from AROME forecasts, are then discussed and compared with in-flight data. Preliminary suggestions for turbulence thresholds are also included. The agreement between AROME wind predictions and wind data gathered by SATA aircraft is assessed via the objective scores for wind speed and wind direction. Lastly, upon globally considering all results, the likely cause for the hard landing incident that transpired during Flight 1 is provided.

4.1 Synoptic Scale Analysis

During Flight 1, the flow in Pico Island was influenced by the presence of a depression located northwest of the Azores and by a subtropical anticyclone to its west/southeast. Consequently, southwesterly winds of around 20 kt (10 m/s) were visible south of the island, according to an ECMWF depiction of that day (Figure 4.1). For Flight 2, an anticyclone was present south of the Azores, causing southwesterly winds of approximately 10 kt (5 m/s) south of Pico Island (Figure 4.2).

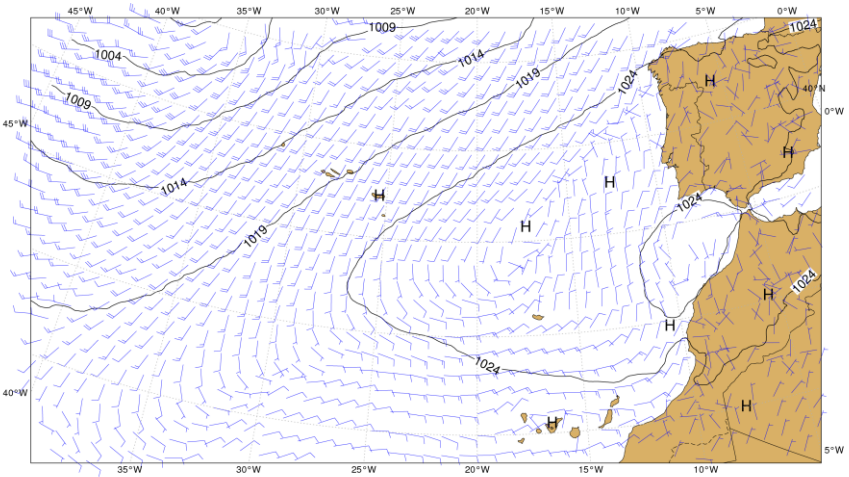

Figure 4.1: Mean sea level pressure (in hPa) and 10 m wind (kt) for Flight 1, based on ECMWF analysis.

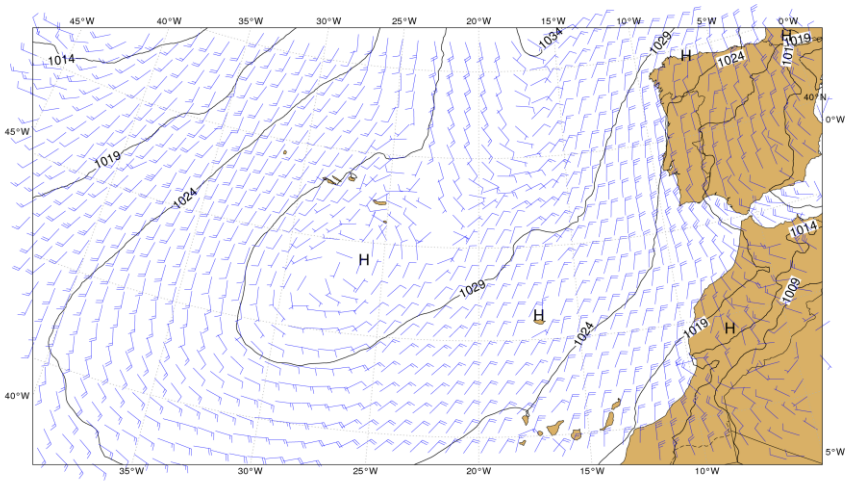

Figure 4.2: Mean sea level pressure (in hPa) and 10 m wind (kt) for Flight 2, based on ECMWF analysis.

4.2 Mesoscale Analysis

During Flight 1, the upstream conditions were characterized by a stable stratification, with N varying from 0.012 to 0.015 s^{-1} and by the absence of an inversion, as is confirmed by the absolute temperature profile in Figure 4.3 (a), showing a continuous decrease of temperature with height. The Froude number varies between 0.7 and 0.9 below 400 m, reaching a maximum value of 1.2 at about 1600 m (Figure 4.4), which coincides with a wind speed of nearly 18 m/s (Figure 4.3 (c)). Above this level, Fr varies between 1 and 1.2. Consistently, Fr and Fr_h are 0.95 and 0.9, respectively (Table 4.1). Therefore, according to previous studies [40-41], no wave breaking, upstream blocking or lee vortex formation are expected (see Figure 2.9 (b)). The critical heights (defined in Chapter 2) are 107 m or 60 m, depending on the method. Accordingly, it is expected that air flows nearly horizontally around the mountain below this level, while it will overcome the obstacle above it. Moreover, the parameter F_L is always below 0.08 in Figure 4.3 (c), so according to the analysis of F_L and the Froude number, vertically propagating waves are expected [39].

During Flight 2, the upstream conditions are characterized by the presence of a short inversion close to 3000 ft (872 m), where N varies between 0.015 and 0.018 s^{-1} (Figure 4.3 (b)). The Froude number has values smaller than 0.6 below 2 km (Figure 4.4). Consistently, Fr and Fr_h are 0.42 and 0.31, respectively (Table 4.1). According to the flow regime diagram presented in Figure 2.10, flow splitting and lee vortex formation with reversed flow are predicted. Figure 4.3 (d) also shows that $F_L \leq 1$ for all heights below 2000 ft, which implies that gravity waves may develop.

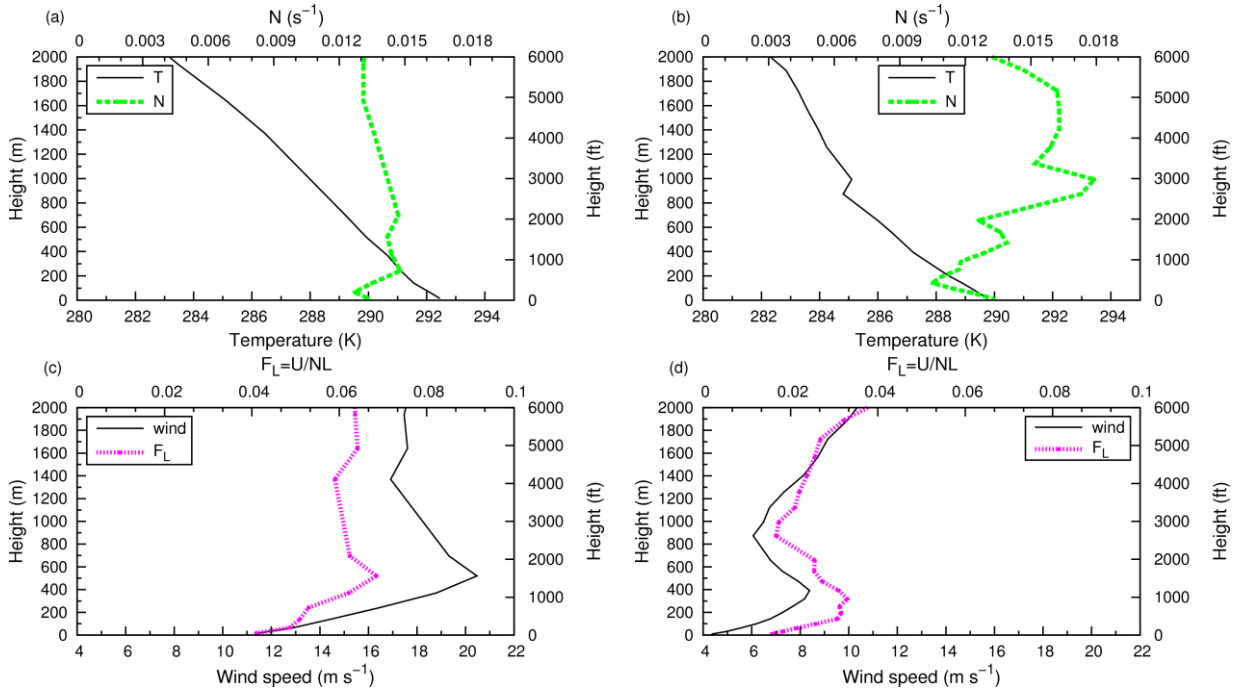

Figure 4.3: Absolute temperature and buoyancy frequency profiles at point C in Figure 3.4 for: (a) Flight 1; (b) Flight 2. Wind and F_L profiles at point C for: (c) Flight 1; (d) Flight 2.

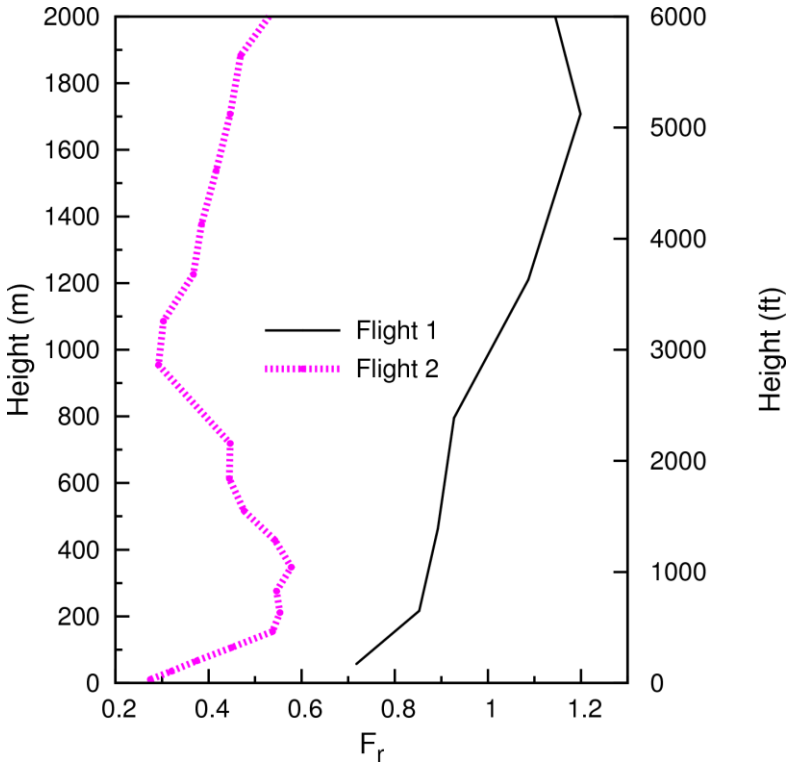

Figure 4.4: Froude number vertical profile for both flights.

Table 4.1: Froude number and related results by flight for Point C in Figure 3.4 with h_{c1},h_{c2} and z_i in meters.

Parameter	Flight 1	Flight 2
Fr (Eq. 2.8)	0.95	0.42
$\mathbf{Fr_h}$ (Eq. 2.11)	0.90	0.31
$\mathbf{Fr_i}$ (Eq. 2.12)	∞	0.92
$\boldsymbol{h_{c1}}$ (Eq. 2.10)	107	855
$\boldsymbol{h_{c2}}$ (Eqs. 2.8, 2.11)	60	696
$\boldsymbol{z_i}$	-	872

These parameters were derived from AROME forecasts.

4.3 Results from Observations

4.3.1 Aerodrome Wind Data

At the LPPI Aerodrome, wind was predominant from the southwest at two instants close to the time of both flights (Table 4.2). A headwind (W_{HD}) of 12/13 kt (6/7 m/s) and a crosswind (W_{CH}) of 14/16 kt (7/8 m/s) were registered on the day of Flight 1. In regard to gusts, the aircraft experienced a headwind (GW_{HD}) of 18/20 kt (9/10 m/s) and a crosswind (GW_{CH}) of 21/24 kt (11/12 m/s) incoming from the left. The wind was also from the southwest during Flight 2 with considerably weaker intensities than Flight 1. The headwind was around 4/6 kt (2/3 m/s), about half of what was reported in Flight 1, with crosswinds at 10/12 kt (5/6 m/s).

Table 4.2: Wind data (velocity in knots) based on METAR (Meteorological Aerodrome Reports) at Pico Aerodrome at the time of both flights. The crosswind (W_{CH}) is from the left if negative. Negative values of W_{HD} indicate headwinds.

	Wind Direction	Wind Speed	Gust	$\boldsymbol{W_{HD}}$	$\boldsymbol{W_{CH}}$	$\boldsymbol{GW_{HD}}$	$\boldsymbol{GW_{CH}}$
Flight 1	220°	18	28	-12	-14	-18	-21
	220°	21	31	-13	-16	-20	-24
Flight 2	200°	13	-	-4	-12	-	-
	210°	12	-	-6	-10	-	-

4.3.2 Characterization of Wind Profiles

The wind speed profile based on airborne observations along its path (see Figure 3.4) is presented in Figure 4.5, for Flights 1 and 2. During Flight 1, the aircraft experienced strong winds oscillating between 10 kt (5 ms^{-1}) and nearly 40 kt (21 ms^{-1}). At 440 ft (107 m), for instance, the aircraft experienced a wind of 38 kt (19.5 ms^{-1}). During Flight 2, a low-level jet is present with a maximum intensity of nearly 22 kt (11 ms^{-1}) at 600 ft (183 m). Above 1000 ft (305 m), the wind is weak (below 8 kt or 4 ms^{-1}). During both flights, the wind is predominantly from the southwest below 1500 ft or 457 m (Figure 4.23).

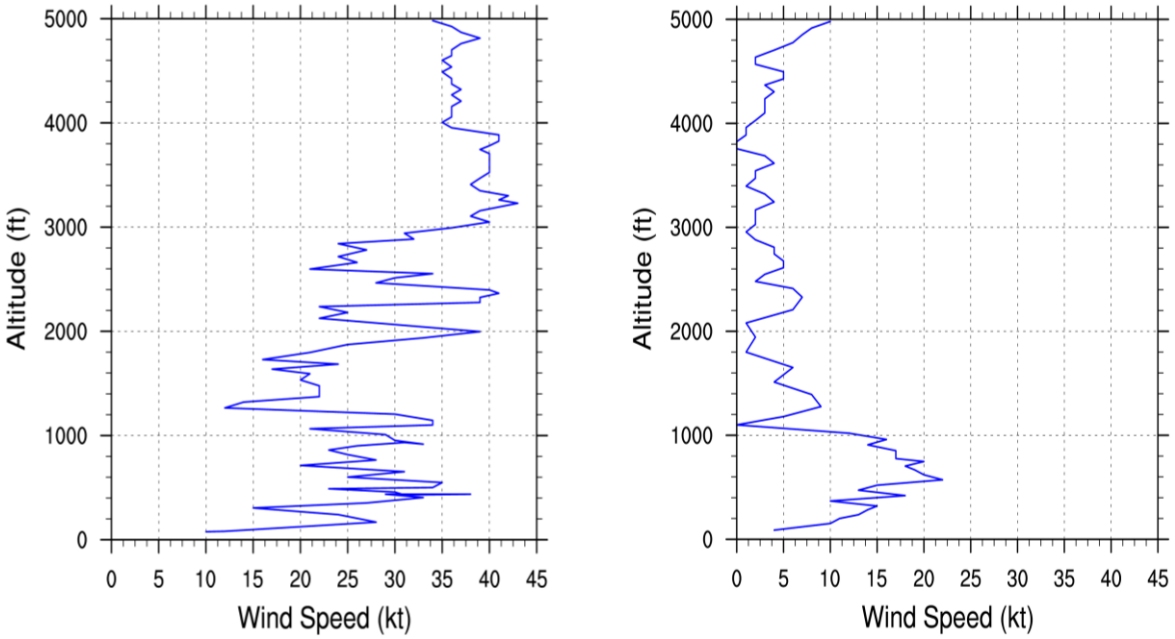

Figure 4.5: Wind intensity profile below 5000 ft (1524 m) for: (a) Flight 1; (b) Flight 2, along the flight path.

When compared to intensities registered by the Aerodrome (Table 4.2), it appears that the aircraft registered slightly more elevated wind speeds at about 27 kt near ground level relative to the 18/21 kt speeds of the Aerodrome. For Flight 2, the aircraft recorded less intense winds of 4 kt compared to 12/13 kt of the Aerodrome.

4.3.3 Wind Shear Intensity Factor *I* Results

Figures 4.6 (a) and (b) detail the relative frequency distributions in both flights for altitudes only below 2100 ft (640 m) in order to focus on the effects of low-level wind shear as is suggested in [17]. During Flight 1, about 36% of the approach phase was carried out under “severe” wind shear conditions and over 15% under “strong” wind shear conditions. In other words, more than 50% of the time the aircraft experienced “strong” to “severe” wind shear, consistently with the occurrence of the hard landing incident. During Flight 2, “severe” wind shear conditions were absent, with only 4% being classified as “strong” and nearly 29% as “moderate” (Figure 4.6 (b)). Table 4.3 lists wind shear levels of the first three lowest altitudes as functions of the variation of airspeed $\frac{dV}{dt}$ and of the ratio $\frac{\Delta V}{V}$ for both flights. By comparing them, it is clear that close to the ground, the hard landing incident (Flight 1) experiences at all three levels “severe” wind shear, whereas in Flight 2, a “light” intensity is prevalent. It is worth noting that since the boundaries for the I factor (Figure 3.6) were established based on a considerably larger aircraft, the B747 rather than the lighter A320 (comparison of key specifications in Table E), the intensities of Figure 4.6 may be slightly underestimated since the A320-200 is about five times less massive than the B747-200.

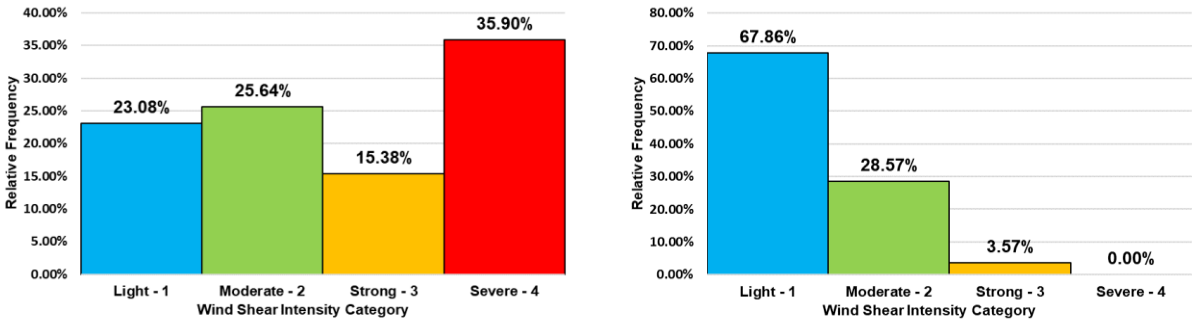

(a) **(b)**

Figure 4.6: Relative frequency per wind shear intensity category for: (a) Flight 1; and (b) Flight 2.

Table 4.3: Classification of wind shear intensity for the three lower altitudes in Flights 1 and 2.

	Altitude	$\frac{dV}{dt}(m/s^2)$	$\frac{\Delta V}{V}$	Classification	Rating
Flight 1	228 ft (69 m)	1.649	0.170	Severe	4
	164 ft (50 m)	8.820	0.476	Severe	4
	90 ft (27 m)	2.962	0.138	Severe	4
Flight 2	214 ft (65 m)	0.265	0.015	Light	1
	169 ft (52 m)	0.264	0.015	Light	1
	128 ft (39 m)	0.729	0.042	Moderate	2

4.3.4 F-factor Results

The F-factor was calculated using observed data from SATA aircraft, as described in Chapter 3. Firstly, for the instantaneous F-factor, the airspeed V_a shown in Eq. 3.17 (a) is computed using Eq. (3.6) by solving for V_{TAS}. The ground speed is computed via Eq. (3.7). The parameter F_H in (3.17 (b)) was determined as follows:

$$F_H = \frac{\dot{w}_x}{g} \approx \frac{V_a}{g}\frac{\partial w_x}{\partial x} \approx \frac{1}{g}\cdot\left(\frac{\Delta d_{path}}{\Delta t} - V_{HT}\right)\cdot\frac{\Delta V_{HT}}{\Delta d_{path}}. \tag{4.1}$$

Note that Δd_{path} is the distance the aircraft travels in an interval Δt (flight path) and is calculated according to Eq. (3.9) and $\Delta V_{HT} = V_{HT}(t_2) - V_{HT}(t_1)$ where $V_{HT}(t_i)$ is found by applying Eq. (3.1) at an instant t_i.

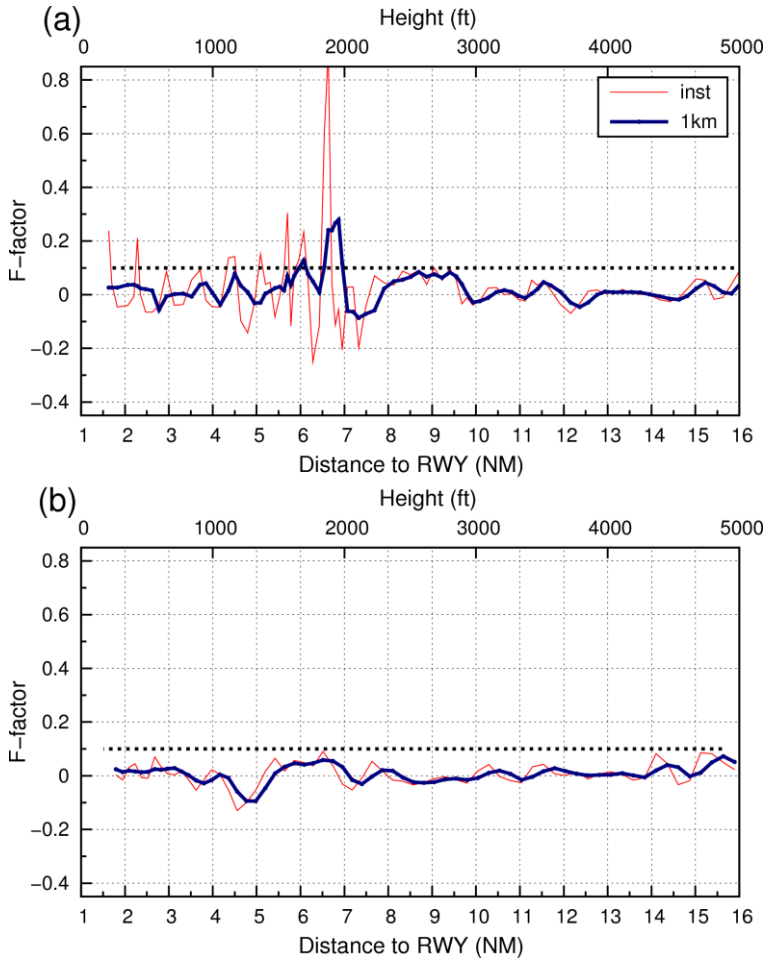

Figure 4.7: Instantaneous and 1-km averaged F-factors for (a) Flight 1 and (b) Flight 2. Dotted black line represents the 0.1 critical threshold.

Comparing Figures 4.7 (a) and (b), it is evident that the values attained during the hard landing incident (Flight 1) are unsurprisingly greater than during Flight 2. Globally, the maximum instantaneous F-factor for Flight 1 is significantly larger, close to 0.9 compared to values entirely below 0.1 for Flight 2. These large values during Flight 1 are consistent with the presence of turbulence in the PBL.

Based on 1-km averaged F-factor values, Flight 1 encountered “severe” or critical wind shear conditions between 6 and 7 NM from runway 27. This corresponds to altitudes varying between 1700 and 2000 ft. For Flight 2, as is expected, no alert should be given, since both the instantaneous and averaged F-factors are always below 0.1.

4.4 Results from AROME Forecasts

The orographic flow dynamics for each flight were characterized using AROME forecast data. Turbulence indicators are then compared to the wind shear intensity factor I and the averaged F-factor $\bar{F}$.

4.4.1 Characterization of Orographic Flow during Flight 1

The horizontal wind and vertical component of the absolute vorticity predicted by the AROME model are depicted in Figure 4.8 for Flight 1. At 30 m, the flow is partially deflected laterally (mostly on the west side), which is denounced by the curvature of the wind vectors. This deflection is still present at 200 m but is barely visible at 300 m (not shown), while at 500 m (Figure 4.8 (b)) it is no longer discernible at all. Empirically speaking, this implies that the critical altitude should lie somewhere between 200 and 300 m, revealing an underestimation of the values of h_c presented in Table 4.1.

Until 2800 ft (853 m), a pair of positive and negative vertical vorticities is visible over the mountain and on the leeward region, illustrated in Figure 4.8 (a) for a height of 30 m. However, no signs of reversed flow or vortex formation are present, which is consistent with the results of Bauer *et al*. [41] and Epifanio [40]. For this flight, $M = \frac{1}{0.95} = 1.05$ (see Table 4.1), so it is unsurprising that Figure 4.8 (a) resembles Figure 2.7 (b) from Smolarkiewicz and Rotunno [38] in which $M = 1.5$.

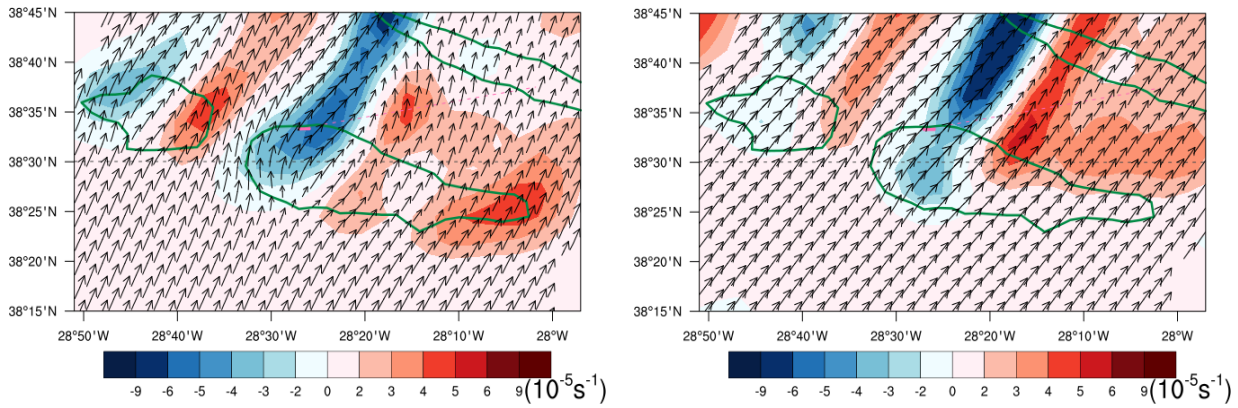

Figure 4.8: Absolute vorticity ζ_a and wind vectors for Flight 1 at an altitude of: (a) 30 m; (b) 500 m. Dark arrows represent wind vectors.

The horizontal wind speed at 680 ft (207 m) shows a stagnation area on the upstream region of Pico Mountain and a maximum wind speed (>40 kt or 21 m/s) over it with weak winds on the leeward side (Figure 4.9 (a)). This pattern is coherent with previous studies like in Bauer *et al.* [41] with their Figure 2.a2. Near Pico Aerodrome, AROME forecast winds with speeds above 35 kt (18 m/s). Ergo, during the approach to the Aerodrome the aircraft passes a region of elevated wind shear. Figure 4.9 (b) presents the maximum and minimum vertical velocity in the layer from the surface up to 6000 ft (1829 m), illustrating a wave pattern

over Pico and Faial Islands. Figure 4.10 (a) displays the vertical cross-section through the flight path in the approach phase (line A-B in Figure 3.4), showing that AROME forecasts the upward vertical velocity in the order of 100 ft/min (0.5 m/s) near 2000 ft (610 m) and a downward vertical velocity of 100-150 ft/min (0.50-0.76 m/s) near the Aerodrome. This is associated with pronounced vertically propagating waves that are caused by interference with Pico mountain, which are illustrated in Figure 4.10 (b) (up to 10000 ft or 3048 m) and Figure C (a) in Appendix A.3 (up to 42000 ft or 12802 m), where the higher values exceed 400 ft/min (2 m/s), and then propagate to the vicinity of the Aerodrome.

During Flight 1, the mean wind speed at point C (from Figure 3.4) is 12.76 m/s (U) and the average value of the buoyancy frequency is 0.0129 s^{-1} (N). Since the horizontal scale (L) for Pico Mountain is of the order of 21 km, then the condition for vertically propagating gravity waves ($N^2 > U^2k^2$) applies [1,35]. See also Figure 13.3 in Lynch and Cassano [35], which illustrates the alternating pattern between upward and downward motions associated with vertically propagating gravity waves.

An agreement between Smolarkiewicz and Rotunno's simulations [38] (Figure 2.7 (a)) and Figure 4.10 (b) is once again confirmed as both display the existence of vertically propagating waves for similar upstream conditions.

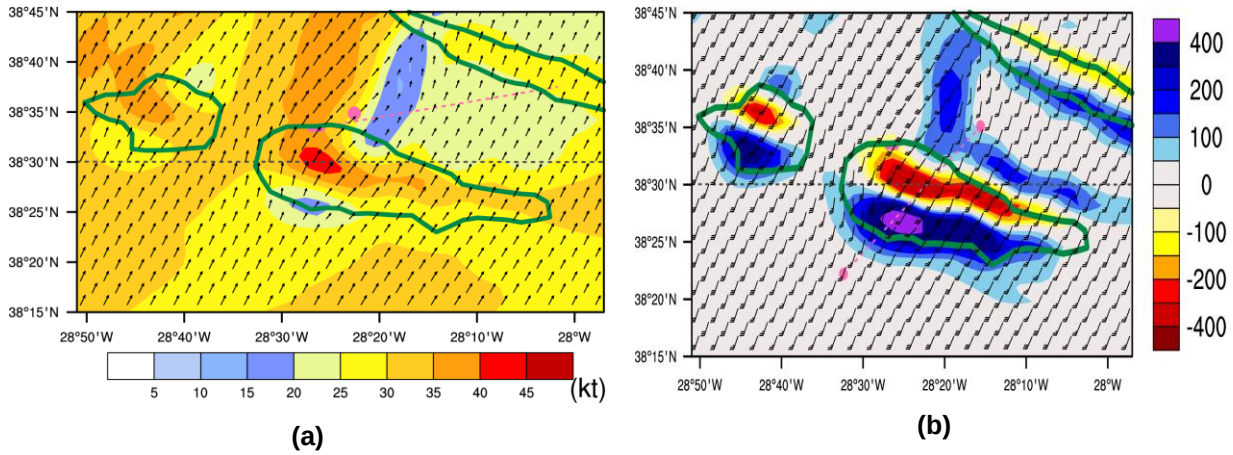

Figure 4.9: (a) Horizontal wind at 680 ft (207 m) for Flight 1; (b) Maximum vertical velocity under 6000 ft (1829 m) for Flight 1. Shading in (a) represents the wind speed in kt and the pink dot identifies the aircraft position at this level. Shading in (b) represents intensity in ft/min, positive values indicate upward vertical velocity and negative values represent downward vertical velocity.

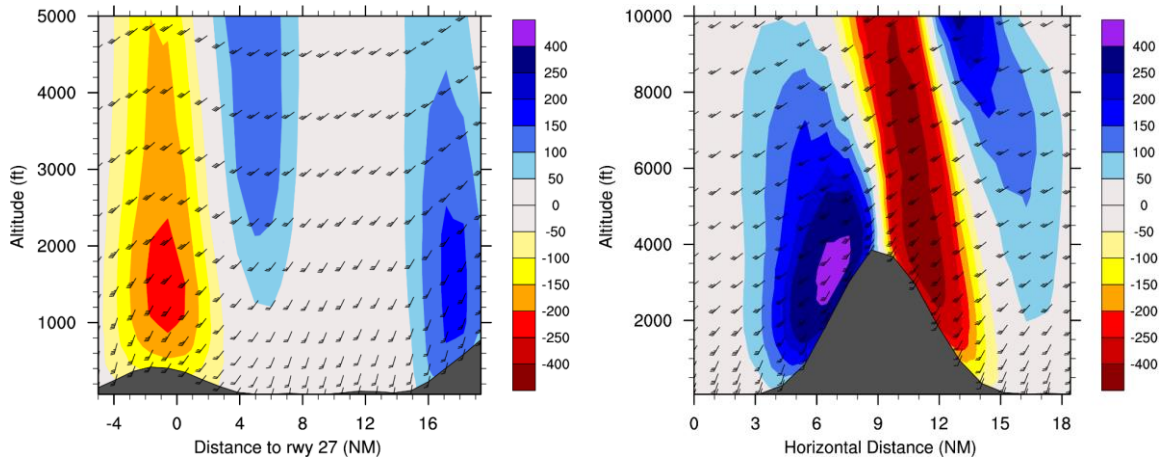

(a) **(b)**

Figure 4.10: Vertical cross-section of the vertical velocity through (a) line A-B on Figure 3.4 and (b) line C-D on Figure 3.4, for Flight 1. Shading represents intensity in ft/min, positive values indicate upward vertical velocity and negative values represent downward vertical velocity.

4.4.2 Characterization of Orographic Flow during Flight 2

The horizontal wind and vertical component of the absolute vorticity predicted by the AROME model at several heights are depicted in Figures 4.11 for Flight 2. Figure 4.11 (a) depicts a stagnation area in the windward direction of Pico Mountain and the occurrence of a flow splitting phenomenon in addition to a wake with reversed flow in the lee of the hill. This wake (at 40 m) consists of a pair of vortices, one with a clockwise rotation and negative absolute vorticity and another with a counter-clockwise rotation and positive vorticity. According to Table 4.1, $M = \frac{1}{0.42} = 2.38$ for this flight, so the presence of lee vortices is consistent with other studies. For instance, the wake structure exemplified in Figure 4.11 (a), which is visible below 600 m (not shown), resembles the results obtained by Smith and Grubišić [66] (p.3747) in their study of Hawaii's wake where it is described of comprising "two large, nearly steady vortices". A similar structure with a pair of counter-rotating vortices downstream of the obstacle was also documented by Smolarkiewicz and Rotunno [38] (see their Figure 1c and Figure 2.8 (b)) and by Epifanio [40] (their Figure 3c). Moreover, the regime flow diagram of Figure 2.10 in Chapter 2, which was used by Schär and Smith [47] and Grubišić *et al.* [21], accurately predicts a wake with reversed flow.

At higher levels, between 600 m and 850 m (Figures 4.11 (b) and (c)), no lee vortices are present and the dipole of positive and negative vorticities is weaker and shifted to the East relative to lower levels, mainly at 850 m. At 1100 m, the incoming flow is mainly from the west and overcomes the mountain (Figure 4.11 (d)). Finally, the analysis of Figure 4.11 suggests that the critical height in Flight 2 should be approximately 850 m, which is close to the estimate of the dividing streamline concept (see Table 4.1).

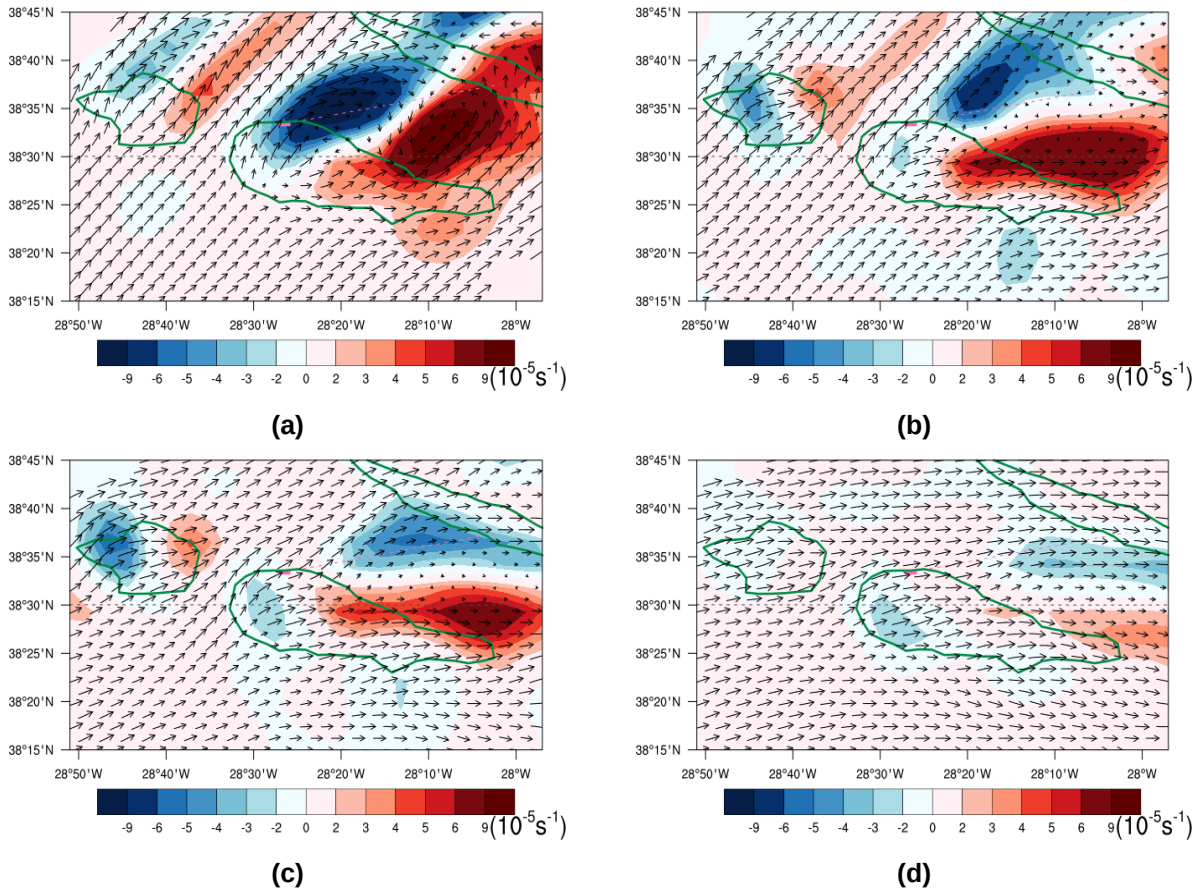

Figure 4.11: Absolute vorticity ζ_a and wind vectors for Flight 2 at an altitude of: (a) 40 m; (b) 640 m; (c) 850 m; (d) 1100 m. Dark arrows represent wind vectors.

The horizontal wind speed at 40 m is depicted in Figure 4.12 (a), which shows that near the aircraft position, the wind speed varies between 15 and 20 kt (8-10 m/s). It is also visible from this figure that the aircraft during the approach phase (pink dashed line) has passed through the wake. Figures 4.12 (a) and 4.13 also show signs of a vertically propagating mountain wave, however less energetic than the one seen on the day of Flight 1 (compared to Figure 4.12) and propagating to lower levels (up to 25000 ft or 7620 m), as is illustrated in Figure C (b) from Appendix A.3. During Flight 2, the maximum vertical velocity on the leeward side of Pico Mountain (Figure 4.13 (b)) is less than 200 ft/min (1 m/s), while during Flight 1 the maximum vertical velocity was above 400 ft/min (2 m/s). Upon propagation of this wave to the Aerodrome (Figure 4.13 (a)), it is seen that only a weak downdraft (less than 100 ft/min or 0.5 m/s) lies atop the Aerodrome with no hints of updrafts along the flight path. In Figure 4.13 (b), the reversed flow associated with the lee vortices is also visible until 2000 ft (610 m).

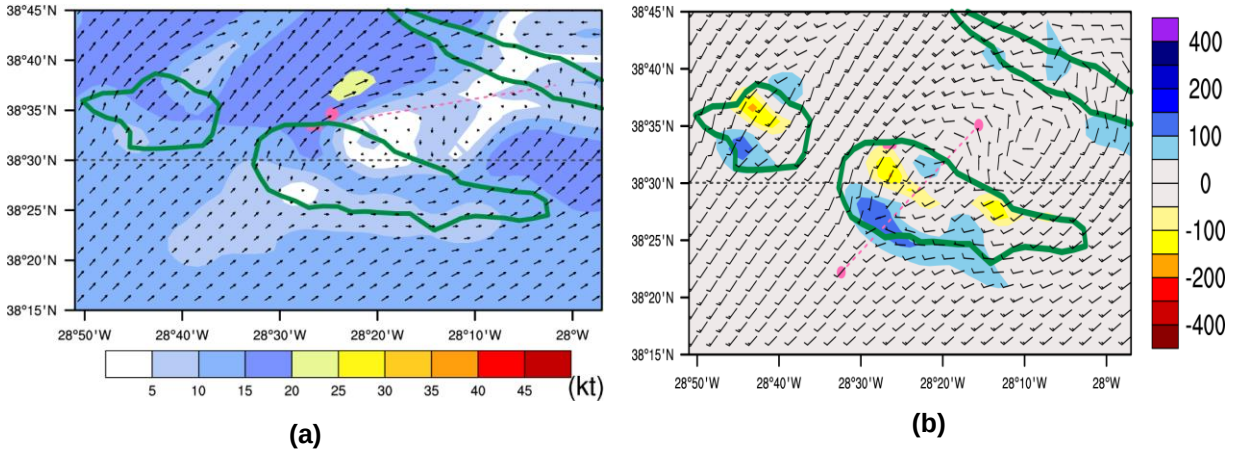

Figure 4.12: (a) Horizontal wind at 135 ft (40 m) for Flight 2.; (b) Maximum vertical velocity component under 6000 ft (1829 m) for Flight 2. Shading in (a) represents the wind speed in kt and the pink dot identifies the aircraft position at this level. Shading in (b) represents intensity in ft/min, positive values indicate upward vertical velocity and negative values represent downward vertical velocity.

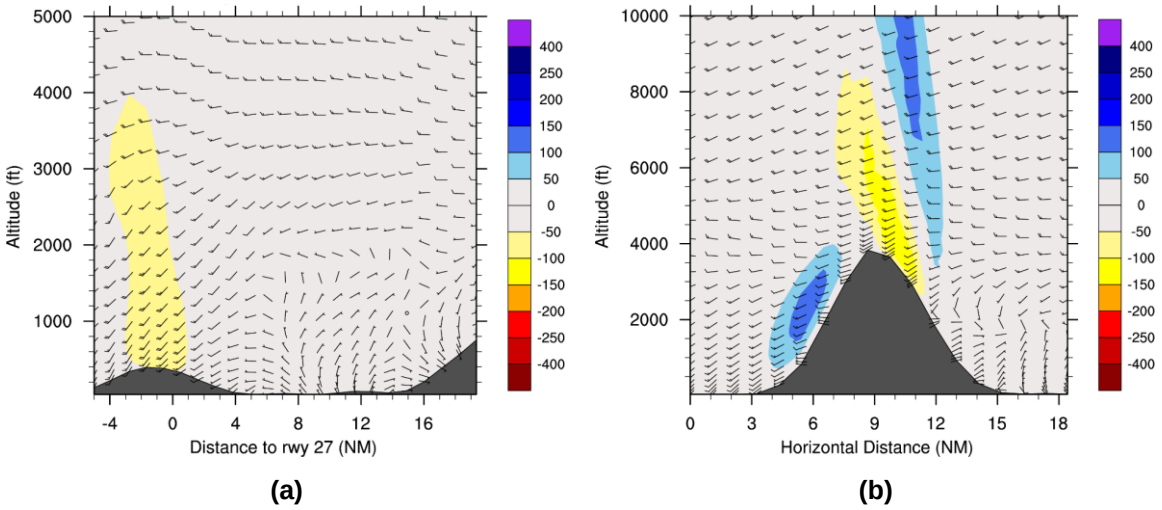

Figure 4.13: Vertical cross-section of the vertical velocity through (a) line A-B in Figure 3.4 and (b) line C-D in Figure 3.4, for Flight 2. Shading represents intensity in ft/min, positive values indicate upward vertical velocity and negative values represent downward vertical velocity.

4.4.3 Turbulence Indicator Results and Comparison

Turbulence indicators Ellrod TI2 and CAT1 at 66 m are presented in Figure 4.14 (a) and (b), for Flight 1. Both indicators show maximum values leeward of Pico mountain, with TI2 exceeding 18×10^{-6} s^{-2} and CAT1 exceeding 8×10^{-3} ms^{-2} in the proximity of the Aerodrome where the incident occurred. The cross-section along the flight path shows that for a distance less than 5 NM (9.3 km) of the runway, between 300 and 1600 ft, TI2 and CAT1 reach values above 18×10^{-6} s^{-2} and 8×10^{-3} ms^{-2}, respectively. Comparing the indicators with the wind shear Intensity Factor "*I*" (Figure 4.15 (a) and (b)), the aircraft experienced severe wind shear at these levels, suggesting that these values for TI2 and CAT1 could be tested as thresholds indicative of severe wind shear conditions. The Ellrod TI1 (shown in detail for both flights in Figures D1 (b), (d) and D2 (b), (d) in Appendix A.4) has a similar spatial pattern to TI2, but with lower values (Figure 4.15 (a)). The Brown index (shown in greater detail for both flights in Figures D1 (a), (c) and D2 (a), (c) in Appendix A.4) is maximum over land near the LPPI Aerodrome, exceeding 20×10^{-9} s^{-3} near the surface and decreasing drastically with height, reaching a value of 13×10^{-9} s^{-3} at 600 ft (Figure 4.15 (c)).

The EDR indicator shows a different pattern when compared to the other indicators. EDR shows higher values over land than over sea, depicting a maximum value above 0.4 $m^{2/3}$ s^{-1} near the top of Pico Mountain (Figure 4.16 (a)). At 66 m, EDR reaches a value between 0.35 and 0.4 $m^{2/3}$ s^{-1} near the Aerodrome (corresponding to moderate turbulence). Figure 4.16 (b) shows that along the flight path EDR decreases with height, varying from 0.35-0.4 $m^{2/3}$ s^{-1} near the surface to 0.15 to 0.2 $m^{2/3}$ s^{-1} at 2000 ft (610 m). It is interesting to mention that the thresholds applied in Figure 4.16 are lower than those presented in ICAO [65], but are those proposed recently [67], after a study by Sharman *et al.* [68] that showed that the thresholds in [65] are overestimated. According to [67], turbulence is severe when EDR ≥ 0.45 $m^{2/3}$ s^{-1} and is moderate for EDR between 0.2 and 0.45 $m^{2/3}$ s^{-1}. Comparing EDR to the wind shear Intensity Factor (Figure 4.15 (d)), it is clear that in the presence of severe wind shear conditions, EDR has values between 0.2 and 0.25 $m^{2/3}$ s^{-1} above 700 ft. For heights under 200 ft (61 m), EDR is close to 0.3, which suggests an underestimation of the "severe" wind shear conditions.

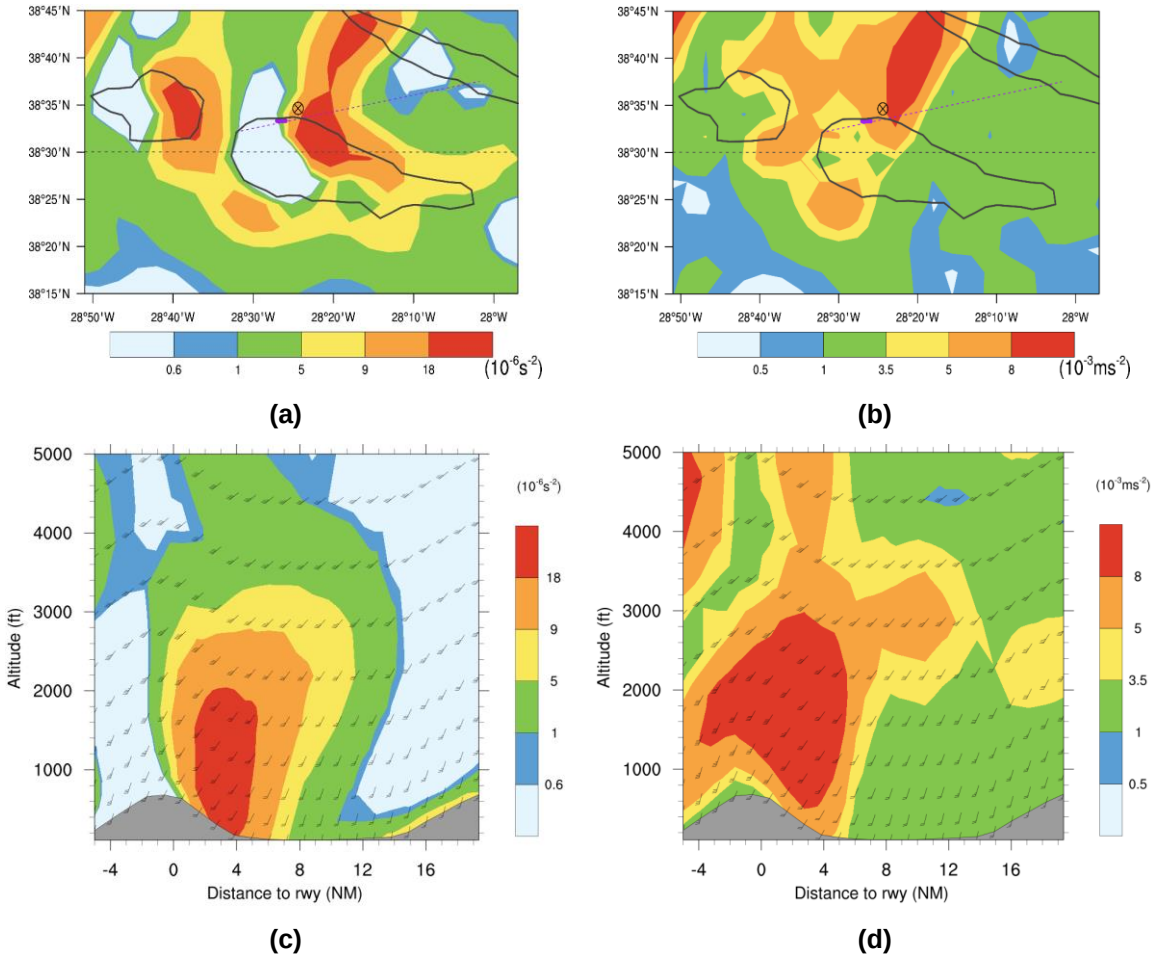

Figure 4.14: Horizontal variation of (a) Ellrod TI2 and (b) CAT1 at 66 m for Flight 1. Dotted pink line shows aircraft trajectory and pink bar locates the Aerodrome. The circled “x” mark identifies aircraft position at 66 m. Cross-sectional variation of (c) Ellrod TI2 and (d) CAT1 along flight path.

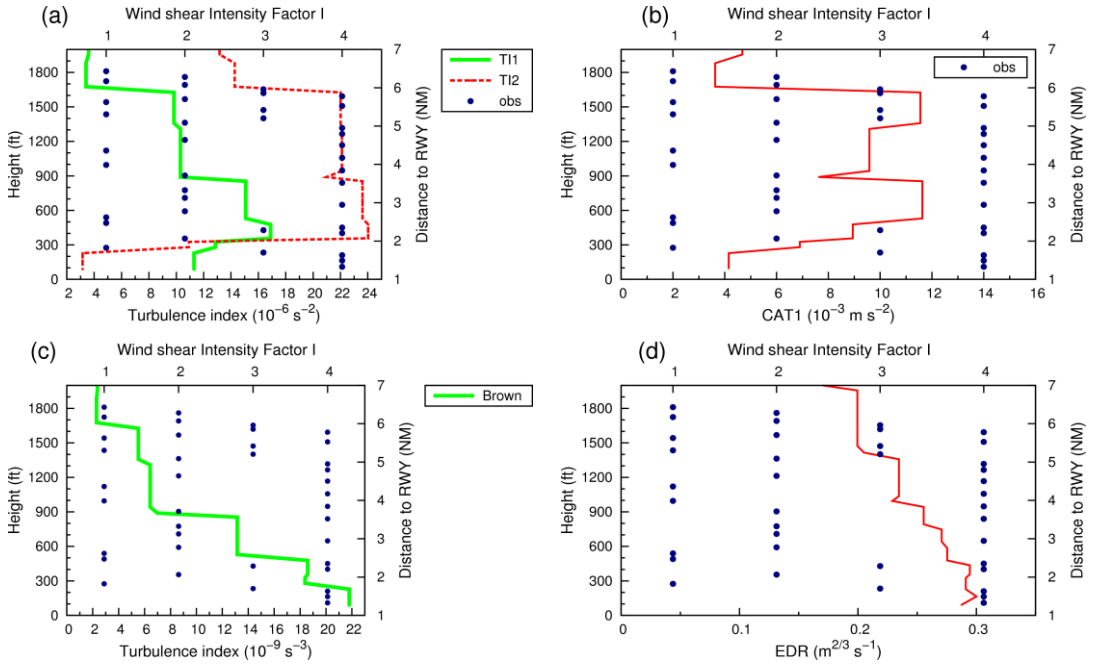

Figure 4.15: AROME turbulence indicators (bottom x-axis) vs. the wind shear intensity factor "*I*" (top x-axis), along the flight path during Flight 1.

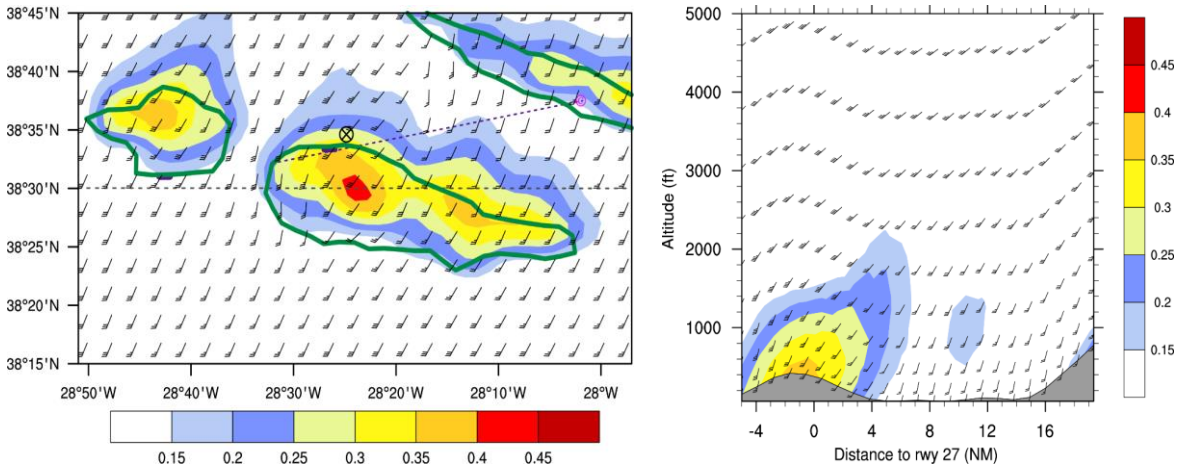

Figure 4.16: (a) Horizontal representation of EDR during Flight 1. The circled "x" mark identifies aircraft position at 66 m. (b) Cross-sectional representation of EDR along flight path. EDR in units of $m^{2/3}s^{-1}$.

During Flight 2, the index Ellrod TI2 shows maximum values in the leeward region of the mountain and exhibits a value of 9×10^{-6} s^{-2} near the aircraft position (Figure 4.17 (a)). The index CAT1 shows maximum values above 5×10^{-3} ms^{-2} downstream of Pico Aerodrome, close to the flight path (Figure 4.17 (b)). Along the flight path itself, Ellrod TI2 reaches values above 9×10^{-6} s^{-2} below 500 ft (152 m), while CAT1 attains values between 4×10^{-3} ms^{-2} and 8×10^{-3} ms^{-2} below 900 ft or 274 m (Figures 4.17 (c), (d) and 4.18), which are predominantly "moderate" wind shear conditions. The TI1 indicator is similar to TI2 and the Brown index decreases again drastically with height, exhibiting values below 4×10^{-9} s^{-3} for altitudes above 300 ft (91 m) (Figure 4.18).

Analysis of EDR depicts the occurrence of "light" turbulence near the Aerodrome (Figure 4.19). The "*l*" factor is mostly consistent with this categorization as wind shear conditions reach intensities that are predominantly "light" for heights between 200-500 ft (61-152 m). Nevertheless, in some instants the wind shear was classified as "moderate", while the EDR values above 400 ft are below 0.1 $m^{2/3}$ s^{-1} suggesting the absence of turbulence or wind shear (Figure 4.18 (d)).

This preliminary scrutiny of turbulence indicators suggests that CAT1, Ellrod TI2 and EDR could be applied together to arrive at a classification for the hazard level of turbulence. Moreover, preliminary thresholds for these indicators are proposed (Table 4.4), which should be subject to future validation, using more flight data.

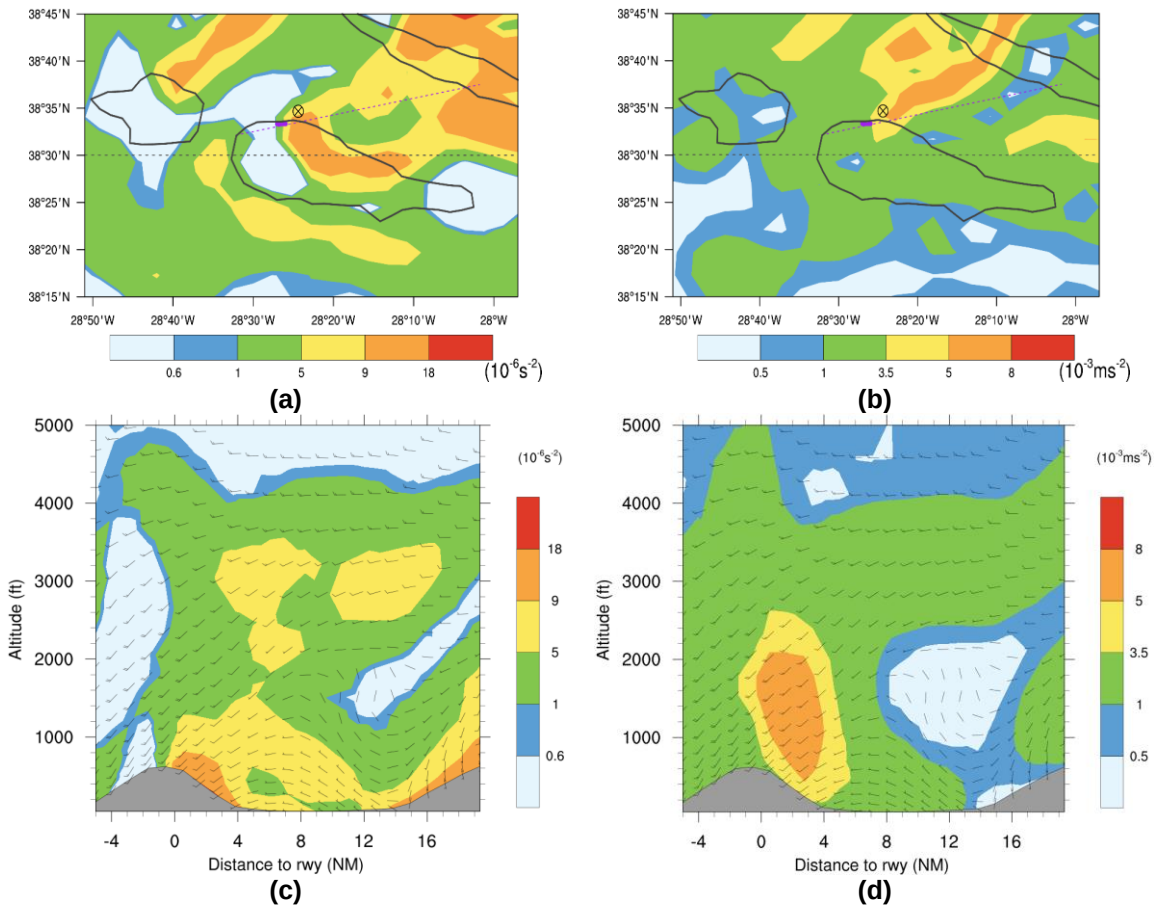

Figure 4.17: Horizontal variation of (a) Ellrod TI2 and (b) CAT1 at 66 m for Flight 2. Dotted pink line shows aircraft trajectory and pink bar locates the Aerodrome. The circled "x" mark identifies aircraft position at 66 m. Cross-sectional variation of (c) Ellrod TI2 and (d) CAT1 along flight path.

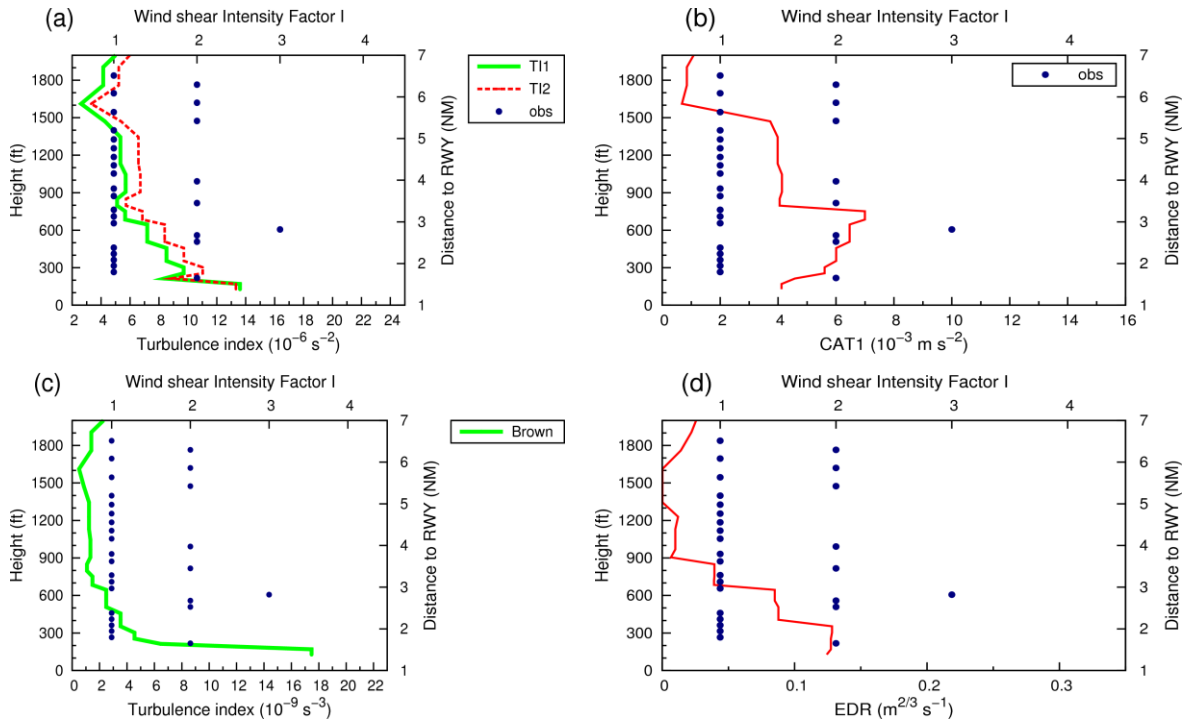

Figure 4.18: AROME turbulence indicators (bottom x-axis) vs. the Wind shear Intensity Factor *I* (top x-axis), along the flight path during Flight 2. The green dots indicate the Wind Shear Intensity Factor *I*.

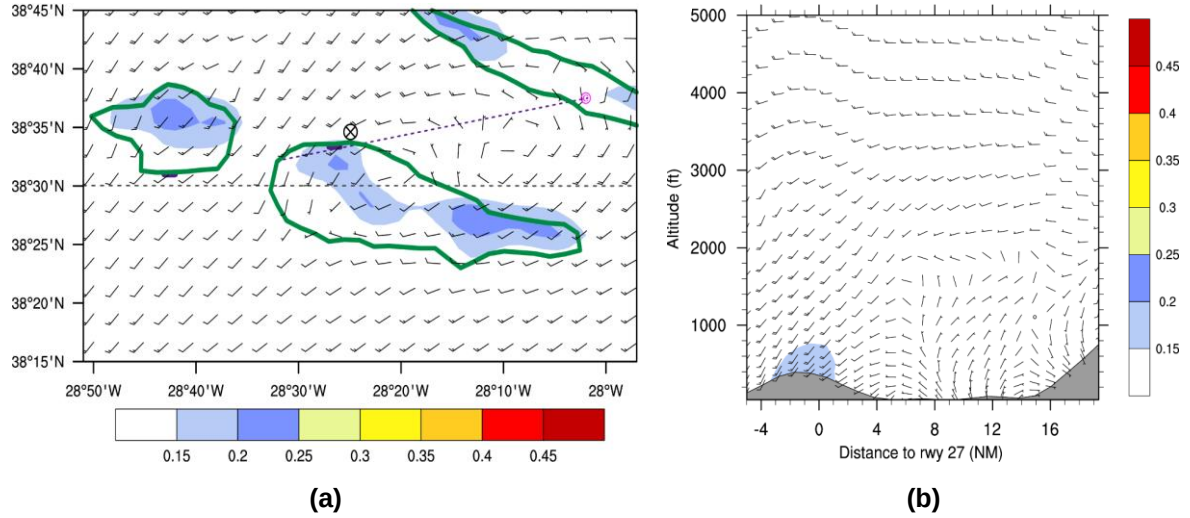

Figure 4.19: Horizontal representation of EDR during Flight 2. The circled "x" mark identifies aircraft position at 66 m. (b) Cross-sectional representation of EDR along flight path. EDR in units of $m^{2/3}s^{-1}$.

The comparison of the 1-km averaged and instantaneous F-factors with the turbulence indicators during Flight 1 and Flight 2 are shown in Figures 4.20 and 4.21, respectively. It reveals that the turbulence indexes, except CAT1, shows higher values near the surface, which decrease rapidly with height. This is more pronounced for Ellrod1, EDR and especially for the Brown index. At the lowest model level, the Brown index has a higher value during Flight 2 than in Flight 1, which is not realistic. However, the Brown index decreases more rapidly with height for Flight 2 than for Flight 1 (comparing Figures 4.20 (e) and 4.21 (e)). In general, the vertical wind shear presents higher values in the PBL near the surface [69], this fact appears to have a large influence on the Brown index. All AROME turbulence indicators predict higher values during Flight 1 than during Flight 2, consistently with higher values of $\bar{F}$ during Flight 1.

For Flight 1, $\bar{F}$ shows two maxima near 6 NM (near 1600 ft) and 7NM (near 1900 ft). None of the turbulence indicators accompanies the oscillatory nature of the F-factor. However, CAT1 and Ellrod 2 present high values between 1.5 and 6 NM, showing a predictive skill. CAT1 and Ellrod TI2 both decrease significantly near the 1-NM distance point to the runway, being unable to capture the maxima of F near the ground. At these levels, the use of EDR in combination with Ellrod 2 and CAT1 appears to be advantageous.

For Flight 2 (Figure 4.21), the CAT1 index (Figure 4.21 (a)) presents the most consistent evolution with $\bar{F}$ and F since it traces the extrema from the averaged and instantaneous F-factors, without invariably increasing with decreasing runway distance like the others.

Conclusions regarding preliminary thresholds for the three main turbulence indicators (most consistent behavior) are summarized in Table 4.4. The EDR threshold are valid only for levels below 500 ft.

Table 4.4: Suggested preliminary thresholds for three turbulence indicators.

Indicator	"Strong"	"Severe"
Ellrod TI2 $[10^{-6}s^{-2}]$	$[9,16[$	$[16,+\infty[$
CAT1 $[10^{-3}ms^{-2}]$	$[5,7[$	$[7,+\infty[$
EDR	$[0.3,0.35[$	$[0.35,+\infty[$

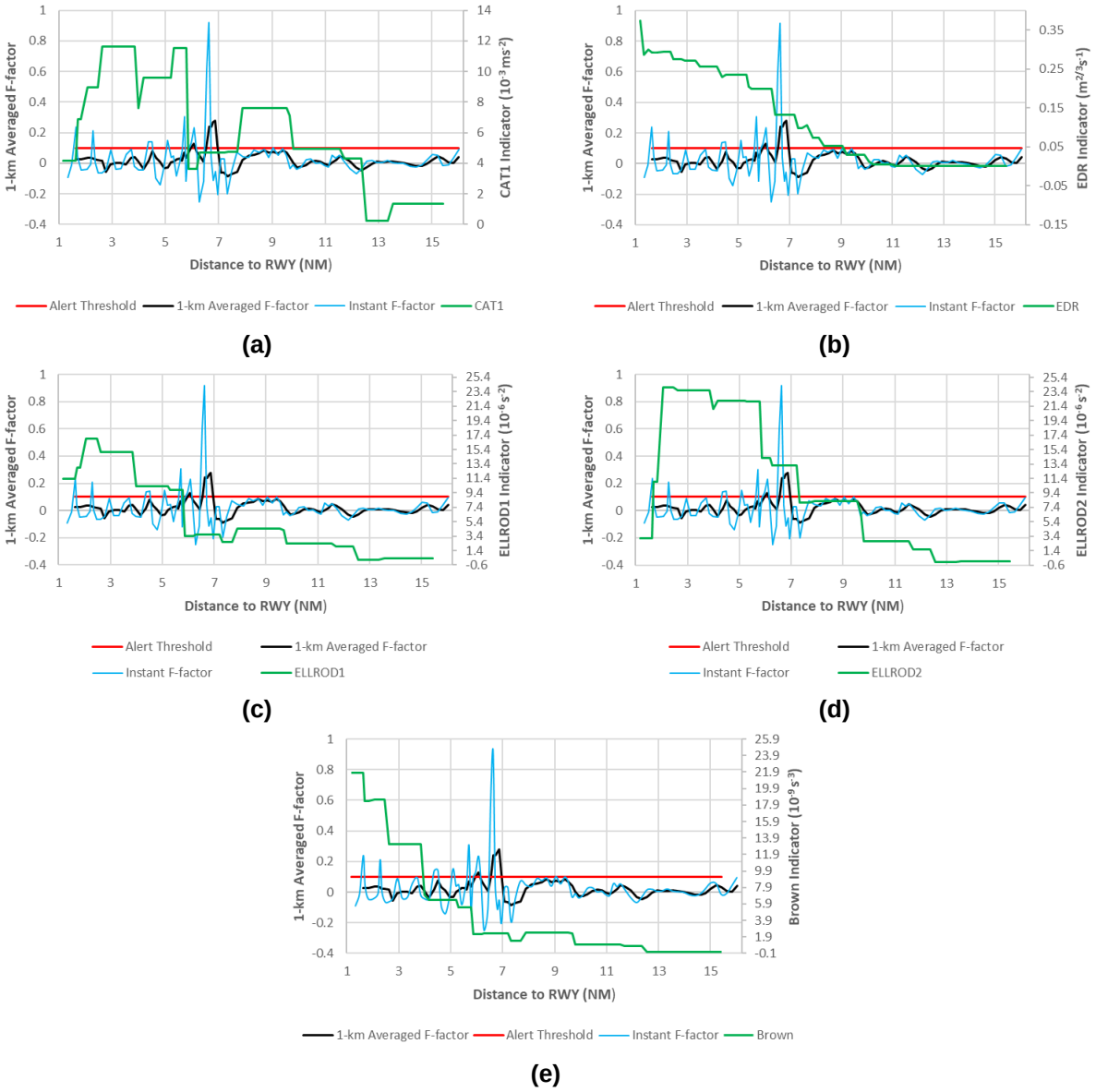

Figure 4.20: Comparison between (a) CAT1, (b) EDR, (c) Ellrod TI1, (d) Ellrod TI2 and (e) Brown indicators, instantaneous and 1-km averaged F-factors for Flight 1.

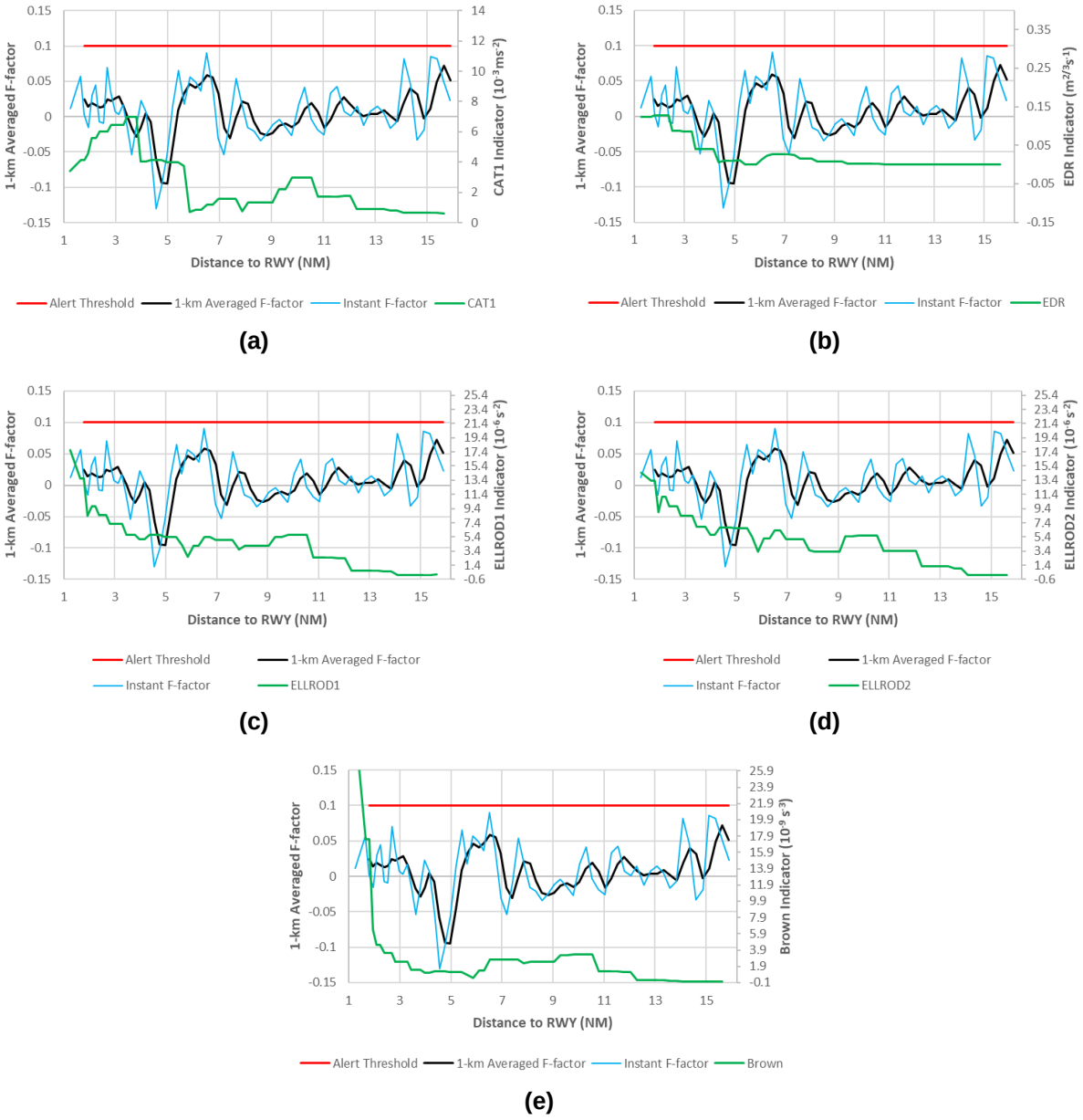

Figure 4.21: Comparison between (a) CAT1, (b) EDR, (c) Ellrod TI1, (d) Ellrod TI2 and (e) Brown indicators, instantaneous and 1-km averaged F-factors for Flight 2.

4.5 Objective Verification of Wind Forecasts from AROME

The accuracy of AROME wind predictions is assessed by comparing them with airborne data during Flights 1 and 2. Absolute errors of wind speed and direction are also mapped for each observation and forecast pair in Figure 4.22. The color coding for wind magnitude and its direction is based on ICAO guidelines [65] for operationally acceptable levels of forecast errors. For wind speed, an absolute value error of up to 5 kt (2.6 m/s) is deemed operationally desirable. For the direction, this value is 20°. For Flight 1, there is a good agreement between observations and forecasts. For altitudes above 1200 ft (366 m) in Flight 2, however, when the wind is weak (see Figures 4.5 (b) and 4.23 (b)), large errors (>120°) in wind direction are visible.

Values for the root mean square error (RMSE) and mean absolute error (MAE) regarding wind speed and direction (computed according to Eqs.3.27-3.31) are displayed in Table 4.5, showing that wind speed RMSE for Flight 1 is only slightly above operational recommendations (about 30% larger) and the RMSE for wind direction is 11.4°, well within the acceptable limits. The Flight 1 MAE for wind speed shows that the 2.6 ms^{-1} recommendation is exceeded by only 7% and the wind direction MAE is again within limits with a value of 8.1°. During Flight 2, however, which was characterized by weaker winds, the RMSE and MAE for wind speed are 4.4 ms^{-1} and 3.8 ms^{-1} respectively, slightly over 30% larger than Flight 1 errors. Moreover, during Flight 2 the RMSE and MAE for the wind direction are around 83.3° and 65.4°, thereby revealing a lack of skill for conditions of weak winds. These large errors in wind direction forecasts are consistent with the findings of Jiménez *et al*. [29], who assessed the WRF model error over complex terrain, demonstrating that $RMSE_{WDIR}$ increases with decreasing wind speeds, reaching values over 70° for wind speeds inferior to 2 kt (1 m/s).

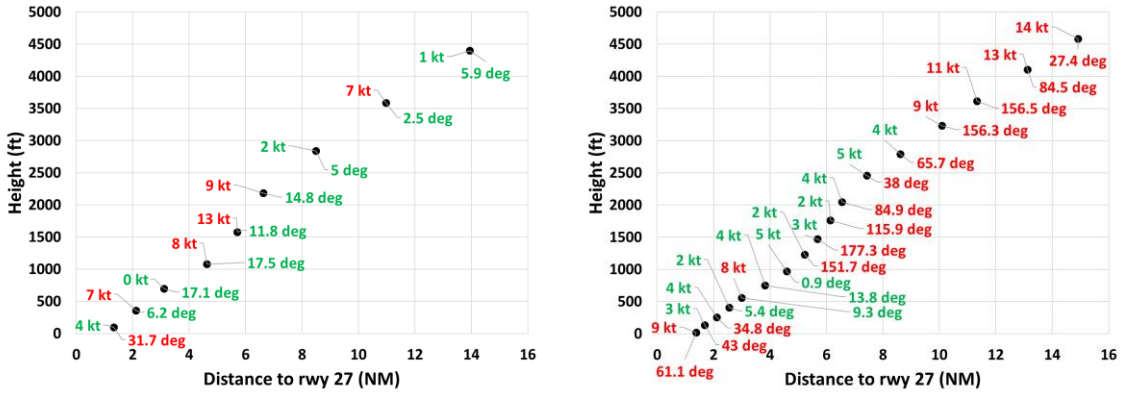

Figure 4.22: Absolute value differences for wind speed and direction for: (a) Flight 1 and (b) Flight 2.

Figures 4.23 superimpose AROME wind forecasts that are geographically the closest to the observation collected by the aircraft during Flights 1 and 2.

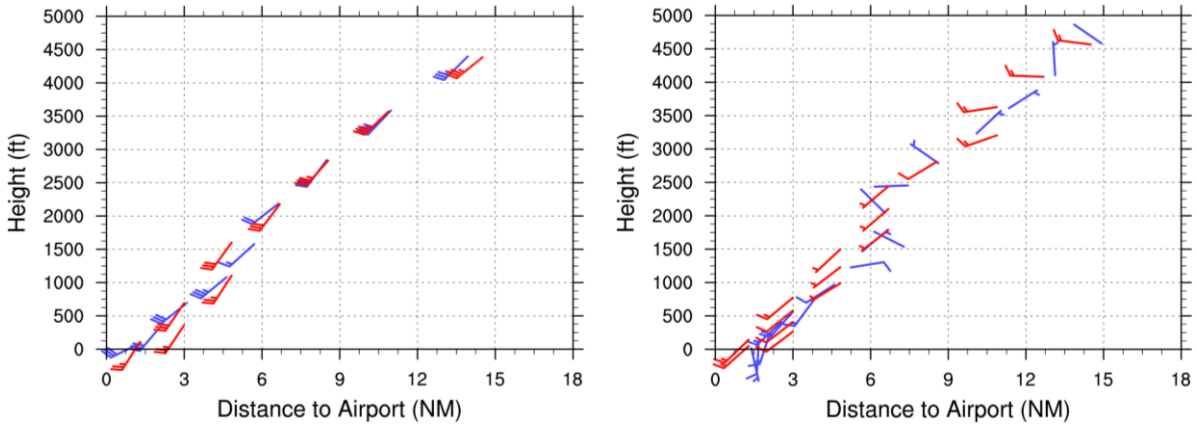

Figure 4.23: Wind profile along flight path (see Figure 3.4) according to aerial observations and AROME for: (a) Flight 1; (b) Flight 2. Wind barbs in blue depict aerial observations while those in red represent AROME forecasts.

Table 4.5: Summary of RMSE and MAE for wind speed and direction for both flights.

Flight	$RMSE_{WSPD}$ [ms^{-1}]	$RMSE_{WDIR}$ [deg]	MAE_{WSPD} [ms^{-1}]	MAE_{WDIR} [deg]
Flight 1	3.4	11.4	2.8	8.1
Flight 2	4.4	83.3	3.8	65.4

Chapter 5

Conclusions and Future Research

The present work focuses on the orographic flow associated with Pico Mountain in the Azores in two different synoptic environments, using SATA airborne measurements and forecasts from the operational AROME model. Aerial measurements were used to compute the wind shear intensity factor "*I*" according to Guan and Yong [17] and to categorize its severity according to four classes: "light", "moderate", "strong" and "severe".

During the first scenario, a hard landing incident (Flight 1) occurred in Pico Aerodrome. On this day, according to the AROME model, the upstream conditions were characterized by southwest winds with speeds of up to 40 kt (20 m/s) in the planetary boundary layer (PBL) and stable stratification, which translated to a Froude number slightly above 1 near the mountain top. These conditions triggered the development of vertically propagating mountain waves, which created an undulation pattern of upward and downward motion downstream of Pico Mountain, leading to maximum vertical velocities above 400 ft/min (2 ms^{-1}) and above 200 ft/min in the flight path. Based on ICAO Annex 3 guidelines [65], a mountain wave is deemed "severe" whenever downdrafts exceed 600 ft/min (3 m/s) and "moderate" whenever they vary between 350 to 600 ft/min (1.75 – 3.0 m/s). However, it is important to note that the AROME model may have underestimated the intensity of the vertical velocities, so this pattern of oscillating updraft/downdrafts may have strongly contributed to the hard landing event. Furthermore, in addition to mountain waves, large wind speeds (above 38 kt or 20 m/s) were registered close to 440 ft (107 m) and the wind shear intensity factor "*I*" based on airborne data showed that 36% of the approach phase (below 2100 ft or 640 m) occurred under "severe" wind shear conditions and 16% under "strong". At the Aerodrome, METAR observations showed southwest winds (18-21 kt or 9-11 m/s) with gusts between 28 and 31 kt (14 and 16 m/s).

During the second flight, the upstream conditions were characterized by southwest winds with speeds below 20 kt (10 m/s) in the PBL and a temperature inversion in the layer between 860 to 1100 m. In this range, the Froude number was less than 0.5. According to previous studies, these conditions promote upstream stagnation and flow splitting with the formation of lee vortices in low levels with reversed flow, which was predicted by the AROME model. During Flight 2, AROME forecasts also showed a pattern of vertically propagating waves, but with smaller vertical velocities and shorter vertical propagation, when compared to Flight 1. According to airborne observations, Flight 2 occurred under wind shear conditions predominantly rated as "light" (68%) or "moderate" (29%), with its most intense class being "strong" (only during less than 4% of the landing phase).

Moreover, the pattern of several turbulence indicators, which were computed from AROME forecasts, was analyzed for both flights. All of these indicators forecast higher values for Flight 1 than in

Flight 2, which agrees with the wind shear intensity factor "*I*" and both instantaneous and averaged F-factors derived from airborne observations. As a result of the comparison between "*I*" and the F-factors based on observations and AROME turbulence indicators, preliminary thresholds are proposed for three indexes. When compared to the instantaneous and 1-km averaged F-factors, the turbulence indicator that best accompanied its extreme oscillations was CAT1. In the future, more flights should be perused in order to verify the validity of such thresholds and to test the consistency of the CAT1 index. The use of other wind shear and turbulence indicators derived from airborne data should also be tested. Also, a linear combination of the three indexes (Ellrod TI2, CAT1 and EDR) may prove to be a good measure of turbulence and should therefore be subject to future scrutiny.

Lastly, this study provides an evaluation of the predictions of AROME wind data against aerial observations. For Flight 1, characterized by wind speeds over 30 kt (15 m/s) during several instants, AROME forecasts show a good agreement with observations in terms of wind speed and direction, with an RMSE of 3.4 ms^{-1} and 11.4°, respectively. The MAE score is 2.8 ms^{-1} and 8.1° for wind speed and direction, respectively. During Flight 2, in the approach phase, the maximum wind speed is 22 kt (11 m/s). In this case, AROME has an RMSE of 4.4 ms^{-1} and 83.3° for wind speed and wind direction respectively. MAE revealed values of 3.8 ms^{-1} and 65.4° for the wind speed and direction, respectively. In particular, when the wind speed is below 10 kt (5 m/s), large errors (>120°) in the wind direction can be found. Such is a limitation of NWP models that was previously documented by Jiménez *et al*. [29] for the WRF model.

Strong ageostrophic winds often develop in coastal gaps or channels when an along-gap pressure gradient is created [70]. Possibly, a gap flow, may also contribute to reinforce the winds downstream of the strait between Faial and Pico islands. This hypothesis should be subject of future research.

References

1. Markowski, P.; Richardson, Y. “Mesoscale Gravity Waves”. In *Mesoscale Meteorology in Midlatitudes,* 1st ed.; Wiley-Blackwell, **2010**; pp.161-180.
2. WMO, Technical Note 34: The Airflow over Mountains, No.98, World Meteorological Organization, **1960**, pp.1-135.
3. Sutherland, B.R. Internal Gravity Waves. Cambridge Univ. Press, **2018**, pp. 1-377.
4. Lyra, G. Theory of Stationary Lee Waves in Free Atmosphere. Z. Angew. Math. Mech. Berlin 23, **1943**, pp.1-28. (In German)
5. Queney, P. Theory of Perturbations in Stratified Currents with Application to Airflow over Mountain Barriers. Dept. of Meteor., Univ. of Chicago Press, **1947**, No.23.
6. Scorer, R.S. Theory of Waves in the Lee of Mountains. *Quart. J. R. Met. Soc.* **1949**, Vol. 75, pp.41-56.
7. Sawyer, J.S.; Hinds, M.K. Numerical Calculations of the Airflow over a Ridge for Small Amplitudes. M.R.P. 1041. Air Ministry Meteorological Research Committee, **1957**.
8. Long, R.R. Some Aspects of the Flow of Stratified Fluids. I. A Theoretical Investigation. *Tellus* **1953**, Vol. 5, pp.42-58.
9. Lin, Y.-L. Mesoscale Dynamics. Cambridge University Press **2007**, pp.1-630.
10. Bérenger, M. and Gerbier, N. Undulatory motion at St.-Auban-sur-Durance, first campaign of studies and measurements, **1956**, Monograph Nº4 from the National Meteorology. (In French)
11. Met Office: Lenticular Clouds. Available online: www.metoffice.gov.uk/learning/clouds/other-clouds/lenticular (accessed on 12/21/2018).
12. Weather Online: Rotor Cloud. Available online: https://www.weatheronline.co.uk/reports/wxfacts/Rotor-cloud.htm (accessed on 12/21/2018).
13. NASA Earth Observatory: Two Views of Von Kármán Vortices. Available online: https://earthobservatory.nasa.gov/images/90734/two-views-of-von-karman-vortices (accessed on 12/21/2018).
14. Durran, D.R. Lee Waves and Mountain Waves. In *Encyclopedia of the Atmospheric Sciences*, Holton, J.R.; J. Pyle and J.A. Curry, Eds. Elsevier Science Ltd., **2003**, pp. 1161-1169.
15. Ágústsson, H.; Ólafsson, H. Simulations of Observed Lee Waves and Rotor Turbulence. *Monthly Weather Review* **2013**, Vol. 142, pp.832-849.
16. Arkell, R.E. Differentiating between Types of Wind Shear in Aviation Forecasting. *National Weather Digest*, **2000**, Vol. 24, pp.39-51.
17. Guan, W.-L.; Yong, K. Review of Aviation Accidents Caused by Wind Shear and Identification Methods. *Journal of the Chinese Society of Mechanical Engineers* **2002**, Volume 23, pp. 99-110.
18. Durran, D.R. Mountain Waves and Downslope Winds. *Atmospheric Processes over Complex Terrain, Meteorological Monographs, Amer. Meteor. Soc.*, **1990**, Vol. 23, pp.59-81.

19. Keller, T.L.; Trier, S.B.; Hall, W.D.; Sharman, R.D., Xu, M.; Liu, Y. Lee Waves Associated with a Commercial Jetliner Accident at Denver International Airport. *Journal of Applied Meteorology and Climatology* **2015**, Volume 54, pp. 1373 -1392.
20. Parker, T.J.; Lane, T.P. Trapped Mountain Waves during a Light Aircraft Accident. *Australian Meteorological and Oceanographic Journal* **2013,** Volume 63, pp. 377-389.
21. Grubišić, V.; Sachsperger, J.; Caldeira, R.M. Atmospheric Wake of Madeira: First Aerial Observations and Numerical Simulations. *J. Atmos. Sci.* **2015,** Volume 72, pp.4755-4776.
22. Caldeira, R.M.A.; Tomé, R. Wake Response to an Ocean-Feedback Mechanism: Madeira Island Case Study. *Boundary-Layer Meteorology* **2013**, Volume 148, pp. 419-436.
23. Couvelard, X.; Caldeira, R.M.A.; Araújo, I.B.; Tomé, R. Wind Meditated Vorticity-generation and Eddy-confinement, Leeward of the Madeira Island: 2008 Numerical Case Study. *Dynamics of Atmospheres and Oceans* **2012,** Volume 58, pp. 128-149.
24. Barata, J.M.M.; Medeiros, R.C.; Silva, A.R.R. An Experimental Study of Terrain-Induced Airflow at the LPPI Airport. *American Institute of Aeronautics and Astronautics* **2010**, pp. 1-8.
25. Elvidge, A.D. and Renfrew, I.A. The Causes of Foehn Warming in the Lee of Mountains. *Bull. Amer. Meteor. Soc.* **2016**, Vol. 97, pp.455-466.
26. Sayers, D.; Stewart, M. "Background Information". In *Azores,* 6th ed.; The Globe Pequot Press Inc, USA, **2016**, pp. 2-3.
27. Woodfield, A.A.; Woods, J.F. Worldwide experience of windshear during 1981-82; *AGARD Flight Mechanics Panel Conf. on Flight mechanics and System Design Lessons from Operational Experience*, AGARD CP **1983**, 347, 28 pp.
28. Maruhashi, J.; Serrão, P.; Belo-Pereira, M. Analysis of Mountain Wave Effects on a Hard Landing Incident in Pico Aerodrome Using the AROME Model and Airborne Observations. *Atmosphere* **2019**, 10, 350.
29. Jiménez, P.A.; Dudhia, J. On the Ability of the WRF Model to Reproduce the Surface Wind Direction over Complex Terrain. *Journal of Applied Meteorology and Climatology* **2013**, Vol. 52, pp. 1610-1617.
30. Medeiros, R.F.C. Airflow around Pico Island and the Operationality of its Airport. Master´s Thesis, Universidade da Beira Interior, Covilhã, June **2009**. (In Portuguese)
31. Brugge, R. Back to basics: Atmospheric stability: Part 1 – basic concepts. *Weather* 1996, Vol. 51, pp.134-140.
32. Doswell III, C.A.; Markowski, P.M. Is Buoyancy a Relative Quantity? *Mon. Wea. Rev.* **2004**, Volume 132, pp.853-863.
33. Sheridan, P.F.; Vosper, S.B. A Flow Regime Diagram for Forecasting Lee Waves, Rotors and Downslope Winds. *Meteorol. Appl.* **2006**, Volume 13, pp. 179-195.
34. Sheppard, P.A. Airflow over Mountains. *Quart. J. Roy. Meteor. Soc.* **1956**, Volume 82, pp. 528-529.
35. Lynch, A.H.; Cassano, J.J. Mountain Weather. In *Atmospheric Dynamics*; Wiley, **2006**, pp. 209-232.
36. Heinze, R.; Raasch, S.; Etling, D. The Structure of Kármán Vortex Streets in the Atmospheric Boundary Layer derived from Large Eddy Simulation. *Meteorol. Z.* **2012**, Volume 21, pp. 221-237.

37. Sha, W.; Nakabayashi, K.; Ueda, H. Numerical Study on Flow Pass of a Three-dimensional Obstacle under a Strong Stratification Condition. *J. Appl. Meteorol.* **1998**, Volume 37, pp. 1047-1054.
38. Smolarkiewicz, P.K.; Rotunno, R. Low Froude-Number Flow Past Three-dimensional Obstacles. Part I: Baroclinically Generated Lee Vortices. *J. Atmos. Sci.* **1989**, Volume 46, pp. 1154-1164.
39. Vosper, S.B.; Gardner, B.A. Measurements of the Near Surface Flow over a Hill. *Quart. J. Roy. Meteor. Soc.* **2002**, Volume 128, pp. 2257-2280.
40. Epifanio, C.C. Lee Vortices. *Encyclopedia of the Atmospheric Sciences*, Cambridge University Press, **2014**; pp. 1150-1160.
41. Bauer, M.H.; Mayr, G.J.; Vergeiner, I.; Pichler, H. Strongly Nonlinear Flow over and around a Three-Dimensional Mountain as a Function of the Horizontal Aspect Ratio. *J. Atmos. Sci.* **2000**, Volume 57, pp. 3971-3991.
42. Jiang, Q.; Doyle, J.D.; Smith, R.B. Blocking, Descent and Gravity Waves: Observations and Modelling of a MAP Northerly Föhn Event. *Q. J. R. Meteorol. Soc.* **2005**, Volume 131, pp. 675-701.
43. Trombetti, F.; Tampieri, F. An Application of the Dividing-Streamline Concept to the Stable Airflow over Mesoscale Mountains. *Mon. Weather Rev.* **1987**, Volume 115, pp. 1802-1806.
44. Wooldridge, G. L.; Fox, D. G.; Furman, R. W. Air-Flow Patterns over and around a Large 3-Dimensional Hill. *Meteorol. Atmos. Phys.* **1987**, Volume 37, pp. 259-270.
45. Vosper, S.B. Inversion Effects on Mountain Lee Waves. *Q. J. Roy. Meteorol. Soc.* **2004**, Volume 130, pp. 1723-1748.
46. Sheridan, P.F.; Vosper, S.B. A Flow Regime Diagram for Forecasting Lee Waves, Rotors and Downslope Winds. *Meteorol. Appl.* **2006**, Volume 13, pp. 179-195.
47. Schär, C.; Smith, R.B. Shallow-Water Flow past Isolated Topography. Part I: Vorticity Production and Wake Formation. *J. Atmos. Sci.* **1993**, Volume 50, pp. 1373-1400.
48. Lott, F.; Miller, M.J. A new subgrid-scale orographic drag parametrization: Its formulation and testing. *Q.J.R. Meteorol. Soc.* **1997**, Volume 123, pp.101-127.
49. Wurtele, M.; Datta, A.; Sharman, R.D. Lee Waves: Benign and Malignant. *NASA Contractor Report 186024* **1993**, pp. 1-28.
50. Eliassen, A.; Palm, E. On the Transfer of Energy in Stationary Mountain Waves. *Geofys. Publ.* **1960**, Volume 22, pp. 1-23.
51. Queney, P. The Problem of Airflow over Mountains: A Summary of Theoretical Studies. *Bull. Amer. Meteor. Soc.* **1948**, Volume 29, pp. 16-26.
52. Smith, R.B. Mountain-induced Stagnation Points in Hydrostatic Flow. *Tellus* **1989**, Volume 41A, pp. 270-274.
53. Batchelor, G.K. An Introduction to Fluid Dynamics. Cambridge University Press **1967**.
54. Hunt, J.C.R.; Snyder, W.H. Experiments on Stably and Neutrally Stratified Flow over a Model Three-dimensional Hill. *J. Fluid Mech.* **1980**, Vol. 96, pp.671-704.

55. Seity, Y.; Brousseau, P.; Malardel, S.; Hello, G.; Bénard, P.; Bouttier, F.; Lac, C.; Masson, V. The AROME-France Convective-Scale Operational Model. *Mon. Weather Rev.* **2011**, Volume 139, pp. 976-991.
56. Cuxart, J.; Bougeault, P.; Redelsperger, J.-L.; A Turbulence Scheme Allowing for Mesoscale and Large-eddy Simulations. *Q.J.R. Meteorol. Soc.* **2006,** Volume 126, pp. 1-30.
57. ICAO, Manual on Low-level Wind Shear, 1st ed., International Civil Aviation Organization, **2005**, pp.1-213.
58. Proctor, F.H.; Hinton, D.A.; Bowles, R.L. A Wind Shear Hazard Index. *9th Conference on Aviation, Range and Aerospace Meteorology* **2000**, Orlando, FL., USA.
59. Bowles, R.L.; Hinton, D.A. Wind Shear Detection: Airborne System Perspective. Royal Aeronautical Society **1990**, pp. 2013-2016.
60. Lewis, M.S.; Robinson, P.A.; Hinton, D.A.; Bowles, R.L. The Relationship of an Integral Wind Shear Hazard to Aircraft Performance Limitations. *NASA TM-109080*, **1994.**
61. Mulgund, S.S.; Stengel, R.F. Optimal Nonlinear Estimation for Aircraft Flight Control in Wind Shear. *Automatica* **1996**, Vol. 32, No.1, pp.3-13.
62. Gill, P.G.; Buchanan, P. An Ensemble based Turbulence Forecasting System. *Meteorol. Appl.* **2014**, Volume 21, pp. 12-19.
63. Sharman, R.; Tebaldi, C.; Wiener, G.; Wolff, J. An Integrated Approach to Mid- and Upper-Level Turbulence Forecasting. *Weather and Forecasting* **2006**, Volume 21, pp. 268-287.
64. Frech, M.; Holzäpfel, F.; Tafferner, A.; Gerz, T. High-Resolution Weather Database for the Terminal Area of Frankfurt Airport. *American Meteorological Society* **2007**, Volume 46, pp. 1913-1932.
65. ICAO, Meteorological Service for International Air Navigation: Annex 3 to the Convention on International Civil Aviation, 20th ed., International Civil Aviation Organization, International Standards and Recommended Practices Tech. Rep., **2007**, pp. 218.
66. Smith, R.B.; Grubišić, V. Aerial Observations of Hawaii's Wake. *J. Atmos. Sci.* **1993**, Volume 50, pp. 3728-3750.
67. ICAO, Meeting of the Meteorology Panel (METP): Proposed Revision to Eddy Dissipation Rate (EDR) Values in Annex 3, International Civil Aviation Organization, **2018**, pp. 1-6.
68. Sharman, R.D.; Cornman, L.B.; Meymaris, G.; Pearson, J; Farrar, T. Descriptions and Derived Climatologies of Automated In Situ Eddy-Dissipation-Rate Reports of Atmospheric Turbulence. *Journal of Applied Meteorology and Climatology* **2014**, Volume 53, pp. 1416-1432.
69. Stull, R.B. *An Introduction to Boundary Layer Meteorology*. Springer: Berlin, Germany. 1988; pp. 666.
70. Colle, B.A.; Mass, C.F. High-Resolution Observations and Numerical Simulations of Easterly Gap Flow through the Strait of Juan de Fuca on 9-10 December 1995. *Mon. Wea. Rev.* **2000**, Volume 128, pp. 2398-2422.
71. SATA Airbus A320. Available online: https://www.sata.pt/en/fleet/a320 (accessed on 12/21/2018).

72. Modern Airliners. Available online: http://www.modernairliners.com/boeing-747-jumbo/boeing-747-specs/ (accessed on 12/21/2018).

Appendix

A.1 Linearization of Navier-Stokes, Continuity and Thermodynamic Equations

The 2D flow ($\frac{\partial}{\partial y} = 0$) equations to be linearized are from Section 2.3.2 and are shown again here:

$$\frac{\partial u}{\partial t} + u\frac{\partial u}{\partial x} + w\frac{\partial u}{\partial z} + \frac{1}{\rho}\frac{\partial p}{\partial x} = 0 \tag{2.23}$$

$$\frac{\partial w}{\partial t} + u\frac{\partial w}{\partial x} + w\frac{\partial w}{\partial z} + \frac{1}{\rho}\frac{\partial p}{\partial z} + g = 0. \tag{2.24}$$

$$\frac{\partial u}{\partial x} + \frac{\partial w}{\partial z} = 0. \tag{2.25}$$

$$\frac{D\theta}{Dt} = 0 \Longrightarrow \frac{\partial \theta}{\partial t} + u\frac{\partial \theta}{\partial x} + w\frac{\partial \theta}{\partial z} = 0. \tag{2.26}$$

The variables decomposed into their basic state and disturbance terms were previously defined as:

$$u = \bar{u} + u', with\ \bar{u}\ constant \tag{2.27a}$$

$$w = w' \tag{2.27b}$$

$$p = \bar{p}(z) + p' \tag{2.27c}$$

$$\theta = \bar{\theta}(z) + \theta' \tag{2.27d}$$

$$\rho = \bar{\rho} + \rho'. \tag{2.27e}$$

Starting with Eq. 2.23, equations 2.27a – 2.27c and 2.27e will be replaced in order to yield the following:

$$\frac{\partial \bar{u}}{\partial t} + \frac{\partial u'}{\partial t} + \bar{u}\frac{\partial \bar{u}}{\partial x} + u'\frac{\partial \bar{u}}{\partial x} + \bar{u}\frac{\partial u'}{\partial x} + u'\frac{\partial u'}{\partial x} + w'\frac{\partial u'}{\partial z} + w'\frac{\partial \bar{u}}{\partial z} + \frac{1}{\bar{\rho} + \rho'}\left(\frac{\partial \bar{p}}{\partial x} + \frac{\partial p'}{\partial x}\right) = 0. \tag{A1}$$

Cancelling nonlinear terms like $u'\frac{\partial u'}{\partial x}$ and removing null derivatives of constant states leads to:

$$\frac{\partial u'}{\partial t} + \bar{u}\frac{\partial u'}{\partial x} + \frac{1}{\bar{\rho} + \rho'}\frac{\partial p'}{\partial x} = 0. \tag{A2}$$

Using the approximation that $\frac{1}{\rho' + \bar{\rho}} = \frac{1}{\bar{\rho}\left(1 + \frac{\rho'}{\bar{\rho}}\right)} \approx \frac{1}{\bar{\rho}}$ simplifies further to the same result as equation 2.28 [35]:

$$\frac{\partial u'}{\partial t} + \bar{u}\frac{\partial u'}{\partial x} + \frac{1}{\bar{\rho}}\frac{\partial p'}{\partial x} = 0. \tag{2.28}$$

Following the same procedure, (2.24) becomes:

$$\frac{\partial \overline{w}}{\partial t} + \frac{\partial w'}{\partial t} + u'\frac{\partial w'}{\partial x} + \bar{u}\frac{\partial w'}{\partial x} + w'\frac{\partial w'}{\partial z} + \frac{1}{\bar{\rho} + \rho'}\left(\frac{\partial \bar{p}}{\partial z} + \frac{\partial p'}{\partial z}\right) + g = 0. \quad (A3)$$

Again eliminating nonlinear terms and null derivatives simplifies to:

$$\frac{\partial w'}{\partial t} + \bar{u}\frac{\partial w'}{\partial x} + \frac{1}{\bar{\rho} + \rho'}\left(\frac{\partial \bar{p}}{\partial z} + \frac{\partial p'}{\partial z}\right) + g = 0. \quad (A4)$$

Expanding equation A4 and applying the hydrostatic relation ($\frac{\partial \bar{p}}{\partial z} = -\bar{\rho}g$) produces:

$$\frac{\partial w'}{\partial t} + \bar{u}\frac{\partial w'}{\partial x} + \frac{1}{\bar{\rho} + \rho'}\left(-\bar{\rho}g + \frac{\partial p'}{\partial z}\right) + g = 0$$

$$\frac{\partial w'}{\partial t} + \bar{u}\frac{\partial w'}{\partial x} + g - \frac{\bar{\rho}g}{\bar{\rho} + \rho'} + \frac{1}{\bar{\rho} + \rho'}\frac{\partial p'}{\partial z} = 0$$

$$\frac{\partial w'}{\partial t} + \bar{u}\frac{\partial w'}{\partial x} + g\frac{\rho'}{\bar{\rho} + \rho'} + \frac{1}{\bar{\rho} + \rho'}\frac{\partial p'}{\partial z} = 0. \quad (A5)$$

As is done in Lynch and Cassano [35], the approximations $\frac{1}{\rho' + \bar{\rho}} \approx \frac{1}{\bar{\rho}}$ and $-\frac{\rho'}{\bar{\rho}} \approx \frac{\theta'}{\bar{\theta}}$ are used in (A5) to arrive at Equation 2.29:

$$\frac{\partial w'}{\partial t} + \bar{u}\frac{\partial w'}{\partial x} - g\frac{\theta'}{\bar{\theta}} + \frac{1}{\bar{\rho}}\frac{\partial p'}{\partial z} = 0. \quad (2.29)$$

For the continuity equation in (2.25), the substitution of linearizing expressions leads to:

$$\frac{\partial \bar{u}}{\partial x} + \frac{\partial u'}{\partial x} + \frac{\partial w'}{\partial z} = 0. \quad (A6)$$

Since $\frac{\partial \bar{u}}{\partial x} = 0$, (A6) is written as:

$$\frac{\partial u'}{\partial x} + \frac{\partial w'}{\partial z} = 0. \quad (2.30)$$

Finally, the linearized thermodynamic equation becomes:

$$\frac{\partial \bar{\theta}}{\partial t} + \frac{\partial \theta'}{\partial t} + \bar{u}\frac{\partial \bar{\theta}}{\partial x} + u'\frac{\partial \bar{\theta}}{\partial x} + \bar{u}\frac{\partial \theta'}{\partial x} + u'\frac{\partial \theta'}{\partial x} + w'\frac{\partial \bar{\theta}}{\partial z} + w'\frac{\partial \theta'}{\partial z} = 0. \quad (A7)$$

Removing null derivatives yields:

$$\frac{\partial \theta'}{\partial t} + \bar{u}\frac{\partial \theta'}{\partial x} + w'\frac{\partial \bar{\theta}}{\partial z} = 0. \quad (2.31)$$

The approximation $-\frac{\rho'}{\bar{\rho}} \approx \frac{\theta'}{\bar{\theta}}$ used above is obtained from the ideal gas law (Eq. 2.1) and inserting for the basic state and perturbation notations of pressure, density and virtual temperature:

$$\bar{p} + p' = (\bar{\rho} + \rho')(\overline{T}_v + T_v')R \quad (A8)$$

$$\bar{p} + p' = [\bar{\rho}\overline{T}_v + \bar{\rho}T_v' + \rho'\overline{T}_v + \rho'T_v']R \quad (A9)$$

Neglecting the product of perturbation terms in Eq. A9 and using the approximation that $\bar{p} \approx \bar{\rho}R\overline{T}_v$ yields:

$$p' \approx R\bar{\rho}T_v' + R\rho'\overline{T}_v, \quad (A10)$$

$$p' \approx \bar{\rho} R \left[T_v' + \frac{\rho'}{\bar{\rho}} \bar{T}_v \right]. \tag{A11}$$

Employing the approximation $\bar{p} \approx \bar{\rho} R \bar{T}_v$ once again:

$$p' \approx \frac{\bar{p}}{\bar{T}_v} \left[T_v' + \frac{\rho'}{\bar{\rho}} \bar{T}_v \right]. \tag{A12}$$

$$\frac{p'}{\bar{p}} \approx \frac{T_v'}{\bar{T}_v} + \frac{\rho'}{\bar{\rho}}. \tag{A13}$$

The contribution of pressure disturbances on the density is generally dismissed, as is explained in [32]:

$$\frac{\rho'}{\bar{\rho}} \approx -\frac{T_v'}{\bar{T}_v}. \tag{A14}$$

A.2 Derivation of the Linear Mountain Wave Equation

The linearized Navier-Stokes, continuity and thermodynamic equations below (2.28 – 2.31) will be mathematically combined, following a similar process described by Lynch and Cassano [35], in order to obtain a single differential equation emphasizing only the disturbance of the vertical wind component w'.

$$\frac{\partial u'}{\partial t} + \bar{u}\frac{\partial u'}{\partial x} + \frac{1}{\bar{\rho}}\frac{\partial p'}{\partial x} = 0 \tag{2.28}$$

$$\frac{\partial w'}{\partial t} + \bar{u}\frac{\partial w'}{\partial x} - g\frac{\theta'}{\bar{\theta}} + \frac{1}{\bar{\rho}}\frac{\partial p'}{\partial z} = 0 \tag{2.29}$$

$$\frac{\partial u'}{\partial x} + \frac{\partial w'}{\partial z} = 0 \tag{2.30}$$

$$\frac{\partial \theta'}{\partial t} + \bar{u}\frac{\partial \theta'}{\partial x} + w'\frac{\partial \bar{\theta}}{\partial z} = 0. \tag{2.31}$$

Step 1: $\frac{\partial}{\partial z}[Eq.2.28]$.

$$\frac{\partial^2 u'}{\partial z \partial t} + \underbrace{\frac{\partial \bar{u}}{\partial z}}_{=0}\frac{\partial u'}{\partial x} + \bar{u}\frac{\partial^2 u'}{\partial x \partial z} + \frac{1}{\bar{\rho}}\frac{\partial^2 p'}{\partial x \partial z} = 0$$

$$\frac{\partial^2 u'}{\partial z \partial t} + \bar{u}\frac{\partial^2 u'}{\partial x \partial z} + \frac{1}{\bar{\rho}}\frac{\partial^2 p'}{\partial x \partial z} = 0 \tag{B1}$$

Step 2: $\frac{\partial}{\partial x}[Eq.2.29]$.

$$\frac{\partial^2 w'}{\partial x \partial t} + \underbrace{\frac{\partial \bar{u}}{\partial x}\frac{\partial w'}{\partial x}}_{=0} + \bar{u}\frac{\partial^2 w'}{\partial x^2} - \frac{g}{\bar{\theta}}\frac{\partial \theta'}{\partial x} + \frac{1}{\bar{\rho}}\frac{\partial^2 p'}{\partial x \partial z} = 0$$

$$\frac{\partial^2 w'}{\partial x \partial t} + \bar{u}\frac{\partial^2 w'}{\partial x^2} - \frac{g}{\bar{\theta}}\frac{\partial \theta'}{\partial x} + \frac{1}{\bar{\rho}}\frac{\partial^2 p'}{\partial x \partial z} = 0 \tag{B2}$$

Step 3: Eq.B2 – Eq.B1.

$$\frac{\partial^2 w'}{\partial x \partial t} + \bar{u}\frac{\partial^2 w'}{\partial x^2} - \frac{g}{\bar{\theta}}\frac{\partial \theta'}{\partial x} + \frac{1}{\bar{\rho}}\frac{\partial^2 p'}{\partial x \partial z} - \frac{\partial^2 u'}{\partial z \partial t} - \bar{u}\frac{\partial^2 u'}{\partial x \partial z} - \frac{1}{\bar{\rho}}\frac{\partial^2 p'}{\partial x \partial z} = 0$$

$$\frac{\partial^2 w'}{\partial x \partial t} - \frac{\partial^2 u'}{\partial z \partial t} + \bar{u}\frac{\partial^2 w'}{\partial x^2} - \bar{u}\frac{\partial^2 u'}{\partial x \partial z} - \frac{g}{\bar{\theta}}\frac{\partial \theta'}{\partial x} = 0 \tag{B3}$$

Step 4: Factor the operator $\left(\frac{\partial}{\partial t} + \bar{u}\frac{\partial}{\partial x}\right)$ from Eq.B3.

$$\left(\frac{\partial}{\partial t} + \bar{u}\frac{\partial}{\partial x}\right)\left(\frac{\partial w'}{\partial x} - \frac{\partial u'}{\partial z}\right) - \frac{g}{\bar{\theta}}\frac{\partial \theta'}{\partial x} = 0 \tag{B4}$$

Step 5: $\frac{\partial}{\partial x}[Eq.B4]$.

$$\frac{\partial}{\partial x}\left[\left(\frac{\partial}{\partial t}+\bar{u}\frac{\partial}{\partial x}\right)\left(\frac{\partial w'}{\partial x}-\frac{\partial u'}{\partial z}\right)-\frac{g}{\bar{\theta}}\frac{\partial \theta'}{\partial x}\right]=0$$

$$\left(\frac{\partial}{\partial t}+\bar{u}\frac{\partial}{\partial x}\right)\left(\frac{\partial^2 w'}{\partial x^2}-\frac{\partial^2 u'}{\partial x \partial z}\right)-\frac{g}{\bar{\theta}}\frac{\partial^2 \theta'}{\partial x^2}=0 \qquad (B5)$$

Step 6: $\frac{\partial}{\partial z}[Eq.2.30]$.

$$\frac{\partial}{\partial z}\left[\frac{\partial u'}{\partial x}+\frac{\partial w'}{\partial z}\right]=0 \Longrightarrow \frac{\partial^2 u'}{\partial x \partial z}+\frac{\partial^2 w'}{\partial z^2}=0$$

$$\frac{\partial^2 w'}{\partial z^2}=-\frac{\partial^2 u'}{\partial x \partial z} \qquad (B6)$$

Step 7: Substitute Eq.B6 into Eq.B5:

$$\left(\frac{\partial}{\partial t}+\bar{u}\frac{\partial}{\partial x}\right)\left(\frac{\partial^2 w'}{\partial x^2}+\frac{\partial^2 w'}{\partial z^2}\right)-\frac{g}{\bar{\theta}}\frac{\partial^2 \theta'}{\partial x^2}=0 \qquad (B7)$$

Step 8: $\frac{\partial^2}{\partial x^2}[Eq.2.31]$.

$$\frac{\partial^3 \theta'}{\partial x^2 \partial t}+\bar{u}\frac{\partial^3 \theta'}{\partial x^3}+\underbrace{\frac{\partial^2 \bar{u}}{\partial x^2}\frac{\partial \theta'}{\partial x}}_{=0}+\frac{\partial^2 w'}{\partial x^2}\frac{\partial \bar{\theta}}{\partial z}+w'\underbrace{\frac{\partial^2}{\partial x^2}\left(\frac{\partial \bar{\theta}}{\partial z}\right)}_{=0}=0$$

$$\frac{\partial^3 \theta'}{\partial x^2 \partial t}+\bar{u}\frac{\partial^3 \theta'}{\partial x^3}+\frac{\partial^2 w'}{\partial x^2}\frac{\partial \bar{\theta}}{\partial z}=0$$

$$\left(\frac{\partial}{\partial t}+\bar{u}\frac{\partial}{\partial x}\right)\frac{\partial^2 \theta'}{\partial x^2}+\frac{\partial^2 w'}{\partial x^2}\frac{\partial \bar{\theta}}{\partial z}=0 \qquad (B8)$$

Step 9: Apply $\left(\frac{\partial}{\partial t}+\bar{u}\frac{\partial}{\partial x}\right)[Eq.B7]$.

$$\left(\frac{\partial}{\partial t}+\bar{u}\frac{\partial}{\partial x}\right)\left(\frac{\partial}{\partial t}+\bar{u}\frac{\partial}{\partial x}\right)\left(\frac{\partial^2 w'}{\partial x^2}+\frac{\partial^2 w'}{\partial z^2}\right)-\frac{g}{\bar{\theta}}\left(\frac{\partial}{\partial t}+\bar{u}\frac{\partial}{\partial x}\right)\frac{\partial^2 \theta'}{\partial x^2}=0$$

$$\left(\frac{\partial}{\partial t}+\bar{u}\frac{\partial}{\partial x}\right)^2\left(\frac{\partial^2 w'}{\partial x^2}+\frac{\partial^2 w'}{\partial z^2}\right)-\frac{g}{\bar{\theta}}\left(\frac{\partial}{\partial t}+\bar{u}\frac{\partial}{\partial x}\right)\frac{\partial^2 \theta'}{\partial x^2}=0 \qquad (B9)$$

Step 10: Substitute Eq.B8 into Eq.B9.

$$\left(\frac{\partial}{\partial t}+\bar{u}\frac{\partial}{\partial x}\right)^2\left(\frac{\partial^2 w'}{\partial x^2}+\frac{\partial^2 w'}{\partial z^2}\right)-\frac{g}{\bar{\theta}}\left(-\frac{\partial \bar{\theta}}{\partial z}\frac{\partial^2 w'}{\partial x^2}\right)=0$$

$$\left(\frac{\partial}{\partial t}+\bar{u}\frac{\partial}{\partial x}\right)^2\left(\frac{\partial^2 w'}{\partial x^2}+\frac{\partial^2 w'}{\partial z^2}\right)+\underbrace{\frac{g}{\bar{\theta}}\frac{\partial\bar{\theta}}{\partial z}}_{=N^2}\frac{\partial^2 w'}{\partial x^2}=0$$

$$\left(\frac{\partial}{\partial t}+\bar{u}\frac{\partial}{\partial x}\right)^2\left(\frac{\partial^2 w'}{\partial x^2}+\frac{\partial^2 w'}{\partial z^2}\right)+N^2\frac{\partial^2 w'}{\partial x^2}=0 \tag{2.32}$$

A.3 Vertically Propagating Waves during Flights 1 and 2

Figures C (a) and (b) depict the pattern of vertically propagating waves for Flights 1 and 2 respectively.

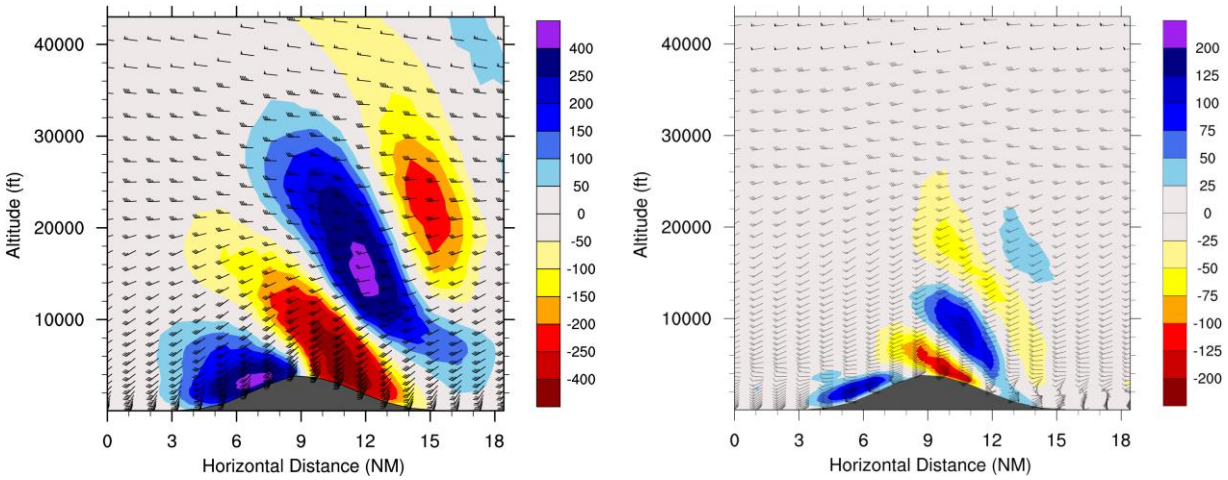

Figure C: (a) Vertically propagating waves present during Flight 1; (b) and during Flight 2. Shading denotes up or downdraft intensity with a positive sign corresponding to an updraft in ft/min. Vertical axes represent altitude in feet while horizontal axes show horizontal distance in nautical miles.

A.4 Brown and Ellrod TI1 Turbulence Indicators

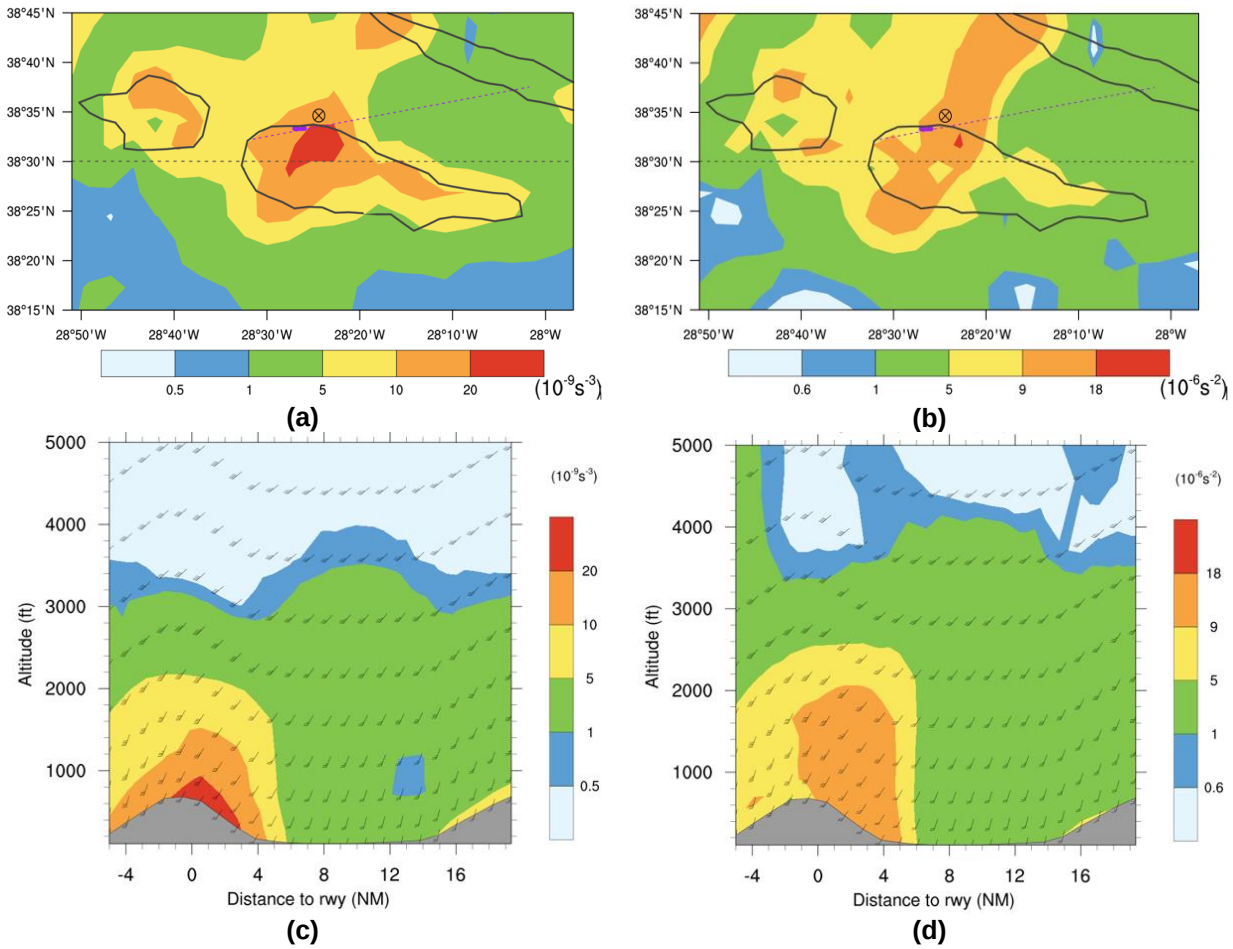

Figure D1: Horizontal variation of (a) Brown and (b) Ellrod TI1 at 66 m for Flight 1. Dotted pink line shows aircraft trajectory and pink bar locates the Aerodrome. The circled “x” mark identifies aircraft position at 66 m. Cross-sectional variation of (c) Brown and (d) Ellrod TI1.

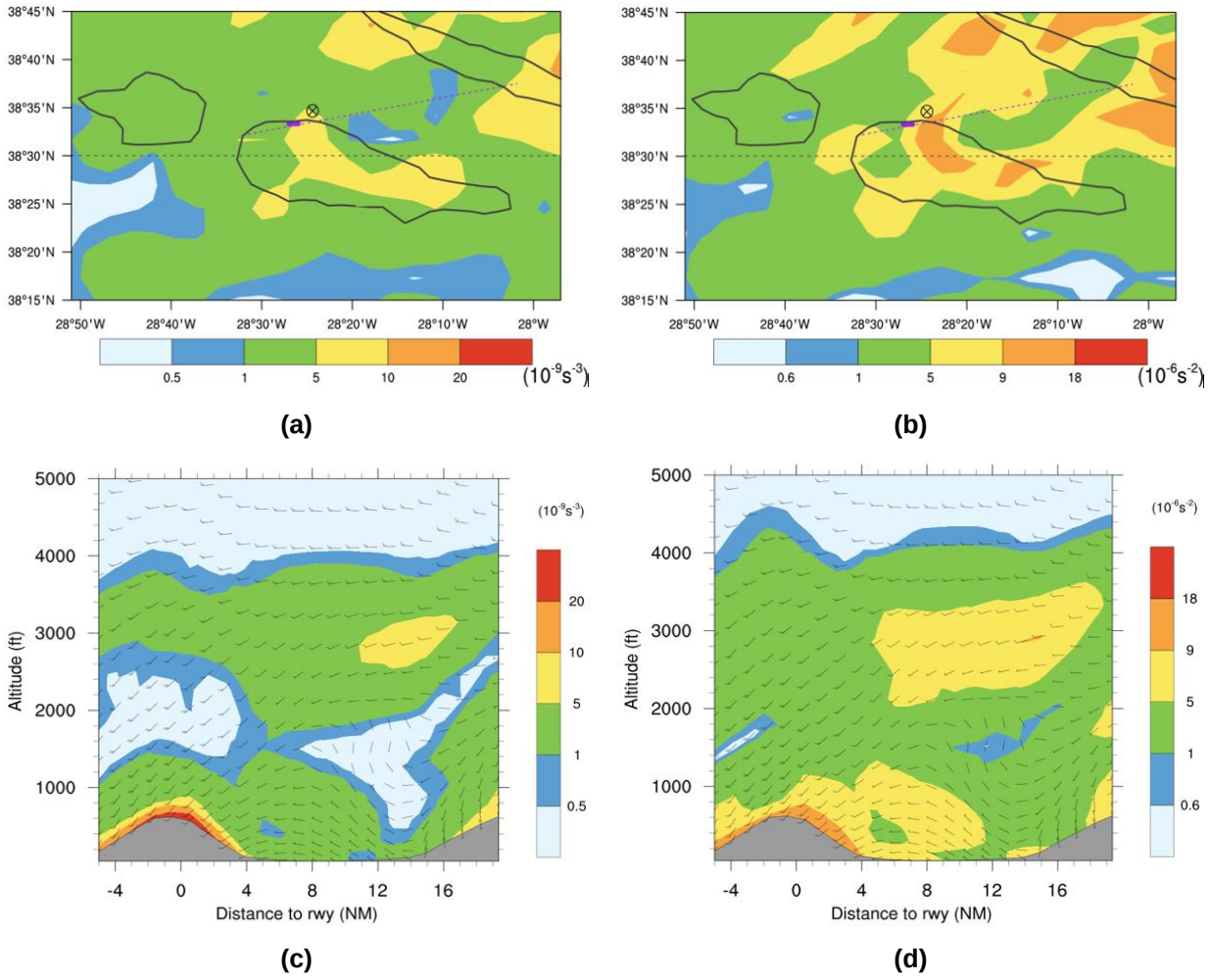

Figure D2: Horizontal variation of (a) Brown and (b) Ellrod TI1 at 66 m for Flight 2. Dotted pink line shows aircraft trajectory and pink bar locates the Aerodrome. The circled “x” mark identifies aircraft position at 66 m. Cross-sectional variation of (c) Brown and (d) Ellrod TI1.

A.5 Aircraft Specifications: A320-200 and B747-200

Figure E: Specifications of aircraft type used during Flights 1 and 2, from SATA [71].

Table E: Aircraft specifications by model [72].

	A320-200	B747-200
Length [m]	37.47	70.60
Wing span [m]	34.10	59.60
Mach Cruise	0.78	0.85
Max Takeoff Weight [kg]	78000	374850
Range [km]	4400	12700

A.6 Meteorological Convention

A wind vector is characterized by both a magnitude or its speed and direction. According to the meteorological convention, the angle describing this direction specifies the point from which the wind emanates. The example of a 225° wind with 30 kt is illustrated in Figure F.1. For a reference frame in which east and north are positive directions, the zonal component of the wind is positive when it flows from west to east and the meridional component is positive when it flows from south to north.

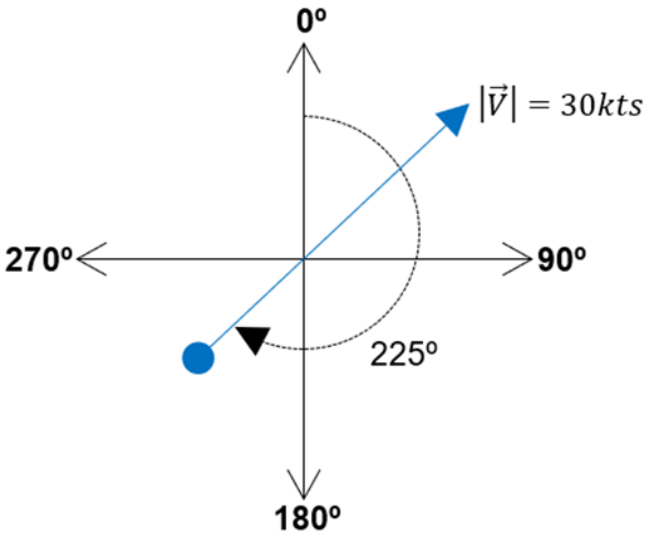

Figure F1: Meteorological convention for wind direction.

The wind may also be portrayed in terms of wind barbs. Figure F.2 (a) shows the example of wind at 25 kt from the northwest while (b) details wind at 50 kt from the southeast.

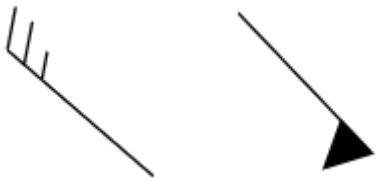

(a) **(b)**

Figure F2: Wind barb representations for (a) wind at 25 kt from NW and (b) wind at 50 kt from SE.

A complete barb in Figure F.2 (a) represents 10 kt and the shorter, half barb 5 kt. A flag mark in Figure F.2 (b) quantifies a 50 kt wind intensity. The locate to which they point will dictate the direction from which the wind emanates.